ZMB

ZENTRUM FÜR MEDIZINISCHE BIOTECHNOLOGIE
UNIVERSITÄT DUISBURG-ESSEN

The role of Par17's N-terminus in interaction and function of the enzyme

Inaugural Dissertation
for the doctoral degree of
Dr. rer. nat.

from the Faculty of Biology
University of Duisburg–Essen
Germany

Submitted by
Anna Göhring
Born in Ahlen

June 2021

DOI: 10.17185/duepublico/74845
URN: urn:nbn:de:hbz:465-20231030-094519-5

The experiments underlying the present work were conducted at the Department of Structural and Medicinal Biochemistry at the University of Duisburg-Essen.

1. Examiner: Prof. Dr. Peter Bayer

2. Examiner: Prof. Dr. Raphael Stoll

3. Examiner: /

Chair of the Board of Examiners: Prof. Dr. Shirley Knauer

Date of the oral examination: 24.09.2021

Man merkt nie, was schon getan wurde,
man sieht immer nur, was noch zu tun bleibt.
[Marie Curie]

Table of contents

List of abbreviations **6**
List of figures **8**
List of tables **10**
Abstract **12**
Zusammenfassung **13**
1 Introduction **15**
  1.1 Characteristics of the Xaa-Pro peptide bond and the corresponding *cis*/*trans* isomerization **15**
  1.2 Features of the parvulin family **17**
  1.3 Characteristics of Par17 and the differences from Par14 .... **18**
    1.3.1 Enzymatic efficiency and specificity (Protease-coupled isomerase assay) 20
    1.3.2 Segregating the function of both isoforms 22
  1.4 Aim of the work **26**
2 Materials and Methods **28**
  2.1 Materials **28**
    2.1.1 Chemicals 28
    2.1.2 Equipment 30
    2.1.3 Consumables 31
    2.1.4 Buffers and solutions 31
    2.1.5 Media 33
    2.1.6 Kit systems and Products 33
    2.1.7 Enzymes 34
    2.1.8 Peptides measured in the PPIase Assay 34
    2.1.9 Human cell lines 34
    2.1.10 Bacteria and Vectors 35
    2.1.11 Primers 35
    2.1.12 Antibodies 36
    2.1.13 Software 36
  2.2 Methods **37**
    2.2.1 Cloning and DNA Transformation in *E.coli* 37
    2.2.2 Protein expression and purification 38
    2.2.3 Protein cross-linking 39
    2.2.4 CD spectroscopy 40
    2.2.5 Immunoprecipitation and pull down of proteins and interactors 40
    2.2.6 Mass spectrometry 40
    2.2.7 Protease-coupled isomerase assay (PPIase Assay) 43
    2.2.8 Nuclear magnetic resonance spectroscopy (NMR) 44
    2.2.9 Actin polymerization assay 46
    2.2.10 Atto594 labeling of proteins and fluorescence anisotropy 46
    2.2.11 Peptide Spotter Array 47
    2.2.12 SDS-PAGE and Western blot 47
    2.2.13 Antibody purification from rabbit antiserum 48
    2.2.14 Cell culture 48
    2.2.15 Migration assay of Par14 and Par14/17 knockdown cells 49
    2.2.16 CRISPR induced knockdown of Par17 49
    2.2.17 Seahorse XF Cell Mito Stress Test 50

2.2.18 Model calculation with YASARA 50
2.2.19 Haddock 51

3 Results 52

3.1 Comparison of the $^1H^{15}N$-HSQC spectra of Par14 and Par17 52

3.2 Detection of the proximity of the N-terminus to the catalytic PPIase domain by cross-linking 56

3.3 Catalytic function of Par17 in comparison to Par14 and the isolated catalytic PPIase domain 61

3.3.1 Examination of the effect of the extended N-terminus on substrate specificity 61
3.3.2 Exploring the effects of the N-terminus on substrate specificity by NMR 71

3.4 Interaction partners identified by photo crosslinking for Par17, Par14 and the isolated N-termini of Par14 and Par17 76

3.4.1 Interacting proteins of the full-length parvulins identified by mass spectrometry 77
3.4.2 Interacting proteins of the N-termini of the parvulins identified by mass spectrometry 80

3.5 Function of Par17 in actin polymerization and migration 88

3.6 Function of Par17 in energy conversion 93

4 Discussion 98

4.1 Proximity and impact of Par17's N-terminus on its catalytic PPIase domain 98

4.2 The 25 N-terminal amino acids in Par17 cause a higher substrate specificity by binding the model substrate 100

4.3 Par17 interacts with target proteins involved in various cellular events 106

4.4 Narrowing down the functional role of Par17 within the cell 109

4.5 Conclusion and future prospective 114

5 Appendix 116

5.1 Appendix figures 116

5.2 Appendix tables 126

5.2.1 Table description of the attached tables 131

6 References 134

7 Danksagung 142

8 Lebenslauf 144

9 Eidesstattliche Erklärungen 145

List of abbreviations

Abbreviations	Meaning
aa	Amino acid
Abz	2-aminobenzoyl
ACE	Analytic Core Facility Essen
ATP	Adenosine triphosphate
cccDNA	Covalently closed circular DNA
CK2	Casein kinase 2
CI	Confidence interval
CL	Cross-linking
CRISPR	Clustered regularly interspaced short palindromic repeats
CSI	Chemical shift index
Cyps	Cyclophilins
Cα	alpha-carbon atom
F3-T3	FGFR3-TACC3 gene fusion
FDR	False discovery rate
FKBPs	FK-506 binding proteins
GST	Glutathione S-transferase
HBV	Hepatitis B virus
HBx	HBx protein
HNRPs	Heterogeneous nuclear ribonucleoproteins
IRS1	Insulin receptor substrate 1
k	Reaction rate constant
KD	Knockdown
KM	Michaelis-Menten constant
LB	Lysogeny broth
LC-MS	Liquid chromatography–mass spectrometry
LFQ	Label-Free Quantitation
LV	Empty vector
MCL	Markov Cluster algorithm
MP	Milk powder
MS	Mass spectrometry
MTS	Mitochondrial targeting sequence
NLS	Nuclear localization signal
NMR	Nuclear magnetic resonance spectroscopy
norm.	Normalization
NPS	Network protein sequence analysis
OCR	Oxygen consuption rate
OXPHOS	Oxidative phosphorylation
Par14	Parvulin 14
Par17	Parvulin 17
PIN4	Peptidyl-prolyl cis/*trans* isomerase NIMA-interacting 4
PKB	Protein kinase B
PPI	Protein-protein interaction
PPIase	Peptidyl-Prolyl *cis*/*trans* isomerases
PPIase Assay	Protease-coupled isomerase assay
PRE	Paramagnetic relaxation enhancement
pre-RNP	Preribosomal ribonucleoprotein
TRiC	Chaperonin-containing T-complex
WT	Wildtype
Xaa	Correspond to any amino acid

Amino acids

Ala (A)	Alanine
Arg (R)	Arginine
Asn (N)	Asparagine
Asp (D)	Aspartic acid
Cys (C)	Cysteine
Glu (E)	Glutamic acid
Gln (N)	Glutamine
Gly (G)	Glycine
His (H)	Histidine
Ile (I)	Isoleucine
Leu (L)	Leucine
Lys (K)	Lysine
Met (M)	Methionine
Phe (F)	Phenylalanine
Pro (P)	Proline
Ser (S)	Serine
Thr (T)	Threonine
Trp (W)	Tryptophan
Tyr (Y)	Tyrosine
Val (V)	Valine

List of figures

Figure 1: Schematic reaction profile of a *cis*/*trans* isomerization of a Xaa-Pro moiety in a model peptide. 16

Figure 2: Calculated Par17 structure from I-TASSER based on the PPIase X-Ray structure. 20

Figure 3: Reaction steps of the protease-coupled isomerase assay. 21

Figure 4: Schematic view of the known cellular role of Par14 and Par17. 25

Figure 5: Differences between Par14 and Par17 investigated by the comparison of the $^1H^{15}N$-HSQC spectra. 54

Figure 6: Mapping of the chemical shift changes in the $^1H^{15}N$-HSQC spectra on the structure of Par14 and Par17. 56

Figure 7: Intramolecular cross-linking of Par14 and Par17. 58

Figure 8: Cross-links of N-terminus and catalytic PPIase domain of Par14 and Par17. 60

Figure 9: Linearity of the rate constant of the catalyzed reaction with the amount of added enzyme Par17. 63

Figure 10: K_M determination of Par14. 65

Figure 11: Thermic and catalyzed reactions of protease-coupled isomerase assay for representative substrate peptides measured with Par17, Par14 and the catalytic PPIase domain. 67

Figure 12: Substrate specificity of the parvulins. 69

Figure 13: Shift changes in Par17 and the catalytic PPIase domain after the addition of a positive or negative charged representative of model substrate. 74

Figure 14: Relations between interactors of Par14 and Par17 identified by different analysis methods shown in a Venn diagram. 79

Figure 15: Comparison of the interactors enriched by the Par14 N-terminus and Par17 N-terminus with the interactors found for the full-length parvulins in a Venn diagram. 81

Figure 16: Categories of interactors from the N-termini of Par14/Par17 and their protein-protein interaction network. 87

Figure 17: Par17 function in actin binding and polymerization 88

Figure 18: Defining the binding of Par17 and actin using peptide spotted array and cross-linking 91

Figure 19: Actin polymerization and influence on cell motility. 92

Figure 20: Assessing the mitochondrial function after Par17 knockdown. 97

Figure 21: Model of the interdomain contact of Par17. 100

Figure 22: The active center of the PPIase domain occupied by DTT is demonstrated with highlighted amino acids whose resonances undergo chemical shift changes upon substrate peptide addition. 105

Figure 23: Graphical representation of the indicated cellular roles of Par14 and Par17. 109

Figure 24: Protein-protein complex model of Par17 and β-actin. 111

Appendix figure 1: Chromatogram and SDS-gels from the purification of the ^{15}N-labeled proteins. 116

Appendix figure 2: Chemical shift changes of Par14 and Par14$_{\Delta 1\text{-}22}$ in comparison to the isolated catalytic PPIase domain. 117

Appendix figure 3: CD spectra of WT parvulins compared to photo-reactive amino acid labeled parvulins. 117

Appendix figure 4: Absorption of free para-Nitroaniline at 390 nm at different concentrations. 117

Appendix figure 5: Thermic and catalyzed reactions of the protease-coupled isomerase assay for different substrate peptides measured with Par17, Par14 and the shared catalytic PPIase domain. 119

Appendix figure 6: NMR titration of Par17 and the isolated PPIase domain with two model substrate peptides. 120

Appendix figure 7: Chemical shift changes in Par14 and the isolated PPIase domain after the addition of the model substrate Suc-Ala-Glu-Pro-Phe-pNa. 120

Appendix figure 8: Chemical shift changes in Par17 after the addition of the different model substrates. 121

Appendix figure 9: Superposition of ^{1}H^{15}N-HSQC spectra of Par17's N-terminus before and after addition of model substrate. 122

Appendix figure 10: Chemical shift changes in N-terminus of Par17 after the addition of the model substrate Suc-Ala-Glu-Pro-Phe-pNa 122

Appendix figure 11: SDS-gel of DSSO Cross-linking of Par17 with actin. 123

Appendix figure 12: Sequences and relative protein levels of Par17 of the knockdown cell lines HEK293 C3.9 and HEK239 C2s4. 123

Appendix figure 13: Vector map of the pET41(+) PreSission vector. 124

Appendix figure 14: Vector map of the pSpCas9(BB)-2A-GFP vector. 125

List of tables

Table 1: Used chemicals 28

Table 2: Equipment used for the experiments........ 30

Table 3: Used consumables 31

Table 4: Composition of the buffers and solutions 31

Table 5: Composition of the used media........ 33

Table 6: Used finished products or kit systems........ 33

Table 7: Enzymes used in this work 34

Table 8: Peptides used for the PPIase Assay. 34

Table 9: Used cell lines 34

Table 10: Vectors with corresponding inserts used in this work. 35

Table 11: Primers........ 35

Table 12: Primary and secondary antibodies used in this worl........ 36

Table 13: Software used in this work listed with the corresponding manufacturers........ 36

Table14: Mean rate constant k, the standard deviation and the k_{cat}/K_M value of the target proteins calculated from the data of protease-coupled isomerase assay. 69

Table 15: Specificity of non-phosphate specific parvulins. 103

Appendix table 1: Detailed liquid chromatography settings before mass spectrometry measurements........ 126

Appendix table 2: Detailed mass spectrometry measurement settings........ 127

Appendix table 3: Detailed search settings for the mass spectrometry data........ 129

Appendix table 4: Proportions of initial c*is/trans* populations of model peptides Suc-Ala-Xaa-Pro-Phe-pNa obtained from PPIase Assay. 130

Appendix table 5: Chemical shifts changes of residues between the parvulin isoforms from Fig. 6. 131

Appendix table 6: Row and extracted data of the Photo and DSSO cross-linking. 131

Appendix table 7: Data of the PPIase assay measurements with the model substrate Suc-Ala-Ser-Pro-Phe-pNa and various Par17 concentrations........ 131

Appendix table 8: Data of the Michaelis-Menten kinetic measurements with Par14. 131

Appendix table 9: Row data, normalized data and calculations of the peptides measured with the PPIase Assay. 131

Appendix table 10: Chemical shift changes between the bound and free signals of the parvulin forms with all measured substrate peptides........ 131

Appendix Table 11: Venn diagram with proteins enriched by Par14 or Par17 compared with interactors available from other sources........ 132

Appendix Table 12: Venn diagram with proteins enriched by Par14’s N-terminus, Par17’s N-terminus compared to the enriched proteins of the full-length parvulins........ 132

Appendix table 13: Enriched proteins of Par14’s N-terminus classified in categories........ 132

Appendix table 14: Protein interactions identified by STRING for the bait Proteins of Par14’s N-terminus. 132

Appendix table 15: Enriched proteins of Par17’s N-terminus classified in categories. 132

Appendix table 16: Protein interactions identified by STRING for the bait Proteins of Par17’s N-terminus. 132

Appendix table 17: DSSO cross-linking data of Par17 and Actin exported from Proteome discoverer........ 132

Appendix table 18: Mito Stress Test measured oxygen consumption rate and normalization. 133

Abstract

Peptidyl-Prolyl *cis*/*trans* isomerases (PPIases) are important enzymes which accelerate protein folding and regulate proteins participating in various cellular processes. The group of parvulin-like PPIases includes the two human isoforms parvulin 14 (Par14) and parvulin 17 (Par17), which originate from the same gene (PIN4) by alternative transcription initiation. Both proteins share the same PPIase domain and N-terminus, and Par17 additionally carries an N-terminal extension of 25 amino acids. Despite this small difference, the two parvulins occur in different cellular compartments, which suggests that the proteins have different functions. Research conducted so far has rarely differentiated between both isoforms, although these parvulins are found in cancer related processes and play a role in virus replication.

This work now studies the influence of the additional 25 N-terminal amino acids of Par17 on the function and interaction of the enzyme. First, nuclear magnetic resonance spectroscopy (NMR) was used to investigate the influence of the N-terminus on the PPIase domain. A possible interaction of the N-terminus with the PPIase domain was further examined by cross-linking studies. Based on this data, an interaction model was subsequently constructed, demonstrating that the N-terminus can shield the catalytic center. Second, the enzymatic efficiency of Par17 for different substrates was analyzed using a protease-coupled PPIase assay. The presence of the unique part of the N-terminus of Par17 leads to a higher substrate specificity in comparison to the shorter isoform Par14. This is presumably caused by the binding of the N-terminal section to the more inefficiently catalyzed model substrates. Finally, a general approach using cross-linking, followed by co-immunoprecipitation and mass spectrometry was chosen to identify interaction partners of Par14 and Par17 and their N-termini. Due to the differences within their N-terminal regions, for Par14 and Par17 different interaction partners were identified, which were classified into various functional groups. Par17 was found to function in internal transport, internal cell motility, lipid metabolism, amino acid metabolism and oxidative phosphorylation. Based on these results a direct interaction between Par17 and actin was demonstrated causing the protein to polymerize in a concentration dependent manner. In addition, gene knockdown experiments in cells confirmed a function of Par17 in cell migration and oxidative phosphorylation.

Zusammenfassung

Peptidyl-Prolyl *cis*/*trans*-Isomerasen (PPIasen) sind wichtige Enzyme, die die Proteinfaltung beschleunigen und Proteine regulieren, die an verschiedenen zellulären Prozessen beteiligt sind. Zur Gruppe der Parvulin-ähnlichen PPIasen gehören die beiden menschlichen Isoformen Parvulin 14 (Par14) und Parvulin 17 (Par17). Sie werden durch alternative Transkriptionsinitiation von dem gleichen Gen (PIN4) transkribiert. Beide Proteine besitzen die gleiche PPIase-Domäne und den gleichen N-Terminus, wobei Par17 zusätzlich noch eine N-terminale Verlängerung von 25 Aminosäuren aufweist. Trotz dieses nur kleinen Unterschieds, kommen die beiden Parvuline in unterschiedlichen Zellkompartimenten vor. Dies legt nahe, dass die Proteine unterschiedliche Funktionen in der Zelle haben. In der bisherigen Forschung wurde kaum zwischen den beiden Isoformen unterschieden, obwohl diese Parvuline an Prozessen beteiligt sind die mit verschiedenen Krebsformen in Verbindung stehen und bei der Virusreplikation eine Rolle spielen.

Diese Arbeit untersucht deshalb nun den Einfluss der zusätzlichen 25 N-terminalen Aminosäuren von Par17 auf die Funktion und Interaktion des Enzyms. Hierzu wurde zunächst mittels Kernspinresonanzspektroskopie (NMR) der Einfluss des N-Terminus auf die PPIase-Domäne untersucht. Anschließend wurde eine mögliche Interaktion des N-Terminus mit der PPIase-Domäne durch Quervernetzungsstudien weiter untersucht. Basierend auf den gewonnenen Daten wurde ein Interaktionsmodell erstellt, das zeigt, dass der N-Terminus das katalytische Zentrum abschirmen kann. Weiter wurde die enzymatische Effizienz von Par17 für verschiedene Substrate mittels eines Protease-gekoppelten PPIase-Assays analysiert. Die Anwesenheit der N-terminalen 25 Aminosäuren von Par17 führt zu einer höheren Substratspezifität im Vergleich zur kürzeren Isoform Par14. Dies wird vermutlich durch die Bindung des N-terminalen Abschnitts an die ineffizienter katalysierten Modellsubstrate verursacht. Abschließend wurde ein allgemeiner Ansatz mit Quervernetzung, gefolgt von Co-Immunpräzipitation und Massenspektrometrie gewählt, um Interaktionspartner von Par14 und Par17 sowie deren N-Termini zu identifizieren. Aufgrund der Unterschiede innerhalb ihrer N-terminalen Regionen, konnten für Par14 und Par17 unterschiedliche Interaktionspartner identifiziert werden. Diese wurden in verschiedene funktionelle Gruppen eingeteilt. Dabei konnte festgestellt werden, dass Par17 wahrscheinlich eine

Funktion beim internen Transport, der internen Zellmotilität, dem Lipidstoffwechsel, dem Aminosäurestoffwechsel und der oxidativen Phosphorylierung hat. Basierend auf diesen Ergebnissen wurde eine direkte Interaktion zwischen Par17 und Aktin nachgewiesen, die zu einer konzentrationsabhängigen Polymerisation des Proteins führt. Darüber hinaus bestätigten Gen-Knockdown Experimente in Zellen eine Funktion von Par17 bei der Zellmigration und der oxidativen Phosphorylierung.

1 Introduction

The family of peptidyl-prolyl *cis*/*trans* isomerases (PPIases) consists of three groups, which include the cyclophilins (Cyps), the FK-506 binding proteins (FKBPs) and the parvulins [31, 52]. Their classification is based on various folds and topologies. However, they all have the ability to accelerate the *cis*/*trans* isomerization of peptidyl-prolyl bonds. This capability is of particular importance as the *cis*/*trans* isomerization of the Xaa-Pro bond (Xaa corresponds to any amino acid) is a rate limiting process in protein folding [11]. Another key aspect is their function in signal transduction and regulation [38]. Since the function of a protein depends on its topology, structural rearrangements like the *cis*/*trans* isomerization can affect it and, for instance, may result in signal transduction or inhibition [166].

1.1 Characteristics of the Xaa-Pro peptide bond and the corresponding *cis*/*trans* isomerization

In general, peptide bonds have planar shape due to their partial double bond character. This results from the delocalization of the electron pair of the nitrogen atom in the C-N bond of the protein backbone in the low-energy state [25]. Therefore, the two alpha-carbon atoms (Cα) located within the peptide bond have two energy minima states. They can be orientated either at a dihedral angle of 0° (*cis* conformation) or at a dihedral angle of 180° (*trans* conformation) with respect to each other [28]. Conversion of both states is hampered by a high activation energy barrier. The *trans* conformation is energetically more favorable since the steric hindrance of the Cα atoms is lower. This is also reflected in the energy that is needed to overcome the rotational barrier between the two states. Although the energy required depends on the amino acid residues and the length of the attached peptides, the *trans* to *cis* conversion requires more energy than the *cis* to *trans* conversion due to steric hindrance. For instance, in secondary amide peptide bonds the *trans* to *cis* conversion energy barrier is about 10-20 $kJ*mol^{-1}$ higher than the barrier of the reverse process [122]. For these reasons, peptide bonds are almost exclusively found in *trans* conformation (99.97%) in three-dimensional proteins, if peptidyl-prolyl bonds are neglected [135].

However, in peptidyl-propyl bonds, the energy difference between the *cis* and *trans* conformations is smaller than in non-peptidyl-prolyl bonds [82]. The steric advantage for the Cα atoms in the *trans* conformation is reduced in these imidic bonds due to the fixation of nitrogen within the proline ring system. Still, the two minimum energy states, *cis* and *trans*, remain (Fig. 1). Consequently, the *cis* portion of Xaa-Pro bonds in peptides and proteins is higher. About 10-40% of the peptidyl-prolyl bonds are predicted to be in the *cis* conformation in peptides and 7% in folded proteins [135]. Nevertheless, also in the case of peptidyl-prolyl bonds, isomerization remains a slow process due to a sustained high energy barrier (~85 kJ*mol^{-}1 for acetyl-L-proline) [16].

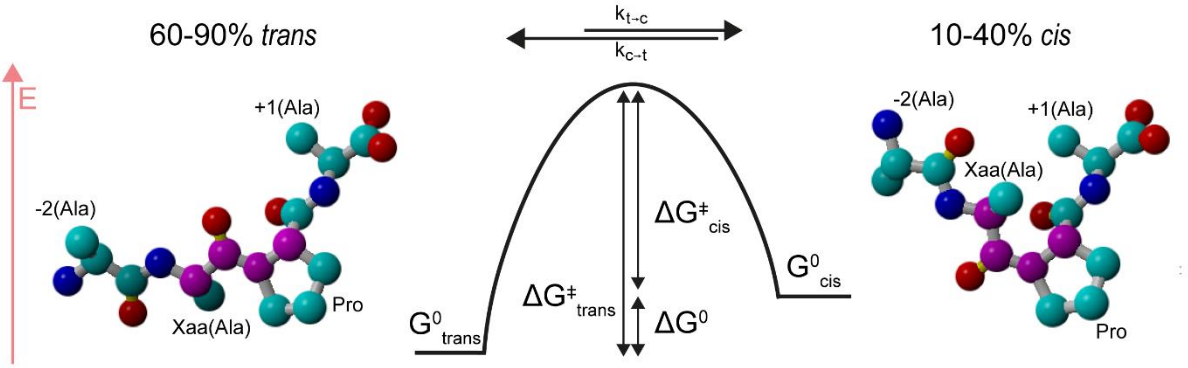

Figure 1: Schematic reaction profile of a *cis*/*trans* isomerization of a Xaa-Pro moiety in a model peptide. The model peptide Ala-Xaa-Pro-Ala is represented in its *trans* and *cis* conformation. The Gibbs free energy of activation ($\Delta G^{\ddagger}$) affects the kinetic constant for the *trans* to *cis* ($k_{t\to c}$) and *cis* to *trans* ($k_{c\to t}$) isomerization. The *cis* and *trans* population in the equilibrium state is determined by the ground state energy differences (ΔG_0). (Figure based on Dugave 2006 [25])

In the refolding of proteins, the isomerization of peptidyl-prolyl bonds takes about 10-100 seconds [95, 125]. Thereby it is a rate limiting process in protein folding since other process such as polypeptide chain collapse, secondary structure formation and segment rearrangement are faster [25]. Additionally, in already folded proteins *cis*/*trans* heterogeneities could be detected. The coexistence of both isoforms can act as a molecular switch between different functional states of proteins [83, 121, 166]. Owning to the importance of this process, enzymes naturally evolved to accelerate *cis/trans* isomerization. These enzymes were named peptidyl-prolyl *cis*/*trans* isomerases [30, 31, 68]. They have been proven to speed up protein-folding [68, 126] and affect many essential cellular events [71, 78, 130]. By accelerating isomerization, PPIases enable the process to play a role in cellular regulation [38]. This includes, for example, an influence on post-translational modification and protein-protein interactions. Due to the specific organization of their active site and surrounding elements, as well as extended N-termini or additional mediating domains, PPIases have gained high specificity for controlling their targeted cellular events [84].

1.2 Features of the parvulin family

Parvulins constitute a subgroup of peptidyl-prolyl *cis*/*trans* isomerases (PPIases) [104]. They are conserved through evolution and they have been found in a wide range of organisms, which indicates their fundamental importance [26, 96, 117]). The first member of the parvulin family, Par10 was discovered in *E.coli* in 1994 [104]. The family name derived from the Latin word *parvulus*, which means very small. The catalytic domains of parvulins with a size around 10 kDa are smaller than those of Cyps and FKBPs [103]. Nevertheless, parvulins seem to have a similar substrate selectivity as the FKBPs. In general, they prefer bulky, hydrophobic side chains preceding proline [52]. In contrast to Cyps and FKBPs, parvulins are not affected by the PPIase inhibitors cyclosporine A and FK506 [52, 104]. Following the discovery of Par10, further members of the parvulin subgroup were identified. The occurrence of parvulins in eukaryotes such as Ess1 in yeast [41, 42] and in higher mammalian organisms such as Pin1 in humans was demonstrated [78]. With these identifications an additional feature of parvulins showed up. Pin1 and Ess1 are selective for a phosphorylated serine or threonine preceding the proline [106]. Pin1's catalytic efficiency is about 1000 times higher for phosphorylated, rather than unphosphorylated, substrates [114]. Thus, parvulins could further be subclassified into phosphorylation specific members such as Pin1/Ess1 and non-phosphorylation specific parvulins such as Par10 [88, 145, 159].

As with the other PPIase family members, single-domain and multiple-domain proteins are also common for parvulins [123]. In bacteria and archaea single domain parvulins are more abundant [70]. Par10, for example, represents a single domain parvulin (93 aa) [67] with a high PPIase activity [104]. By contrast, in eukaryotes, parvulins that have an N-terminal extension or additional domains are frequently found. Multi-domain parvulins have been found in a wide range of organisms, from unicellular eukaryotic cells such as trypanosomes [26, 110] to complex organisms such as mammals [104, 145]. The human Pin1, for instance, has an additional small WW domain (39 aa) at the N-terminus which is connected to the PPIase domain by a flexible linker (9 aa) [5, 78]. The WW-domain is composed of a triple-stranded antiparallel β sheet, which forms a molecular hydrophobic clamp [106]. The WW-domain targets phosphorylated proline-rich substrates and mediates protein-protein interactions [80].

In addition, eukaryotes usually contain multiple parvulins. Humans are a relevant example, with three of the known parvulins present in cells. First, the previously mentioned peptidyl-prolyl *cis*/*trans* isomerase NIMA-interacting (Pin1) was identified [78]. So far, it is the most intensively studied parvulin, as it plays a crucial role in cell cycle progression. Furthermore, it is involved in many diseases such as cancer [15, 102, 160] and Alzheimer's disease [79, 94, 156]. In 1999 a second parvulin Parvulin 14 (Par14, initially also known as eukaryotic homolog of parvulin, EHPF) was found by nucleotide Blast search of the human genome [117, 145]. The name is derived from the size of the protein of approximately 14 kDa. The protein consists of a PPIase domain (96 aa) and a flexible and unstructured N-terminal extension (35 aa, later referred to as N-terminus). The third human parvulin was identified in 2006 [89]. It is an extended isoform of Par14 with a size of about 17 kDa. Therefore, the parvulin was named Parvulin 17 (Par17). Interestingly, homologs of Pin1 and Par14 are present in many eukaryotic unicellular and complex organisms, while the occurrence of Par17 has been found only in hominids. Although the genetic sequence of Par17 is already coded within the genome of other mammals, the required start codon for the open reading frame could only be found in gorillas, pongos and pans [61, 89]. Therefore, an important function of Par17 in the evolution of higher primates is suggested [84].

1.3 Characteristics of Par17 and the differences from Par14

Par17 originates from the PIN4 locus on chromosome Xq13.1, which also gives rise to the shorter protein isoform Par14 [89]. The elongated mRNA of Par17 is created by alternative transcription initiation. No TATA boxes or downstream promoter elements were found near the open reading frame, indicating weaker promoter elements and explaining alternative transcription initiation. The open reading frame of Par17 contains a start codon and a 72 base pair extension attached to the 5’ end of the open reading frame of Par14. Therefore, the mRNA encodes a protein that contains the complete sequence of Par14 and is extended at the N-terminus by 25 amino acids. Thus, Par17 has a total size of 151 amino acids and the flexible N-terminus has a total length of 61 amino acids. Furthermore, the in unique N-terminal segment of Par17 two single nucleotide polymorphisms (SNPs) were identified that occur simultaneously. The SNPs results in an exchange of Q16R and R18S. The exchange was observed in approximately 10% of the cDNA samples studied [89].

Since Par14 and Par17 have the same PPIase domain sequence, the domain should be structurally almost identical for both proteins [74]. The PPIase domain (elucidated for Par14; PDB ID: 3UI6 and 1EQ3) has the typical secondary parvulin element sequence $\beta_1\alpha_1\alpha_2h\beta_2\alpha_3\beta_3\beta_4$, with h denoting a helical turn (3_{10}-helix) or small helix [90, 128, 139]. The flexible N-terminus of Par17 (in total 61 aa) includes the N-terminus of Par14 (36 aa) [89]. An I-TASSER model of Par17 was calculated [161] based on the X-ray structure of the PPIase domain (PDB ID: 3UI6 [91]) and overlaid with its template (Fig. 2A).

Only minor differences can be observed in the PPIase domain. A chemical shift index (CSI) analysis of Par17 also suggests only small differences from the PPIase domain of Par14. First, the second β-strand could not be identified in Par17 [74]. The lack of the β-strand can also be observed in the I-TASSER model. Second, an additional short β-strand between Val^{135} and Asp^{138} was indicated [74]. Interestingly, the I-TASSER model loses the subsequent very short ß-strand ranging from Val^{141} to Asp^{143} present in the X-ray structure [91] and predicted by the CSI analysis of Par17 [74]. Despite this, the catalytic center is the same as that of Par14. The residues Leu^{69}, Leu^{107}, Met^{110}, Met^{115}, Val^{116}, Phe^{119} and Phe^{145} make up the mainly hydrophobic active site in addition to the conserved hydrogen bonding network between Asp^{99}, H^{67}, His^{148} and Thr^{143} (Fig. 2B) [90]. Furthermore, the I-TASSER model predicts secondary structure elements for the N-terminus. Three α-helixes can be observed (ranging from Met^{3}-Ser^{18}, Gln^{22}-Ser^{31} and Ser^{44}-Gly^{55}) and a small helical turn (Lys^{36}-Gly^{38}). They do not assemble into a tertiary structure but rather exist exposed. Kessler et al. also predicts an α-helical fold from Met^{3} to Ala^{23} with Network Protein Sequence (NPS) analysis and points to the amphiphilic character of the sequence [61]. In the CSI analysis of Lin et al. [74] only the ^{13}CO chemical shift values hint to an α-helical fold in the N-terminus. In the corresponding ^{13}Cα and ^{13}Cβ chemical shift values no indication of secondary elements could be found. Therefore, it was suggested that the N-terminus of Par17 only adopts a structure during interaction with another protein or ligand. Additionally, a possible weak interaction was suggested between the N-terminus and the PPIase domain of Par17, although no long-range NOE connectivities could be measured that would indicate a strong interaction [74]. Changes in the chemical shift of some amino acids in the catalytic domain observed between differentially recorded Par14 and Par17 $^{1}H^{15}N$ HSQC spectra point to an interaction between the N-terminus and the catalytic PPIase domain [14].

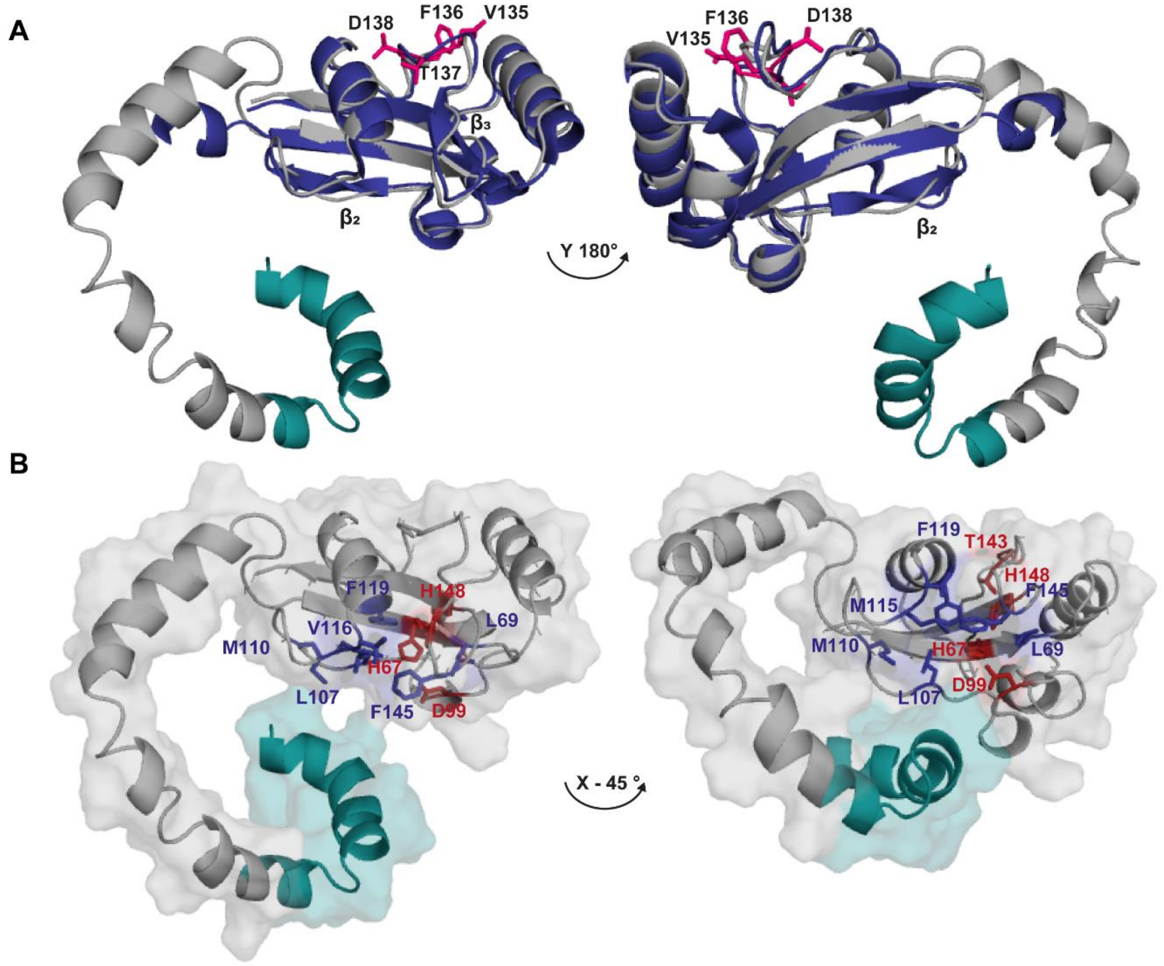

Figure 2: Calculated Par17 structure from I-TASSER based on the PPIase X-Ray structure. A: The Par17 structure (gray) is overlaid with the known PPIase domain structure (blue, PDB ID: 3UI6). Minor differences between the structures are indicated. **B:** Surface representation of Par17 with tagged active site. The amino acids that made up the hydrophobic core (blue) and the hydrogen-bonding network (red) are highlighted. In addition, the amino acids exclusive for Par17 are marked (turquoise).

1.3.1 Enzymatic efficiency and specificity (Protease-coupled isomerase assay)

There are different methods to determine the *cis*/*trans* conversion of PPIases. One very precise method is nuclear magnetic resonance spectroscopy (NMR). With 2D exchange spectroscopy and saturation transfer, the k_{cat}/K_M values could be determined tag-free in a temperature dependent manner [49, 53]. For a more advanced, precise analysis and the kinetic characterization of all individual reactions involved, line shape analysis can be applied [40, 60]. Furthermore, photometric assays can be used to determine the kinetic efficiency of the PPIases. These assays give the same results as the more complex NMR 2D exchange spectroscopy and saturation transfer, but are faster and easier to perform [60]. One very well established assay is the protease coupled isomerase assay first described by Fischer et al. [29]. The basic principle of the assay is the use of a conformation-specific protease that cleaves a traceable signal from the targeted model substrate to visualize isomerization. In this assay, the protease used is chymotrypsin, which only cleaves peptides N-terminal to Trp, Tyr, Phe and Leu that are in the *trans* conformation. The steps of the assay reaction can be seen in Figure 3.

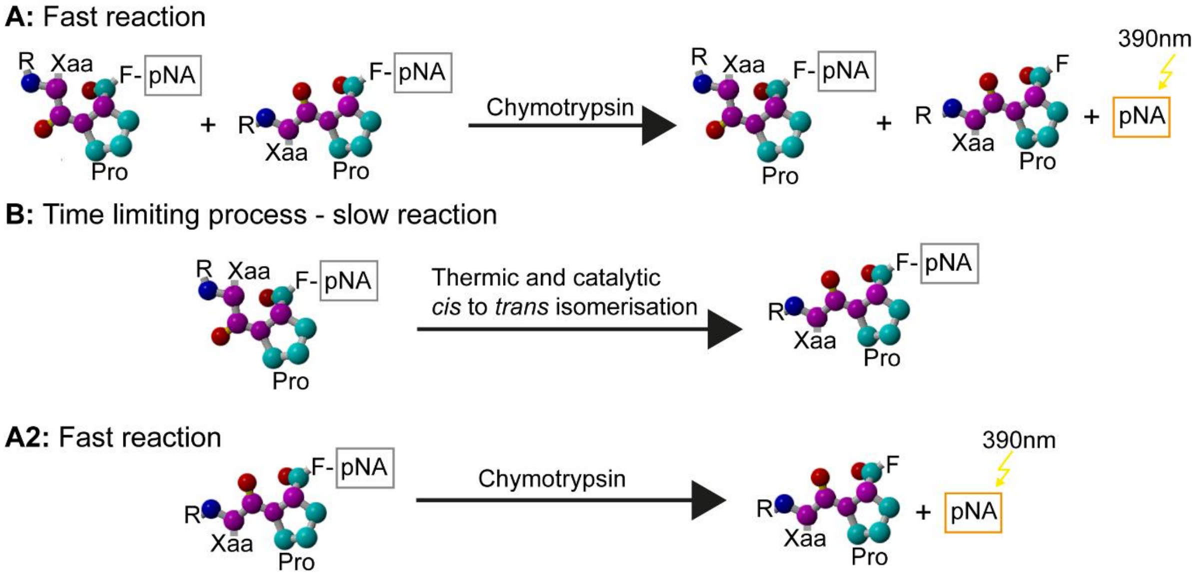

Figure 3: Reaction steps of the protease-coupled isomerase assay. A: *Trans* and *cis* populations of the model substrates R-Xaa-Pro-F-pNa are present in the solution. As soon as α-chymotrypsin is added, it facilitates the cleavage of the *trans* isomers by hydrolysis reaction. The free para-Nitroaniline (pNa) absorbs light (λ = 390 nm). **B:** The *cis* isomers remaining after the fast proteolytic cleavage are isomerized to *trans* isomers additively by the thermic and catalytic reactions. This reaction step is slow, and therefore the rate limiting process. **A2**: The new formed *trans* isomers are hydrolyzed by α-chymotrypsin immediately. This is how isomerization can be monitored. Process B and A2 take place to adjust the equilibrium and last until the model substrate is almost completely cleaved.

When the chymotrypsin concentration is sufficient, the equilibration of the *cis* to *trans* isomerization follows the first burst of pNa hydrolysis of the *trans* isomers. The height of the signal of the first burst corresponds to the *trans* population at the beginning of the measurement. Then the isomerization can be tracked by immediate hydrolysis of the newly formed *trans* peptides following pseudo first order kinetics at high chymotrypsin concentrations [29]. The first order rate constant of the isomerization can be obtained by non-linear fitting methods, provided that the substrate concentration (*cis*-shaped peptide) is lower than the K_M value. Under this conditions the observed rate constant corresponds to the sum of the thermal rate constant and the catalyzed rate constant ($k_{observed} = k_{thermal} + k_{catalytic}$) [43]. With the knowledge of the rate constant of the thermal reaction and PPIase concentration, the specificity constant $k_{cat/}K_M$ can be determined [2]. The assay was further improved in 1990 by adjusting the peptide medium, which increases the initial proportion of *cis* isomers [63].

For Par17 the PPIase assay was performed with an attached glutathione S-transferase (GST)-tag and only one model substrate Suc-Ala-Phe-Pro-Phe-pNa [142]. The reported K_{cat}/K_M value was approximately $4 \cdot 10^3$ M^-1s^{-1}. Additionally, the efficiency of the mutant GST-Par17$_{D99A}$ was determined. The aspartate is involved in the hydrogen-bonding network in the active site and predicted to be important for the catalysis [90]. The mutation resulted in a reduced efficiency of about one order of magnitude [142]. However, these measurements do not indicate anything about the efficiency of the protein without a tag and do not provide any insight into substrate specificity. The general efficiency of Par17 is probably similar to that of Par14. For seven substrate peptides the efficiency of Par14 was found to be low, around $0.1 \cdot 10^3$-$4 \cdot 10^3$ $M^{-1}s^{-1}$ [145]. With these values, the efficiency of both isoforms is rather moderate. The other human PPIase Pin1 is about 10^3-10^4 times more efficient for its substrate. The $k_{cat/}K_M$ values for the peptide with phosphorylated Ser at the Xaa position was about $3 \cdot 10^6$-$2 \cdot 10^7$ $M^{-1}s^{-1}$ and for the unphosphorylated Ser peptide $2.9 \cdot 10^3$ $M^{-1}s^{-1}$ [114, 146].

1.3.2 Segregating the function of both isoforms

Assessing the presence of Par17 and Par14 in tissues is difficult. In many studies, the differentiation between Par14 and Par17 was neglected because of the difficult technical process of discrimination between the two isoforms [37]. In general, the Human Protein Atlas (HPA) [148] reports that Pin4 mRNA can be detected in almost all tissues. Also, the expression of Par14/17 could be shown in many tissues. The highest expression was shown in different tissues of the brain, as well as in the stomach, pancreas, oral mucosa and testes (retrieved from the HPA on 03.21). Müller et al. determined the proportion of Par17 mRNA in the total PIN4 mRNA in selected tissues to range between 0.2 and 2.5%. The highest percentage was observed in the submandibular gland, followed by the brain, blood vessels, kidney and mammary gland [89]. However, the percentage does not allow any conclusions to be made regarding the amount of protein expression.

Within the cell, Par17 and Par14 are localized in different compartments. Par14 can be observed in the cytoplasm, but is mainly localized in the nucleus [137]. Especially, it was found to concentrate in the nucleolus during the interphase [33, 34]. Moreover, Par14 shuttles between the nucleus and the cytoplasm. Import into the nucleus is directed through the N-terminus of Par14 with the amino acids Ser^{7}-Lys^{14} likely functioning as a nuclear localization signal (NLS) [137]. The import is controlled by phosphorylation of Ser^{19} presumably by the casein kinase 2 (CK2). The S19A mutant of Par14, which mimics the dephosphorylated state, is not transported into the nucleus (Fig. 4) [112]. The export of Par14 from the nucleus is maintained by the 14-3-3 protein, which is dependent on the simultaneous phosphorylation of Ser^{7} and Ser^{9} of Par14 [111]. In contrast, Par17 is located in the cytoplasm and mitochondrion [61, 142]. The import into the mitochondrion is dependent on the exclusive 25 N-terminal amino acids of Par17 [61]. This sequence is predicted to have a mitochondrial targeting signal. Moreover, the transport of Par17 into the inner mitochondrial membrane is dependent on the presence of a mitochondrial membrane potential [88]. In addition, Par17 was identified in the sub-cellular fraction of the cell membrane [61].

Concerning the function of both parvulins within cell compartments, first a DNA-binding motif was identified in the sequence of Par14 and Par17 [137, 145]. DNA binding of Par14 and Par17 was demonstrated in vitro [61]. In case of Par14, the N-terminus is responsible for high affinity DNA-binding (corresponding to the amino acids 25-61 in Par17) [137]. However, the function of DNA binding within the cell remains elusive. Involvement in processes like transcription regulation and cell-cycle regulation, as observed for PIN1 [15], were suggested [84]. In further studies, an association of unphosphorylated Par14 with the pre-ribosomal ribonucleoprotein (pre-rRNP) complex was shown [33, 34]. For the association the presence of the N-terminus of

Par14 was mandatory. Since the reduced presence of Par14 slowed down the processing of pre-rRNA to 18 and 28 S rRNAs, Par14 was attributed a role in rRNA processing [34]. When overexpression of Par14 was identified in Pin1 knockdown mice, a compensatory function of Par14 for Pin1 was proposed, and the function of Par14 in insulin sensitivity was investigated. Par14 was found to associate with insulin receptor substrate 1 (IRS1, Fig. 4) [163]. Again, the N-terminus with a portion of the PPIase domain was mandatory for contact. The presence of Par14 enhanced phosphorylation of IRS1 as well as downstream phosphoinositide 3-kinases (PI3K) binding and protein kinase B (PKB) phosphorylation (Fig. 4). Recently, in human glioblastoma cases with FGFR3-TACC3 gene fusion (F3-T3), PIN4 phosphorylation at $\text{Tyr}^{122}/\text{Tyr}^{147}$ was found to be an intermediate step in the signaling pathway of mitochondrial metabolism activation [32]. In this study, the distinction between Par14 and Par17 was neglected, but PIN4 in general was found to interact with the F3-T3 protein. As a result, enhanced phosphorylation at the $\text{Tyr}^{122}/\text{Tyr}^{147}$ site was identified. In addition, the Human Protein Atlas contains data on lung cancer, testicular cancer, and urothelial cancer in which high PIN4 expression levels resulted in better prognoses [147]. This reinforces the suspicion that the two parvulins may contribute to diseases such as cancer. Furthermore, a previously unrecognized function of Par14 and Par17 in virus replication was discovered [118]. In the presence of HBx protein (HBx) both isoforms upregulated hepatitis B virus (HBV) replication. Par14 and Par17 bound HBx and the cccDNA and thereby increased the covalently closed circular DNA (cccDNA) levels and viral replication. For the effect to occur, both isoforms had to be intact. Mutants of the isoforms with single amino acid exchanges such as S19/44A (preventing nuclear import of Par14) and D74/99A (decreasing isomerization efficiency) lost the effect on viral replication [118].

As already mentioned, Par17 has rarely been studied individually without the shorter isoform Par14. The only studies that focused on Par17 alone were those that reported the occurrence of Par17 [61, 89] and two additionally studies that examined the interaction of Par17 with tubulin *in vitro* [14, 142]. Par17 was found to catalyze tubulin polymerization in GTP and in a concentration dependent manner. For efficient polymerization, the N-terminus of Par17 was required as well as intact PPIase activity. The binding site of Par17 was narrowed down two binding motifs by microarray display with GST-Par17. The motifs cover the first α-helix Lys^{75}-Lys^{85} and the area including the second β-sheet Gln^{103}-Phe^{118}. With the same approach in tubulin, one binding motif was identified that included an Arg-Pro-Asp sequence [142].

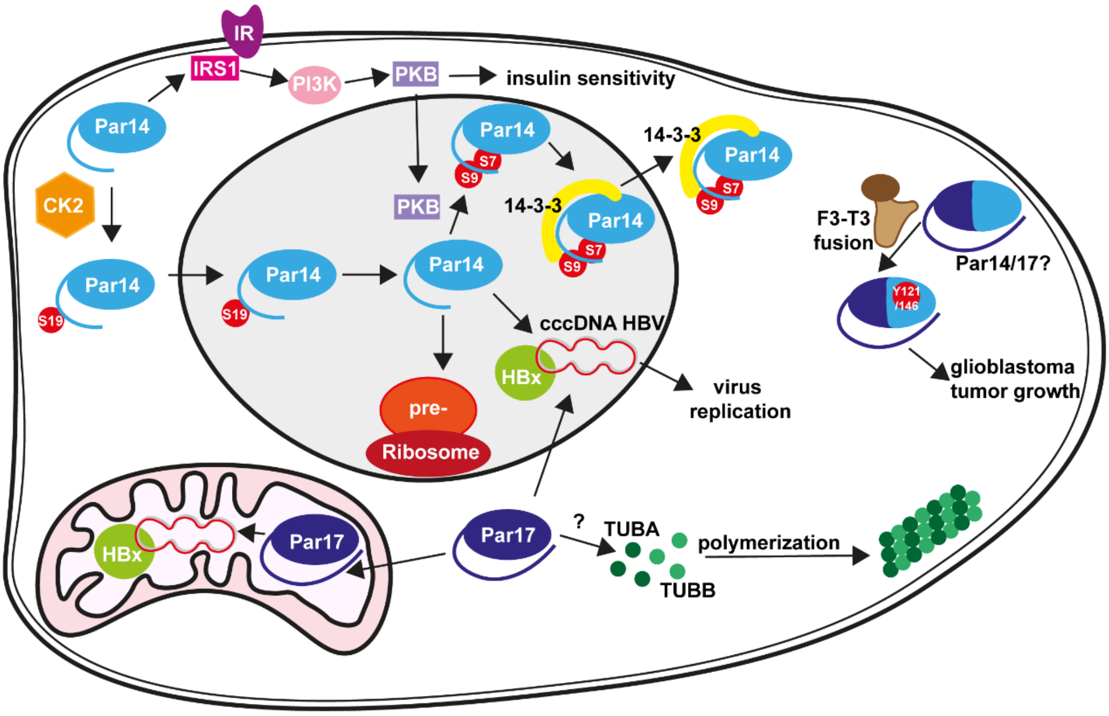

Figure 4: Schematic view of the known cellular role of Par14 and Par17. Par14 (light blue) shuttles between the nucleus and the cytoplasm [111, 112] and it is associated with insulin sensitivity [163], ribosomal biogenesis and rRNA processing [34], viral replication of HBV and glioblastoma tumor growth [118]. Par17 (dark blue) is transported into the mitochondrion [61] and associated with tubulin polymerization [14], virus replication [118] and glioblastoma tumor growth [14, 32, 61, 118]. IRS-1 = insulin receptor substrate 1; IR: Insulin receptor, PI3K = phosphatidyl-inositol-4,5-bisphosphate 3-kinase, PKB = phosphokinase B, CK2 = casein kinase 2, 14-3-3 = 14-3-3 protein, TUBA = tubulin α-chain, TUBB = tubulin β-chain, HBx = HBx protein. Cytoplasm (white) and nucleoplasm (grey) and mitochondrion (pink) are colored.

1.4 Aim of the work

The human PPIase Par17 differs from its shorter isoform Par14 only by an extension of 25 amino acids at the N-terminus. The structure of the PPIase domain is almost the same in both parvulins and Par17 also contains the N-terminus of Par14 [74, 89]. Nevertheless, the two proteins are found in different cellular compartments. Par14 is mainly located in the nucleus [111] and Par17 in the mitochondrion [61], indicating that the two isoforms have different functions within the cell. However, the impact of the N-terminal 25 amino acids of Par17 on the interaction and function of this protein is mostly unexplored.

Initially, there was an indication that the flexible and free N-terminus of the PPIase interacts with the active domain [14]. The possible interaction will be investigated in this work by comparing $^{1}H^{15}N$-HSQC NMR spectra of both isoforms. The spectra indicate each individual residue within the protein and changes due to the presence of the N-terminus can be tracked. To complete possible interaction regions, chemical and photo-reactive cross-linking will be used in this work. First, the established chemical cross-linker DSSO will be used, linking Lys residues. Second, to increase sequential coverage, the photo-reactive amino acid L-photo-leucine and L-photo-methionine will be used. These modified amino acids have a diazirine ring that becomes a highly reactive carbene upon irradiation with ultraviolet light. The reactive photo amino acids can be incorporated into proteins by *E.coli*, allowing the production of recombinant labeled proteins [7, 97]. Within the protein the photo-reactive amino acids react with any compound in the proximity, most likely water but also any amino acid from an interaction partner [136]. However, a preferential reaction with carboxylic acids and the amino acids Tyr, Asp, and Glu has been observed [50]. The resulting covalent bonds will then be analyzed by mass spectrometry (MS) to identify interaction regions.

Furthermore, the effect of the N-terminal 25 amino acids of Par17 on the efficiency and substrate specificity of the PPIase domain is obscure. To explore this, the well-established protease-coupled PPIase assay will be used [30, 63]. First, the applicability of the assay will be evaluated for the two parvulin isoforms, which have low isomerase efficiency. Subsequently, the assay will be performed with different model substrates with varying amino acids at the Xaa-Pro position to narrow down a possible specificity of Par17. Concurrently the selectivity will be compared to those of the shorter isoform and the isolated catalytic domain.

The importance of the two human parvulins is increasing as they are involved in cancer cases [32] and in viral replication [118] and thus could be possible drug targets. However, the exact function of Par14 and Par17 within the cell has only been rudimentarily investigated. In addition, most studies lack the distinction between the two isoforms. Therefore, this work will apply a general approach that attempts to identify novel interaction partners of both parvulins within the cell and classify them into possible functional categories. Co-immunoprecipitation of the respective parvulin, followed by identification of interactors by MS is chosen as such an attempt. To overcome the restriction of strong binding that such methods require, photo-reactive cross-linking will be used. Thereby, the weak and transient interactions are covalently cross-linked before purification and identification. The photo-reactive amino acids were already used to identify protein-protein interactions [44, 136]. In the general approach, living cells incorporated the amino acids in all proteins, protein interactions are cross-linked via irradiation and the interactions are analyzed by western blot or MS. In this thesis, the photo-reactive amino acids will be incorporated into the protein of interest by recombinant expression in *E.coli*. After purification, the proteins will be added to the cell lysate, cross-linked by irradiation and identified by MS. This approach will not only reduces the detection of nonspecific interactions compared to labeling of the total cell lysate, but will also allow the differentiation between the two isoforms. By supplementing recombinant proteins to the lysate the identification of interactors from only the isolated N-termini will also be possible. Subsequently, selected functions of Par17 and individual interaction partners identified will be examined in more detail.

2 Materials and Methods

2.1 Materials

2.1.1 Chemicals

Table 1: Used chemicals

Chemicals	Abbreviation	Manufacturer
Acetonitrile UPLC grade	ACN	Sigma-Aldrich, Darmstadt, Germany
Antimycin A	AA	Sigma-Aldrich, Darmstadt, Germany
Ammonium persulfate	APS	Roth, Karlsruhe, Germany
Brilliant Blue 250G		Sigma-Aldrich, Darmstadt, Germany
Bisacrylamide Rotiphorese Gel 30		Roth, Karlsruhe, Germany
Bromophenol blue		Roth, Karlsruhe, Germany
Boric acid	H_3BO_3	Roth, Karlsruhe, Germany
Bovine serum albumin fraction V	BSA	PAN-Biotech, Aidenbach, Germany
Calcium chloride dihydrate	$CaCl_2 \cdot 2\ H_2O$	Roth, Karlsruhe, Germany
Cobalt chloride hexahydrate	$CoCl_2 \cdot 6\ H_2O$	Fluka, Buchs, Switzerland, Germany
Copper chloride dihydrate	$CuCl_2 \cdot 2\ H_2O$	Sigma-Aldrich, Darmstadt, Germany
Copper sulfate pentahydrate	$CuSO_4 \cdot H_2O$	Sigma-Aldrich, Darmstadt, Germany
Diammonium hydrogen citrate		Fluka, Buchs, Switzerland, Germany
2,5-dihydroxyacetophenone	2,5-DHAP	Thermo Scientific, Darmstadt, Germany
2,2-Dimethyl-2-silapentan-5-sulfonat	DSS	Sigma-Aldrich, Darmstadt, Germany
Disodium hydrogen phosphate	Na_2HPO_4	Roth, Karlsruhe, Germany
Disuccinimidyl sulfoxide	DSSO	Thermo Scientific, Darmstadt, Germany
Dimethylsulfoxid MS grade	DMSO	Thermo Scientific, Darmstadt, Germany
Dulbecco's Modified Eagle Medium	DMEM	Thermo Scientific, Darmstadt, Germany
DMEM Limiting Medium	DMEM-LM	Thermo Scientific, Darmstadt, Germany
D-glucose	$C_6H_{12}O_6$	Roth, Karlsruhe, Germany
EDTA disodium salt dihydrate	Na_2EDTA	Roth, Karlsruhe, Germany
Ethanolamine		Fluka, Buchs, Switzerland, Germany
Fetal Bovine Serum	FBS	PAN-Biotech, Aidenbach, Germany
Fetal Bovine Serum, dialyzed		Thermo Scientific, Darmstadt, Germany
Formaldehyde 4%		Merck, Darmstadt, Germany
Folic acid		Sigma-Aldrich, Darmstadt, Germany
Formic acid	FA	Sigma-Aldrich, Darmstadt, Germany
Igepal CA 630		MP Biomedical, Eschwege, Germany
Iron (III) chloride hexahydrate	$FeCl_3 \cdot 6\ H_2O$	Fluka, Buchs, Switzerland
Iron (III) citrate		Sigma-Aldrich, Darmstadt, Germany
Isopropanol		Fisher Chemical, Schwerte, Germany
Isopropyl β-D-1-thiogalactopyranoside	IPTG	AppliChem, Darmstadt, Germany
Kanamycin sulfate		Roth, Karlsruhe, Germany
2-[4-(2-hydroxyethyl)piperazin-1-yl]ethanesulfonic acid	HEPES	Roth, Karlsruhe, Germany

Lithium chloride	LiCl	Roth, Karlsruhe, Germany
Magnesium sulfate heptahydrate	$MgSO_4 \cdot 7\,H_2O$	Sigma-Aldrich, Darmstadt
Manganese chloride tetrahydrate	$MnCl_2 \cdot 4\,H_2O$	Fluka, Buchs, Switzerland
Manganese sulfate hydrate	$MnSO_4 \cdot H_2O$	Sigma-Aldrich, Darmstadt,Germany
Midori Green Advance		Nippon Genetics Europe, Dueren, Germany
Sodium chloride	NaCl	AppliChem, Darmstadt, Germany
Nickel chloride hexahydrate	$NiCl_2 \cdot 6\,H_2O$	Roth, Karlsruhe, Germany
Nicotinamide		AppliChem, Darmstadt, Germany
Skim milk powder		Heirler Cenovis, Radolfzell, Germany
Orange G		Roth, Karlsruhe, Germany
Pantothenic acid		Sigma-Aldrich, Darmstadt, Germany
Penicillin/Streptomycin	P/S	PAN-Biotech, Aidenbach, Germany
Phenyl methyl ethylenediamine	PMSF	Serva, Heidelberg, Germany
p-Nitroaniline	pNa	Sigma-Aldrich, Darmstadt, Germany
Ponceau S		Roth, Karlsruhe, Germany
Potassium chloride	KCl	AppliChem, Darmstadt, Germany
Potassium dihydrogen phosphate	KH_2PO_4	Roth, Karlsruhe, Germany
L-photo-leucine		Thermo Scientific, Darmstadt, Germany
L-photo-methionine		Thermo Scientific, Darmstadt, Germany
MES SDS Running buffer (20x)		Thermo Scientific, Darmstadt, Germany
Oligomycin		Sigma-Aldrich, Darmstadt, Germany
Riboflavin		Sigma-Aldrich, Darmstadt, Germany
Rotenon		Sigma-Aldrich, Darmstadt, Germany
Tetramethylethylenediamine	TEMED	AppliChem, Darmstadt, Germany
Trifluorethanol	TFE	Fluka, Buchs, Switzerland, Germany
Sodium dihydrogen phosphate	NaH_2PO_4	Roth, Karlsruhe, Germany
Sodium dodecyl sulfate	SDS	Merck, Darmstadt, Germany
Sodium molybdate dihydrate	$Na_2MoO_4 \cdot 2\,H_2O$	Roth, Karlsruhe, Germany
Sodium selenite pentahydrate	$Na_2SeO_3 \cdot 5\,H_2O$	Fluka, Buchs, Switzerland
Thiamine hydrochloride	Vitamine B1	Roth, Karlsruhe, Germany
Trifluoroacetic acid	TFA	Merck, Darmstadt, Germany
2-[2-[4-(trifluoromethoxy)phenyl] hydrazinylidene]-propanedinitrile	FCCP	Cayman Chemical, Ann Arbor, US
Tris(hydroxymethyl)aminomethane	TRIS	AppliChem, Darmstadt, Germany
Trypsin/EDTA Solution		PAN-Biotech, Aidenbach, Germany
Tryptone		AppliChem, Darmstadt, Germany
Tween 20		AppliChem, Darmstadt, Germany
Vitamin B1		Sigma-Aldrich, Darmstadt, Germany
XF Dulbecco's Modified Eagle Medium	XF DMEM	Agilent technologies, Santa Clara, US
XF 1.0 M Glucose Solution		Agilent technologies, Santa Clara, US
XF 200 mM Glutamine Solution		Agilent technologies, Santa Clara, US
XF 100 mM Pyruvate Solution		Agilent technologies, Santa Clara, US
Yeast extract		AppliChem, Darmstadt, Germany

2.1.2 Equipment

Table 2: Equipment used for the experiments

Equipment	Model	Manufacturer
Agarose gel analyzer	Biodoc Analyze	Biometra, Goettingen, Germany
CD spectrometer	J-710 Spectropolarimeter	JASCO GmbH, Pfungstadt, Germany
Cell counter	Countess II FL	Thermo Scientific, Darmstadt, Germany
Centrifuge	Centrifuge 5810 R, 5415 R Avanti JE, JLA 9.100	Eppendorf, Hamburg, Germany Beckmann, Krefeld, Germany
Electrophoresis chamber	Mini-PROTEAN Mini-Sub Cell-GT	Bio-Rad, Hercules, US Bio-Rad, Hercules, US
Fast protein liquid chromatography system	BioLogical DuoFlow F10	BioRad, Hercules, US
Fluorescence spectrometer	Varian Cary Eclipse with plate reader FP-8300 JASCO	Agilent technologies, Santa Clara, US JASCO GmbH, Pfungstadt, Germany
Heating block	LS1	VLM, Bielefeld, Germany
Incubator	C200	Labortect, Goettingen, Germany
Liquid chromatography coupled to an mass spectrometer	Orbitrap Elite instrument coupled to an EASY-nLC 1000 liquid chromatography system with an integrated PicoFrit emitter covered by a column oven attached to a nanospray flex ion source	Thermo Fisher Scientific, Waltham, US New Objective, Woburn, US Sonation GmbH, Biberach, Germany Thermo Fisher Scientific, Waltham, US
Microscope	Ti-E inverted wide field, CFI S Plan Fluor ELWD 20x/0.45 DIC objective; CoolSNAP HQ2 interline-transfer CCD camera AMG Evos	Nikon, Chiyoda, Japan Roper Scientific, Martinsried, Germany AMG, Mill Creek, USA
Nano-Photometer	NanoDrop 1000	Peqlab, Erlangen, Germany
Peptide Synthesizer	MultiPep RSi	INTAVIS Bioanalytical Instruments AG, Koeln, Germany
Photometer	BioPhotometer	Eppendorf, Hamburg, Germany
Power supply	PowerPac Basic	BioRad, Hercules, US
Recording device	Amersham Imager 600 GE PR GO15 ECl Chemostar Typhoon FLA 9000 Imaginer	Healthcare Life Science Intas, Florenz, Italy GE Healthcare, Chicago, US
Seahorse Analyzer	XFe24	Agilent Technologies, Santa Clara, US
Semidry blotter	Fastblot B44 iBlot2	Biometra, Goettingen, Germany Thermo Scientific, Darmstadt, Germany
Sterile bench	BDK PR G015	Weisstechnik, Reiskirchen-Lindenstruth, Germany
Thermal cycler	Mastercycler ep 5341	Eppendorf, Hamburg, Germany
Ultrasonic homogenizer	Sonopuls	Bandelin, Hamburg, Germany
Ultracentrifuge	Optima 45Ti	Beckmann, Krefeld, Germany
Ultrashield 700-NMR		Bruker, Billerica, US
UV-Lampe	3UV- 8 W 254/302/365 nm	UVP, California, US
UV/Vis spectrometer	Cary 100Bio	Varian/Agilent, Santa Clara, US

2.1.3 Consumables

Table 3: Used consumables

Consumables	Manufacturer
Affi-Gel 10 Gel and Affi-Gel 15 Gel	BioRad, Hercules, US
BD Falcon Cell Culture Inserts; pore size 8 µm; 24 wells	BD Bioscience, San Jose, US
C18 StageTips; two discs of empore material (3M) in a disc StageTip	In-house production
Centrifugal concentrators, Vivaspin Turbo 15ml, 5 und 30 MWCO	Sartorius, Goettingen, Germany
Disposable PD 10 Columns	GE Healthcare, Chicago, US
Gel 15 Well, 4-12% Bis Tris	Thermo Scientific, Darmstadt, Germany
Gel Filtration Standard from Bio-Rad 151-1901	BioRad, Hercules, US
Gel filtration column, Superdex 75 pg, 16/600, 26/600, 10/300	GE Healthcare, Chicago, US
Glutathione-Agarose Protino 4B	Macherey-Nagel, Dueren, Germany
Nitrocellulose membrane	GE Healthcare, Chicago, US
Petri dishes, different sizes	Greiner Bio-One, Essen, Germany
Pipette tips, different sizes, with and without filter	Sarstedt, Nuembrecht, Germany
Protein A agarose beads	Merck Millipore, Burlington, US
PVDF membrane for iBlot	Thermo Scientific, Darmstadt, Germany
Reaction tube 0.5ml, 1.5ml, 2.0ml	Greiner Bio-One, Essen; Germany
Reaction tube 15ml, 50ml	Sarstedt, Nuembrecht, Germany
Reaction tube Protein LoBind 1.5 ml	Eppendorf, Hamburg, Germany
Reprosil-Pur 120 C18-AQ 1.9 µm resin	Dr. Maisch GmbH, Ammerbuch, Germany
Seahorse XF24 Cell Culture Microplates & Accessories	Agilent Technologies, Santa Clara, US
Serological pipettes, different sizes	Sarstedt, Nuembrecht, Germany
Strep-tag® MagStrep „type3“ XT beads	IBA GmbH, Goettingen, Germany
TC-Flask T75, TC-Plate standard 96 Well	Sarstedt, Nuembrecht, Germany

2.1.4 Buffers and solutions

Buffers and solutions were prepared with demineralized water, in the given order. They were stored at room temperature if not labeled otherwise.

Table 4: Composition of the buffers and solutions

Term/Description	Composition	Remark
Actin buffer	5 mM TRIS pH 8.0 0.2 mM $CaCl_2$ 0.2 mM ATP (from Actin polymerization kit) 5% (w/v) Sucrose 1% (w/v) Dextran	4 °C
Coomassie blue solution	1.25 g Brilliant blue G250 227 ml Ethanol 46 ml Acetic acid ad 500 ml H_2O	
Lysis buffer	10 ml Wash buffer IP 100 ml Phosphatase Inhibitor Cocktail 100 ml Protease Inhibitor Cocktail 0.05 % Igepal	Storage conditions: maximum storage period 14 days at 4 °C

Peptide buffer	0.106 g LiCl Dissolved in 5 mL 2,2,2-TFE	
PBS 10x	14.4 g Na_2HPO_4 2.4 g KH_2PO_4 80 g $NaCl_2$ 2 g KCl ad 1 l H_2O	autoclaved
Stacking gel	2900 µl Bisacrylamide 2200 µl stacking gel buffer (500 mM TRIS pH 6,8) 3500 µl H_2O 85 µl SDS solution 10% 5 µl TEMED 75 µl APS	
SDS sample buffer 5x	12.5 ml Stacking gel buffer 12.5 ml Glycerine 2.5 g SDS 1 mg Bromophenol blue 8% β-Mercaptoethanol	
SDS running buffer 10x	30.3 g TRIS 150.1 g Glycine 10 g SDS in 1000 ml H_2O	
Semi-dry blotting buffer 10x	480 mM TRIS 300 mM Glycine 0.4% SDS in1000 ml H_2O	1x buffer: 100 ml of 10x buffers 70 ml of Isopropanol in 830 ml H_2O
20x TBS	200 mM TRIS pH 7.5 2 M NaCl	
Trace metal stock solution	2 g Na_2EDTA 1.67 g $FeCl_3 \cdot 6\ H_2O$ 500 mg $CaCl_2 \cdot 2\ H_2O$ 18 mg $ZnSO_4 \cdot 7\ H_2O$ 16 mg $CuSO_4 \cdot 5\ H_2O$ 12 mg $MnSO_4 \cdot H_2O$ 18 mg $CoCl_2 \cdot 6\ H_2O$ in 100 ml H_2O	Storage at 4 °C
Separating gel	2900 µl Bisacrylamid 2200 µl Separating buffer (1.5 M TRIS pH 8.8) 3500 µl H_2O 85 µl SDS solution 10% 5 µl TEMED 75 µl APS	
Vitamin stock solution	2 mg Biotin 2 mg Folic acid 5 mg Thiamin 5 mg Pantothenic acid 0.1 mg Vitamin B12 5 mg Nicotinamid 5 mg Riboflavin in 100 ml H_2O	Storage at 4 °C
Regular protein buffer / Wash buffer CO-IP and pull down / Coupling buffer	150 mM $NaCl_2$ 50 mM HEPES (pH 7.5)	
Membrane wash buffer 1 (PBST)	1x PBS 0.05% Tween 20	
Membrane wash buffer 2 (TBST)	1x TBS 0.1% Tween 20	

2.1.5 Media

Table 5: Composition of the used media

Term/Description	Composition	Remark
Basic cell culture medium	DMEM 10% FBS 1% P/S	Sometimes further modified with other nutrients or antibiotics in some experiments
Cross-linking cell culture medium	DMEM-LM 10% FBS 1% P/S 4 µM Photo-leucine 2 µM Photo-methionine	
M9 minimal medium	12.8 g Na_2HPO_4 3 g KH_2PO_4 0.5 g NaCl ad 1 l H_2O 4 g Glucose 2 ml $MgSO_4$ (1 M) 0.1 ml $CaCl_2$ (1 M) 1 ml Vitamin stock solution 1.5 ml Trace metal stock solution 40 mg Kanamycin sulfate	autoclaved
Lysogeny broth (LB) medium	10 g Tryptone 5 g Yeast extract 10 g $NaCl_2$ in 1 l H_2O 40 mg Kanamycin sulfate	pH 7.0 autoclaved

2.1.6 Kit systems and Products

Table 6: Used finished products or kit systems

Description	Manufacturer	Product nr.
ATTO594 NHS-ester	ATTO-TEC GmbH	AD 594-31
Actin Protein: Human Platelet (> 99% Pure)	Cytoskeleton Inc	APHL99
Actin Polymerization Kit	Cytoskeleton Inc	BK003
DNA-Marker mi-100 bp+ and mi-1 kb	Metabion	mi-M8201, mi-M8201
Halt Phosphatase Inhibitor Single- Use Cocktail	Thermo Fisher Scientific	78428
Halt Protease Inhibitor Single- Use Cocktail	Thermo Fisher Scientific	78430
Lipofectamine 2000 Transfection Reagent	Thermo Fisher Scientific	11668030
NucleoSpin gDNA Clean-up	MACHEREY-NAGEL GmbH	740230.250
NucleoSpin Gel and PCR Clean-up	MACHEREY-NAGEL GmbH	740609.250
NucleoSpin Plasmid	MACHEREY-NAGEL GmbH	740588.250
Protein Ladder (PageRuler™ Prestained, PageRuler™ Unstained)	Thermo Fisher Scientific	26616, 26630
SuperSignal™ West Femto Maximum Sensitivity Substrate	Thermo Fisher Scientific	34094
Venor®GeM Classic, Mycoplasma Detection Kit	Minerva Biolabs	11-1025

2.1.7 Enzymes

Table 7: Enzymes used in this work

Enzyme	Application	Manufacturer
α-chymotrypsin	Isomerase assay	Sigma-Aldrich, Darmstadt, Germany
ApaI (normal and fast digest)	Cloning	New England Labs, Frankfurt, Germany
BbsI-HF	Cloning	New England Labs, Frankfurt, Germany
KLD Enzyme Mix	Degradation of template DNA	New England Labs, Frankfurt, Germany
Lysozyme	Cell disruption	Fluka, Buchs, Switzerland
MB Taq Polymerase, hot-start	Mycoplasma test	Minerva Biolabs
PfuPlus! DNA Polymerase	Cloning	Roboklon, Berlin, Germany
PreScission Protease	Protein purification	In-house production (Alma Rute)
Q5® Hot Start High-Fidelity DNA Polymerase	Cloning	New England Biolabs, Frankfurt, Germany
Quick Ligase	Cloning	New England Biolabs, Frankfurt, Germany
T4 Ligas	Cloning	Thermo Scientific, Darmstadt, Germany
T4 Polynucleotid Kinase	Cloning	New England Biolabs, Frankfurt, Germany
XhoI (normal or fast digest)	Cloning	New England Biolabs, Frankfurt, Germany

2.1.8 Peptides measured in the PPIase Assay

Table 8: Peptides used for the PPIase Assay. The peptides have a sequence of Suc-Ala-Xaa-Pro-Phe-pNa, where Xaa is a proteinogenic amino acid. The peptides are listed with their molecular weight (MW). The peptides were synthesized by CASLO (Kongens Lyngby, Denmark) and received in lyophilized form.

Suc-Ala-Xaa-Pro-Phe-pNa	MW [g/mol]	Suc-Ala-Xaa-Pro-Phe-pNa	MW [g/mol]
Ala	623.10	Leu	667.19
Arg	710.30	Lys	681.00
Asn	667.34	Phe	700.02
Asp	669.08	Ser	640.44
Gln	681.40	pSer	720.81
Glu	682.81	Thr	655.44
Gly	610.21	Trp	739.33
His	691.35	Tyr	717.09
Ile	667.07	Val	652.34

2.1.9 Human cell lines

Table 9: Used cell lines

Line	Growth	Mycoplasma test	Verified (cell line typing report)
HeLa CCL2	adherent	negative	by ATCC, US in 2019
HCT116	adherent	negative	Purchased from ATCC, 2008
HEK 293T	adherent	negative	by Microsynth, Germany in 2019

2.1.10 Bacteria and Vectors

BL21 (DE3) T1r competent *E. coli*-cells (Sigma-Aldrich, Germany) were transfected with the plasmids for the expression of proteins and NEB5α cells (New England Biolabs, Germany) were used for the amplification of the plasmid DNA.

Table 10: Vectors with corresponding inserts used in this work.

Term	Basic vector	Insert	Vector Map
BC697	pET41b(+) PreScission	Par14 N-term(Par14$_{\Delta 36-131}$) - Strep Tag	Fig. A13
BC808	pET41b(+) PreScission	Par17	Fig. A13
BC844	pET41b(+) PreScission	PPIase domain (Par14$_{\Delta 1-35}$/Par17$_{\Delta 1-6161}$)	Fig. A13
BC880	pET41b(+) PreScission	Par14	Fig. A13
BC1119	pET41b(+) PreScission	Par17D99A	Fig. A13
BC1356	pET41b(+) PreScission	Par14 N-terminus (Par14$_{\Delta 36-131}$)- Strep Tag TAATAG	Fig. A13
BC1366	pET41b(+) PreScission	Par17 N-terminus (Par17$_{\Delta 61-156}$)-Strep Tag	Fig. A13
BC1405	pSpCas9(BB)-2A-GFP (Abcam 48138)	sgRNA2	Fig. A14
BC1406	pSpCas9(BB)-2A-GFP (Abcam 48138)	sgRNA3	Fig. A14
BC1467	pET41b(+) PreScission	Par17 N-term (Par17$_{\Delta 61-151}$)	Fig. A13
BC1468	pET41b(+) PreScission	Par14$_{\Delta 1-22}$	Fig. A13

2.1.11 Primers

Table 11: Primers

Primer Name	Sequence 5'-3'	Manufacturer
2570	GCAGTTCGAAAAATAATAGCGAGCACCACCACC	Metabion GmbH, Sterinkirchen, Germany
2571	GGTGGTGGTGCTCGCTATTATTTTTCGAACTGC	
2642F sgRNA2 FW	CACCGCCCTTTAGAAGCCCCGCCAT	Microsynth Seqlab, Goettingen, Germany
2643R sgRNA2 RV	AAACATGGCGGGGCTTCTAAAGGGC	
2644F sgRNA3 FW	CACCGTGTTTAGGACATGCCCATGG	
2645R sgRNA3 RV	AAACCCATGGGCATGTCCTAAACAC	
2646 ssODN template	AAGAACGGTCAATTGAGATGCGGCTTTCAGGCATTTGTTT AGGACGTGCCCATGGCGGGGCTTCTAAAGGGGCTTGTACG GCAACTGGAGCGG	
2648F gDNA primer	CTTTGTCTCCGCCCCTCTGCCTTTG	
2649R gDNA primer	ACTGTCTGTTCCCTCCCTTCGCTCC	
2713R	TTGGTTCTCGAGCTATTAGCCACCACCTTTGGGACCTTGAGC	

2.1.12 Antibodies

Table 12: Primary and secondary antibodies used in this worl

Description	Conjugation	Species	Manufacturer	Product nr.
Anti-Actin antibody		Mouse	MP Biomedicals	6911
Anti-Beta Actin polyclonal antibody		Rabbit	Elabscience	A-AB-20058
Anti-Mouse IgG	HRP	Goat	Invitrogen	32260
Anti-Par17 antibody polyclonal		Rabbit	Ab-extraction	Müller 2006 [89]
Anti-Rabbit IgG	HRP	Goat	Siegma-Aldrich	A-9169
Total OXPHOS Rodent WB Antibody Cocktail		Mouse	Thermo Fisher Scientific	ab110413

2.1.13 Software

Table 13: Software used in this work listed with the corresponding manufacturers

Software	Use	Manufacturer
Adobe Illustrator	Photo editing	Adobe Inc., California, US
BioGrid$^{4.2}$	Interaction partner analysis	TyersLab.com [133]
BioLogic	BioRad FPLC Programming	BioRad, Hercules, US
CARA 1.2	NMR	The Wüthrich Group [58]
Cary WinUV	UV/Vis-spectral recording	Varian, Santa Clara, US
CcpNMR Analysis 2.4	NMR	Plone Foundation, Cambridge, UK [152]
Cell Profiler	Cell counting	Broad Institute, Massachusetts, US [86]
GraphPad Prism	Statistical analysis, curve fitting	GraphPad Software, California, US
HADDOCK 2.4	Protein-protein interaction	Bonvin Lab, Utrecht, Netherlands [151]
I-TASSER	Model calculation	Zhang lab, University of Michigan, US [161]
Microsoft Office Word, Excel, Powerpoint	Word processing, spreadsheet preparation, presentation	Microsoft Corporation, New Mexico, USA
NIS Elements AR software	Cell counting, cell migration	Nikon, Netherlands
Perseus V1.5.5.3	Interaction analysis	Max-Planck-Institute of Biochemistry, Planegg, Germany [144]
PyMol		
StavroX 2.0	Cross-link analysis	Michael Götze, Halle, Germany
STRING V11.0	Network analysis	STRING Consortium 2020 [138]
TopSpin 3.5	NMR	Bruker, Massachusetts, US
Wave V2.6	Seahorse Mito Stress Test	Agilent technologies, Santa Clara, US
YASARA	Model simulation	YASARA Biosciences GmbH, Austria [66]
XiNET –Cross-link Viewer	Cross-Linking experiments	Rappsilber Laboratory, Berlin, Germany [18]

2.2 Methods

2.2.1 Cloning and DNA Transformation in *E.coli*

For Par14 and Par17, Par17$_{D99A}$ and the PPIase domain vectors previously described were used (pET-41 vector with an N-terminal GST-His6 fusion followed by a PreScission protease cleavage site and the protein of interest) [61].

The vector BC697, the modified pET-41 vector, containing the Par14 N-terminus (Par14$_{\Delta 36\text{-}136}$-Strep) ending with a Strep-tag II lacks a second stop codon which was added by side directed mutagenesis. For the mutagenesis, the polymerase Q5 Hot start was used with the primers 2570F and 2571R. For the degradation of the template DNA, the KLD Enzyme Mix was used. All steps were performed according to the manufacturer's protocols.

The DNA of the Par17 N-terminus followed by a Strep-tag II (Par17$_{\Delta 61\text{-}156}$-Strep) were inserted in the modified pET41 vector. The Pfu Plus Polymerase with the primer 2572F and 2573R were used as prescribed by the manufacturer. The NucleoSpin Gel and PCR Cleanup kit was used for purification PCR products. For restriction, ApaI and XhoI were applied for 1 h at 37 °C for the insert and the vector. The enzymes were inactivated at 65 °C for 10 min. The constructs were separated on an agarose gel and purified with the NucleoSpin Gel and PCR Clean-up kit according to the manufacture's instructions. The cleaved constructs were ligated with the T4 ligase for 1h at 16 °C. The DNA of the Par17 N-terminus (Par17$_{\Delta 61\text{-}156}$) were inserted in the modified pET41 vector as described for its Strep-tagged form, only the primer 2573R was replaced by 2713R.

The guide sequence of the sgRNA was cloned into the pspCas9(BB)2A-GFP vector for co-expression with Cas9. The pair of oligonucleotides were annealed and phosphorylated with the T4 Polynucleotid kinase. Paired oligonucleotides (sgRNA2, sgRNA3) and the vector were digested by BbsI-HF and ligated by Quick Ligase in accordance with the company's instructions.

Transformation. Transformation was performed with the head shock method. The competent *E.coli* strains were mixed with the plasmid DNA (around 50 ng) and incubated on ice for 20 min. Afterwards the suspension was heat shocked at 42 °C for 30 sec and placed on ice for further 5 min. The cells were supplemented with SOC medium and then incubated for 1 h at 37 °C. Then the *E.coli* cells were either directly added to media for cultivation or grown on an agarose plate, each with required selective antibiotic.

2.2.2 Protein expression and purification

Transformed bacteria were grown in LB medium or, for NMR experiments, in M9 minimal medium at 37 °C upon an $O.D._{600}$ of 0.8. The protein expression was induced by adding 200 µl of a 1 mM IPTG stock solution to 1l of medium and cells were incubated overnight at 30 °C and 160 rpm. For labeling of the proteins with photo-reactive amino acids, the cells were grown in M9 minimal medium as described, with the minor modification that at $O.D._{600}$ of 0.6, L-photo-leucine and L-photo-methionine (20 mg each) were added to the media.

For cell lysis, 100 ml PBS, Lysozyme (1mg/ml) and PMSF (final concentration 1 mM) were added to the cell pellet and the solution was mixed at 4 °C for 1 h. The solution was sonified by ultrasonic homogenization (5 x 50 sec, with 1 min intervals at 60% sound intensity). The lysate was centrifuged at 100000 x g for 1 h and the supernatant was filtered.

The GST-tagged proteins were purified from the cell extract by affinity chromatography. For this purpose a GSH column was equilibrated with PBS and the supernatant was loaded on the column and washed with a high salt buffer (400 mM $NaCl_2$ in PBS) followed by a PBS washing step. The GST-tagged proteins were detached by elution buffer (20 mM glutathione in PBS). The protein fractions were concentrated and the GST fusion was cleaved by PreScission protease. To yield pure protein, size exclusion chromatography was performed (50 mM HEPES, 150 mM NaCl, pH 7.5 or for NMR for Par14/PPIase 50 mM KPi buffer pH 6.4-6.8 and for Par17 50mM KPi , 50mM $NaCl_2$, 7mM β-mercapthoethanol pH 8.0 or 50mM HEPES, 150 mM $NaCl_2$). The protein fractions were concentrated again and if later measurements required a different buffer, the proteins were rebuffered three times in the desired buffer. The actual protein concentration was determined by measuring the O.D. at 280 nm and using the extinction coefficients calculated from the amino acid sequences, ,excepted for the N-terminus of Par17 without a tag, it was determined by the Bradford method.

2.2.3 Protein cross-linking

DSSO cross-linking. The MS-cleavable cross-linker DSSO was used in this work to investigate the intramolecular interactions of proteins. DSSO was dissolved in DMSO as a stock solution with a concentration of 50 mM. In 300 µl of solution the final DSSO concentration was 3.3 fold higher than the protein concertation (Par14, 0.3 mM; Par17, 0.15 mM). The mixture was incubated for 1 h at 25 °C and the reaction was stopped with TRIS buffer (final concentration 1 mM, pH 7.5). The monomeric and dimeric species were separated by analytical size exclusion chromatography (50 mM HEPES, 150 mM $NaCl_2$, pH 7.5) and comparison of the signals to the signals of a molecular weight marker with the range of 1350 Da to 670000 Da was performed.

For DSSO cross-linking of actin and Par17 both were mixed (10 µM and 25 µM respectively in a total volume of 140 µM; 50 mM HEPES, 150 mM $NaCl_2$, pH 7.5) and incubated for 30 min at 4 °C. DSSO was added in a 3.3 fold excess (0.8 mM) and the reaction was stopped after 10 min with TRIS buffer. Probes were taken before and after cross-linking for an SDS-gel.

For mass spectrometry analysis, all DSSO cross-linked samples were digested in solution (Section 2.2.6).

Photo cross-linking. The photo reactive amino acids were used to cross-link intra and intermolecular interactions. Firstly, the amino acids were incorporated in the recombinant proteins and purified (Section 2.2.2). To study the intramolecular cross-links within the proteins the solution of labeled proteins (250 µl of Par14, 0.2 µM and Par17, 0.07µM) was irradiated with UV light of 365 nm for 30 min one ice with a distance from the UV source of 1 cm. Next, the separation of monomeric and dimeric species was performed, as described in the case of DSSO cross-linking. For mass spectrometry analysis, the samples were digested in solution (Section 2.2.6).

To identify intermolecular interactors of full-length proteins the photo amino acid labeled proteins (25 µg) were added to HeLa cell lysate (200 µl, protein concentration ~3 mg/ml). The mixture was irradiated with a distanced of 1 cm with UV light for 30 min on ice. To identify intermolecular interactors of the N-termini of Par14 and Par17 these proteins (final concentration of 20 µM in 300 µl) were added to photo amino acid labeled HeLa cell lysate (final concentration ~2 mg/ml). Since the N-termini are tagged with a Strep-tag, a Strep-tag II peptide (AA: Trp-Ser-His-Pro-Gln-Phe-Glu-Lys, purchased from Caslo, Denmark) was added as a control to labeled HeLa cell lysate in the same concentration as well. The samples were irradiated as described above. For mass spectrometry analysis, the samples were digested on the beads (section 2.2.6)

2.2.4 CD spectroscopy

To measure CD-spectra, proteins were diluted with salt free buffer (50 mM potassium phosphate buffer, pH 7.5) to a final concentration of 25 µM in 200 µl volume. Measurements were performed at 25 °C and the spectrum of the buffer was subtracted for baseline correction.

2.2.5 Immunoprecipitation and pull down of proteins and interactors

Immunoprecipitation of Par14/17. The recombinant full-length proteins Par14/17 were isolated from the cell lysate by immunoprecipitation. The PIN4 antibody was first immobilized on protein A agarose beads. 100 µl of the beads were washed once with lysis buffer and two times with wash buffer and incubated overnight at 4 °C with the antibody (5 µg) in washing buffer. To separate the beads from the suspension they were centrifuged for 1 min at 4 °C at 1000 rpm after each step. The beads were incubated with the irradiated samples for 4 h at 4°C and were washed three times. Supernatants of each step were collected and prepared for western blot analysis (presented in Goehring et al. [37]).

Pull down of Strep tagged Proteins. The Strep II tagged N-termini were isolated from the solution by pull down. 50 µl of the Magnetic Strep-Tag Beads were washed two times. The irradiated samples were incubated with the beads overnight at 4 °C and washed with washing buffer three times.

The proteins that were bound to the beads were digested directly on the beads with trypsin (cooperation with the Analytics Core Facility Essen (ACE)).

2.2.6 Mass spectrometry

Sample clean-up for Liquid chromatography–mass spectrometry (LC-MS). Subsequently after on-bead digestion or in solution digestion with trypsin, peptides were desalted on home-made C18 StageTips [108]. The digests were passed twice over StageTips and the immobilized peptides were washed twice with 0.5% FA and eluted from the StageTips using 80% ACN with 0.5% FA. Drying was done by using a vacuum concentrator and peptide samples were resuspended in 10 µl 0.1% FA before LC-MS (Preparation was done jointly with the help of Svenja Blaskowski, AG Kaiser, ACE Facility).

LC–MS/MS. Experiments were performed with an Orbitrap Elite or Orbitrap Fusion Lumos instrument coupled to an EASY-nLC 1000 or 1200 (LC) system. A fused silica capillary (75 µm × 35-46 cm) with an integrated PicoFrit emitter packed in-house with Reprosil-Pur 120 C18-AQ 1.9 µm covered by a column oven (45-50°C) was utilized. The column was attached to a nanospray flex ion source. Peptides were loaded onto the column and separated with a maximum flow rate that would not exceed the set pressure limit of 980 bar and using different gradients (for detail setting see appendix table 1)

The mass spectrometers were operated using Xcalibur software (Elite: v2.2 SP1.48; Lumos: v4.3.7.3.11). The mass spectrometers were set in the positive ion mode. Precursor ion scanning (MS1) was performed in the orbitrap analyzer (FTMS; Fourier Transform Mass Spectrometry) with the internal lock mass option turned on (lock mass was 445.120025 m/z, polysiloxane) [93]. MS2 Product ion spectra were recorded only from ions with a charge bigger than +1 and in a data dependent fashion in the ion trap (IT) MS or FTMS. (All relevant MS settings: Resolution, scan range, automatic gain control, ion acquisition time, charge states isolation window, fragmentation type and details, cycle time, number of scans performed, and various other settings for the individual experiments can be found appendix table 2).

Data analysis of experiments with DSSO. The crosslinking experiments with parvulin monomers and Par17 with Actin were analyzed in Thermo Scientific Proteome Discoverer (PD, version 2.2) with the add-ons SEQUEST for the identification of non-cross-linked peptides and XlinkX for the identification of cross-linked peptides [75]. The search was performed against the Uniprot *E. coli* reference database concatenated with the respective sequence of interest (details settings see appendix table 3).

Data analysis of photo cross-linking experiments. Identification of intramolecular photo cross-links was performed with StavroX 3.6.6 [39]. To this end, the RAW files were converted to the mzML format using Proteome Discoverer (details settings see appendix table 3).

The photo cross-linking data of the labeled proteins with cell lysate was analyzed with the software MaxQuant (version 1.5.3.30 or 1.6.3.4) [20] and submitted to an Andromeda search at default settings [21] and activated label-free quantification [19]. Based on the Uniprot *Homo sapiens* reference proteome database (UP000005640_9606.fasta; 20679 entries, one protein sequence per gene, downloaded from 07.08.2019) and a database with known contaminants, spectra were searched for valid proteins (details settings see appendix table 3). The instrument type in Andromeda searches was set to Orbitrap and the precursor mass tolerance was set to ±20 ppm (first search) and ±4.5 ppm (main search). The MS/MS match tolerance was set to ±0.5 Da. The peptide spectrum match FDR and the protein FDR were set to 0.01 (based on target-decoy approach). Minimum peptide length was 7 amino acids. For protein quantification unique and razor peptides were allowed. Modified peptides were allowed for quantification. The minimum score for modified peptides was 40. Label-free protein quantification was switched on, and unique and razor peptides were considered for quantification with a minimum ratio count of 2. Retention times were recalibrated based on the built-in nonlinear time-rescaling algorithm. MS/MS identifications were transferred between LC-MS/MS runs with the “match between runs” option in which the maximal match time window was set to 0.7 min and the alignment time window set to 20 min. The quantification is based on the “value at maximum” of the extracted ion current. At least two quantitation events were required for a quantifiable protein (Measurements of mass spectrometry data and analyzation of spectra were done by Farnusch Kaschani, AG Kaiser). For further data analysis the LFQ intensities from the proteinGroups.txt file were loaded into the program Perseus 1.5.5.3 [144]. The categories contaminants, reverse hits and hits only identified by site were removed. The four replicates of each sample were categorized into groups for statistical calculations. Only the proteins that are present in three valid values in at least one of the groups were further processed. Comparison of protein group quantities (relative quantification) between different MS runs is based on the LFQ’s as calculated by MaxQuant, MaxLFQ algorithm [19].

Protein-protein interaction (PPI) network analysis. Proteins significantly enriched by MS were analyzed for interactions between proteins by the Search Tool for the Retrieval of Interacting Genes (STRING; version 11.0) [138]. STRING is a database of known and predicted protein-protein interactions. The gene names of the significantly enriched proteins were used to search their interactions. The interaction network is calculated by a spring model based on the interactions scores of the genome of *Homo sapiens*. Each protein is visualized by a colored sphere and the interaction is indicated by lines. Interaction partners in the PPI network were depicted when the score was > 0.4 (medium confidence). The confidence of the interaction is reflected by the thickness of the lines. Clusters of the interactors are calculated by the Markov Cluster Algorithm based on the score specified with an inflation parameter of three and visualized by the same sphere color.

2.2.7 Protease-coupled isomerase assay (PPIase Assay)

To determine the isomerase activity of the parvulins and derived forms a PPIase Assay was used. Therefore, the lyophilized peptides (table 9) were weighed on a digital fine scale and dissolved in an adequate volume of 0.5 M-LiCl/TFE buffer to obtain a 15 mM stock solution. To achieve a stable *cis*/*trans* ratio the mixture was incubated overnight at 4°C. The next day a stock solution of 350 µM α-chymotrypsin in PBS was prepared and incubated on ice for at least 20 minutes. First the thermic measurements were performed. PBS buffer (pH 6.8) were mixed with α-chymotrypsin to a final concentration of 35 µM in 1 ml. A baseline was recorded for 5 min (Cary 100Bio UV/Vis spectrophotometer, λ: 390 nm, bandwidth: 1.0 nm, average time between measurements: 0.5 sec, temperature: 10 °C). At the time point of 5 min the substrate peptide was added to a final concentration of 75 µM in 1 ml. The solution was mixed swiftly by inverting the cuvette three times and the reaction was recorded for a further 15 min. Afterwards, the catalytic measurement was performed in the same way, except that before the baseline measurement, the appropriate isomerase was added in a final concentration of 2 µM in 1 ml in addition to PBS and α-chymotrypsin. For the linearity measurements, the final concentration of Par17 was varied. For the K_M determination, the final substrate concentration was varied and the measurement times were shortened (baseline measurement: 2 min, reaction measurement: 1 min).

For the data analysis, a mean value of the baseline was subtracted (average of the first 200 data points). The measured values were normalized with the respective maximum of the measurement. To determine the rate constant, the program graph pad was used and non-linear curve fitting was applied for each individual measurement (Equation 1: exponential, one phase association).

$$Y= Y_0+(\text{Plateau}- Y_0)\cdot(1-e^{(-K\cdot x)}) \qquad \text{Eq. 1}$$

x: time [min]
Y: absorbance
Y_0: absorbance when x=0
Plateau: Y value at infinite times
K: rate constant [min^{-1}]

The K_{cat}/K_M value was calculated as demonstrated in equation 2.

$$\frac{k_{cat}}{K_M} = \frac{k_{obs} - k_{therm}}{[\text{PPIase}]} \qquad \text{Eq. 2}$$

k_{cat}/K_M: catalytic efficiency [$M^{-1}s^{-1}$]
k_{obs}: rate constant of the observed reaction [s^{-1}]
k_{therm}: rate constant of the thermic reaction [s^{-1}]
[PPIase]: concentration of PPIase used in the assay [M]

For the K_M determination, the slope of the first 10 data points of each measurement was fitted linearly and the slope of the thermal reaction was subtracted. For the conversion of absorption per time into converted molecules per time, a calibration curve of free pNa had to be measured. For this purpose, absorbance of different concentrations of free pNa in water was determined (Alma Rute) and the slope of the linear fit was calculated. Subsequently, the slope of the catalytic reaction could be divided by the slope of the calibration line and resulted in the molecules converted per time.

2.2.8 Nuclear magnetic resonance spectroscopy (NMR)

For NMR measurements, purified and concentrated proteins in salt free buffers were mixed with 10% D_2O and 1 µl DSS standard. Spectra were measured with an ultrashield 700-NMR with a triple resonance cryo probe (700 MHz). For recording and processing of the date the software Topspin 3.5 was used. To analyze the spectra Cara analysis software 2.3.1 and CcpNMR analysis 2.3.1 were utilized.

Comparison of full-length proteins with the PPIase domain. To compare the ^{15}N-labeled full-length Par14 and Par17 with the catalytic PPIase domain each was measured with the ^{15}N-HSQC pulse program hsqcetf3gpsi2 from the Bruker standard bibliotheca at 25 °C under the same buffer conditions (50 mM potassium phosphate buffer, pH 6,4). To analyze the spectra the software CcpNMR analysis 2.3.1 was used. The presence of new amino acids in a protein (full-length) could change the chemical environment of the other amino acids of the protein. This could induce chemical shift changes of the signal of a single amino acid in the spectra. The calculation of chemical shift changes between the same peaks of different constructs was performed with the following equation:

$$\Delta\delta = \sqrt{(\Delta\delta_H)^2+(\Delta\delta_N\cdot 0{,}154)^2} \qquad \text{Eq. 3}$$

$\Delta\delta$: combined chemical shift
$\Delta\delta_H$: chemical shift in the H-dimension
$\Delta\delta_N$: chemical shift in the N-dimension

Titration of substrate peptides to ^{15}N labeled parvulins. The Glu-Xaa, Val-Xaa (12.5 mM stock solution), Lys-Xaa and Gly-Xaa (15 mM stock solution) substrate peptides were diluted in salt free 50 mM KPi buffer pH 6.7. There were added stepwise to 200 µl of the labeled parvulins, the isolated catlytic domain or Par17’s N-terminus (about 200-300 µM in 50 mM potassium phosphate buffer pH 6.7). Spectra were recorded with the pulse program Best-TROSY at 20 °C. Upon addition the unlabeled substrate, shifting of signals and/or decrease in relative intensity can be monitored for amides in close vicinity of the binding site due to line broadening. Combined chemical shifts between the same, but shifted peaks were calculated as described in Eq.3. The microscopic dissociation constant K_D was fitted with the following equation 4 (assuming a 1:1 binding model):

$$\Delta\delta = \Delta\delta max * \frac{(P+x+K_D)-\sqrt{(P+x+K_D)^2-(4\cdot x\cdot P)}}{2*P} \qquad \text{Eq. 4}$$

$\Delta\delta max$: amplitude
P: Protein concentration
X: concentration of the peptide

The microscopic K_D describes the binding affinity of the ligand to the single amino acid. This does not have to correspond directly to the binding of the ligand to the protein.

Intensity changes in ^{15}N labeled Par17 upon addition of actin. Actin in actin-buffer was added to 200 µl of ^{15}N labeled Par17 (348 µM, in 50 mM potassium phosphate buffer, pH 6.6). Actin was added to a final concentration of 45 µM. Spectra were recorded with the pulse program Best-TROSY at 25 °C. As control, an equivalent amount of pure actin buffer was added (published in Goehring et al., [37]). The intensities of single resonances within the spectrum in absence (I_0) and presence of actin (I) were determined. The normalized intensities were calculated for each residue and for better depiction the mean value of all intensity ratios was subtracted from each normalized intensity as indicated in equation 5.

$$x = \left(\frac{I}{I_0}\right) - \frac{1}{n}\sum\left(\frac{I}{I_0}\right) \qquad \text{Eq. 5}$$

I: Intensities of single resonances within the spectrum in presence of actin
I_0: Intensities of single resonances within the spectrum in absence of actin

2.2.9 Actin polymerization assay

To measure the ability of PPIases to polymerize human actin the actin polymerization kit and non-muscle actin from humans was used. The assay was performed according to the manufacturer’s instructions. In the assay, the fluorescence enhancement is measured. This occurs when in dependency of non-muscle human G-actin, pyrene-labeled rabbit muscle G-actin (monomeric) forms F-actin (polymeric). Briefly, the parvulin isoforms (100 mM TRIS buffer, pH 7.5) were added to the G-actin solution with a final assay volume of 110 µl and polymerization was measured for 30 min at an excitation of 365 nm and an emission of 407 nm at room temperature (Varian Cary Eclipse Fluorescence Spectrophotometer).

2.2.10 Atto594 labeling of proteins and fluorescence anisotropy

Par17, Par14 and GST were labeled with Atto594 NHS-ester according to the company’s instructions. In short, the NHS-ester was dissolved as a stock solution in DMSO (20 mg/ml). Then solution was added to ~2 mg protein (in 1.1-fold molar excess) in a volume of 1 ml and incubated for 1 h at 24 °C and 400 rpm. The reaction was stopped by adding 10 µl of 1 M TRIS. The labeled protein was separated from the free dye over a disposable PD-10 column with the use of the regular protein buffer. Labeled Proteins were dissolved with actin buffer to a final concentration of 100 µM in 55 µl measuring volume. Anisotropy was measured (FP-8300 JASCO,

$\lambda_{excitation}$=604 nm, $\lambda_{emmission}$=604 nm) while adding non-muscle human actin up to a concentration of 60 µM. Atto594-GST was measured for control and Atto594-Par14/17 measurements were carried out in three replicates. GraphPad Prism were utilized to calculate a binding curve and a dissociation constant K_D based on a one-site-specific binding model.

2.2.11 Peptide Spotter Array

Actin peptide libraries were produced by automatic SPOT synthesis by Fmoc (9-fluorenylmethyloxycarbonyl) chemistry on Whatmancellulose 50 membranes (Peptide Synthesizer, by Helmut Tourné, AG Ehrmann). The dried membranes were activated in 100 % ethanol for 10 minutes, washed with PBS and incubated with blocking buffer (5 % BSA in PBS) for 1 h at room temperature. Next they were incubated overnight with Atto594 labeled Par14/Par17 and free dye for control. Membranes were washed with PBS and dried at 37 °C. Followed by the detection of the bound proteins (Typhoon FLA 9000 Imaginer $\lambda_{excitation}$=523 nm, $\lambda_{emission}$=665 nm).

2.2.12 SDS-PAGE and Western blot

Cell extract or protein fractions and samples were supplemented with 5 x SDS sample buffer and boiled at 95 °C for 5 min. Samples were loaded onto a self-cast SDS-Gel (separating and stacking gel) and run in 1x SDS running buffer at a constant voltage of 120V. The proteins in the gels were ether stained with coomassie blue solution or transferred to a nitrocellulose membrane for western blotting with a constant current of 150 mA for 1 h using 1x semi-dry blotting buffer. After blotting, membranes were stained with Ponceau S dye and blocked for 1 h (5% skim milk powder (MP) in PBST). Primary antibody was diluted (Par17 antibody 1:500, β-actin antibody 1:1000 in PBST) and incubated with the membrane overnight at 4 °C. PBST was added to the membrane 3 times for 5 minutes followed by the secondary antibody in the appropriate dilution (anti-Rabbit, 1:5000 in PBST) for 2 h at room temperature. The membrane was washed 5 times for 5 min, and to detect the protein, was then incubated for 5 min with SuperSignal™ West Femto Maximum Sensitivity Substrate.

For the analysis of OXPHOS complexes, the cell lysates were placed on a purchased 15-well gel 4%-12% Bis Tris and separated at 200 V for 25 min in MES SDS Running buffer. Subsequently, the proteins were transferred to a PVDF membrane using the standard program P0 (20V 1min, 23V 4min, 25V 2min) in the iBlot2 dry blotting system. The membrane was first blocked (5% MP in TBST) and then incubated overnight at 4 °C with the OXPHOS antibody cocktail (1:1000 in TBST). The next day the membrane was washed twice and incubated with the secondary antibody for 1 h (anti-Mouse, 1:1000 in TBST). The blot was washed three time and incubated for 5 min with SuperSignal™ West Pico PLUS Substrate. After detection, HRP was inactivated by incubation of the membrane with 8% acetic acid for 10 min. The membrane was washed three times for 5 min and incubated with the loading control antibody for 1 h at RT (anti-actin 1:1000 in TBST). The second antibody (anti-Mouse, 1:1000 in TBST) was added after two washing steps and remains on the membrane for 1 h. The membrane was again incubated with the substrate and signals were detected.

2.2.13 Antibody purification from rabbit antiserum

The antiserum from rabbit against the mixture of Par17 peptides KGLVRQLERFS and KGLVRQLEQFR peptides (Müller 2006) was used for affinity purification of the polyclonal antibodies against Par17. First, Par17 protein (7 mg) was coupled to the mixture of 4/5 Affi-Gel 10 and 1/5 Affi-Gel 15 according to the manufacturer’s description with the use of coupling buffer at 4 °C. The gel mixture was packed into a column and the remaining active ester of the gel was blocked with 0.1 M ethanolamine (pH 8.0). 5 ml of the inactivated antiserum (incubation at 56 °C for 1 h) was added to the pre-washed column (5 ml PBS; 2 ml 0.2 M glycine; 5 ml PBS) and was incubated for 2 h at 4 °C. After the antiserum flowed through the column three washing steps (5 ml PBS; 5 ml 1 M $NaCl_2$ within PBS; 5 ml PBS) were performed. The antibody bound to Par17 was eluted 8 times by adding 250 µl of 0.2 glycine flow through the column into a tube with 100 µl of 1 M TRIS and 0.2 M KCl buffer.

2.2.14 Cell culture

Cells were grown in a humidified atmosphere with 5% CO2 at 37 °C in their appropriate media. For incorporation of photo amino acids cells at confluency of 70-80% were first washed twice with PBS and then treated with cross-linking cell culture media for 24 h. For cell lysis, cells (usually 70-80 % confluent) were washed once with PBS and lysis buffer was added. Cells were scraped off the dishes and incubated in tubes on ice for 30 min and mixed every 10 min by vortexing. After centrifugation for 15 min at 16000 x g the supernatant was transferred as cell lysate into a new tube.

2.2.15 Migration assay of Par14 and Par14/17 knockdown cells

A lentiviral shuttle system was used by Irena Michin (AG Bayer) to introduce a stable shRNA interference of Par14 or Par14/17 and thereby knockdown the proteins in human HCT116 cells. The mRNA levels were tested by her with real time PCR and showed a reduction of 80% for the Par14 knockdown cell lines pLKO-sh228 and pLKO-sh311 and of 70% for the Par14/17 cell lines pLKO-sh83 and pLKO-sh90 [37]. Knockdown of around 50% on protein levels was demonstrated by western blot (published in Goehring et al., [37])

Migration Assay. HCT116 cells (wild type; empty vector; siRNAs 311, 228, 90 and 83) grew in serum free medium with 0.1 % BSA (migration medium) overnight and $5 \cdot 10^5$ cells were placed on collagen coated, BSA blocked cell culture inserts (pore size 8 µM). The inserts were placed into a 24-well with 400 µl migration medium and incubated (37 °C and 5 % CO_2 for 6 h). The cells were washed, fixed with formaldehyde and after additional washing they were stained with DAPI (1 µg/ml DAPI in PBS with 0.2 % Triton X100). Non-migrated cells on the inside of the inserts were scraped off with cotton swaps. Afterwards, inserts were subjected to microscopy and recorded with three different appropriate DAPI filter sets. 25 areas (0,15 mm^2 each) chosen by chance were captured per sample, filter and the number of cells was counted. (Migration assay was carried out by Tina Gerdes, AG Bayer and microscopy were performed by Nina Schulze, Imaging Centre Campus Essen) [37].

2.2.16 CRISPR induced knockdown of Par17

HEK293T cells grown on a 24 well plate were transfected either with vector BC1405 (500 ng) and the ssODN template (1 µl of 10 µM solution) or only with vector BC1406 (500 ng). Lipofectamin 2000 reagent was used for the transfection according to the manufacture’s protocol. After 48 h the cells were dissociated, counted with the cell counter and diluted to a final concentration of 60 cells per 12 ml. The solution was distributed on a 96 well plate. The plates were checked after one week for single cell colonies and these were allowed to grow for three to five weeks depending on the growth rate. When sufficient cells were available, the gDNA was extracted with the NucleoSpin gDNA Clean-up Kit according to the manufacturer's instructions, sequenced (by Microsynth, SEQLAB with the gDNA sequence primer) and examined for changes. In addition, cell lysates were prepared as described in 1.2.10 and the protein level of Par17 was determined by western blot.

2.2.17 Seahorse XF Cell Mito Stress Test

The Agilent Seahorse XF Cell Mito Stress Test on a Seahorse XFe24 Analyzer instrument was performed according to the manufacturer's specifications. One day prior to the assay, the cells were counted and were plated into wells with the ideal cell number on the XF cell culture microplates. The cells were cultured in basic cell culture media overnight. On the day of the assay, the medium was changed to the freshly prepared XF assay medium (XF Base Medium with 10 mM glucose, 2 mM glutamine and 1 mM pyruvate) and incubated for 1 h at 37 °C in a non-CO_2 incubator. During incubation, the stock solutions of the compounds (10 µM Oligomycin, 20 µM FCCP, 10 µM Rotenone/antimycin A diluted in assay medium) were loaded into the ports of the sensor cartridge. The sensor cartridge was placed on the XF cell culture plate and the measurement was started. The device measured the oxygen consumption rate. At different time points, the compounds were added and were thereby diluted 1:10. After completion of the assay, cells were fixed (formaldehyde 4 %, 20 min; washed with PBST) and stained with DAPI (diluted in PBST 1:1000; washed twice with PBST). An image was captured from each well and the number of cells was determined using the program cell profiler. Data analysis was performed using the Seahorse XFe Wave software and the cell number was inserted for data normalization.

2.2.18 Model calculation with YASARA

Model of Par17. A model for Par17 was calculated using the software I-TASSER, with the sequence of Par17 and the known structure of the PPIase domain (PDB ID: 3UI6 [91]) that is equal between Par14 and Par17 as the input. Molecular dynamics simulations of the model generated by I-TASSER were performed using the YASARA Structure Suite (v11.12.31) with a YASARA2 force field [65] using the experimental cross-links between the PPIase domain and the N-terminus as distance restraints. Additionally, all amino acids within the PPIase domain that did not shift when the N-terminus of Par17 were present were fixed, with the exception of the amino acids that were part of a cross-link. For the simulation, the cubic simulation cell size was 78.5 Å per edge. The simulation was performed with an explicit water model, periodic boundaries and drift correction. The temperature was set at 298 K and the simulation was run with 0.9% (m/m) NaCl, pH 7.4 with 2.5 fs step width and 7.8 Å cutoff for Van der Waals and real-space Coulomb forces.

2.2.19 Haddock

Model of the Par17 and actin complex. The interaction of the Par17-actin complex was modelled in HADDOCK using a cryo-EM structure of one actin domain (PDB-ID: 6ANU [154]) and the I-TASSER-generated Par17 model on the basis of the calculated PPIase domain structure. The ambiguous interaction restrains of Par17 were defined by the NMR experiments. All amino acids that showed chemical shift changes after actin addition were included. For actin, ambiguous interaction restrains were defined as amino acids bound by Par17 in the spotter array that are exposed on the surface of actin. The inter-domain crosslinks obtained by DSSO cross-linking were used as unambiguous restraints for docking (Table A17). Default HADDOCK scaling for energy terms was applied. Rigid body docking resulted in 1000 complex structures, and the best 200 lowest energy structures were selected for semi-flexible and water refinement. The scoring function yielded a single clear ensemble with a HADDOCK score of 652.7 +/- 8.2. A molecular dynamic simulation of the Par17-actin complex was subsequently performed with YASARA. The settings from the YASARA section were used and the inter-domain DSSO cross-links between actin and Par17 were used as distance restraints.

3 Results

In this work, Par17 that has 25 additional amino acids in the beginning of the N-terminus compared to its shorter isoform Par14 was the focus. The significance of the N-terminal 25 amino acids for the catalytic and biological function of this protein was investigated.

3.1 Comparison of the $^1H^{15}N$-HSQC spectra of Par14 and Par17

The impact of the N-terminus on the catalytic PPIase domain was determined with NMR spectroscopy (Section 2.2.8). For the measurements, ^{15}N-labeled GST-tagged proteins were expressed by *E.coli* and purified with affinity chromatography (Section 2.2.2). Thereafter the GST-tag was cleaved and separated from the target proteins by gel size exclusion chromatography (Fig. A1). $^1H^{15}N$-HSCQ spectra were recorded from Par14, Par17 and the PPIase domain under the same conditions (50 mM KPi buffer with a pH of 6.4, 25 °C). The $^1H^{15}N$-HSCQ spectra show N-H correlations of each residue that has a slow or moderate exchange with water and each residue that is stable. Therefore, residues with the exception of proline and the first N-terminal amino acid are represented in the spectra by a peak. The visible peaks were assigned to the corresponding residue of the proteins based on the assignment of Par14 and Par17 of Sekerina et al. [128] and Lin et al. 2013 [74]. If the N-terminus of Par14 or Par17 interact with the catalytic domain, then the chemical environment of the amino acids forming the PPIase domain will change. This in turn becomes visible in chemical shift changes of the $^1H^{15}N$-signals of the PPIase domain. Chemical shifts associated with the presence of the N-terminus can be observed for some peaks in the $^1H^{15}N$-HSCQ spectra of the full-length proteins Par14 (Fig. 5A) and Par17 (Fig. 5B). The most obvious chemical shift changes in both full-length proteins could be observed for the peaks of residue Asn^{61}, the first amino acid of the catalytic domain, and Lys^{156}, the last residue of the catalytic domain.

For a more detailed picture, geometric distances from both dimensions between the peaks of the different constructs that were the same, but shifted were calculated, resulting in the combined chemical shift change $\Delta\delta_{HN}$ (Table A5). All combined chemical shift changes between the full-length proteins and the catalytic PPIase domain and between both full-length proteins were plotted against the residue number of Par17 (Fig. 5C). The combined chemical shift changes for the shared residues between Par14 and the PPIase domain and Par17 and the PPIase domain show a similar pattern. In the presence of both N-termini, the strongest chemical shift changes are seen in three sequence regions. The first region is located at the beginning of the catalytic PPIase domain. The region ranges from Asn^{61} to Arg^{66} and includes the strongest chemical shift change of 0.4 ppm for Asn^{61} when comparing the two full-length proteins to the PPIase domain. The second region includes amino acids Met^{110} to Gly^{130}. The highest chemical shift changes in this sequence are observed for Gly^{113} at 0.091/0.082 ppm (Par17/Par14) and Met^{115} at 0.082/0.075 ppm. The last sequence covers amino acids from Val^{152} to Lys^{156} and contains the second largest chemical shift change of 0.160 ppm for Lys^{156}. The second sequence is particularly interesting because some of the amino acids are part of the catalytic center of Par14/17, including Met^{115} [90]. The changes in the chemical environment can be caused either by the simple structural differences between the constructs (position of the N-terminus) and the associated charge changes or by interaction of protein segments with each other. In order to exclude chemical shift changes that are more likely to arise from the presence of the charge of the N-terminus in Par14, a spectrum of a shortened version of Par14, Par14$_{\Delta 1\text{-}22}$, was also recorded. The chemical shift changes compared to the PPIase domain was calculated and were compared to those of Par14 relative to the PPIase domain (Fig A2). The pattern of the chemical shifts were almost identical. Furthermore, no additional chemical shifts were observed between Par14 and the PPIase domain compared to the chemical shift changes of the truncated form (Par14$_{\Delta 1\text{-}22}$) relative to the PPIase domain. This indicates that the relocation of the positive charge of the N-terminus is responsible for the chemical shift changes in the PPIase domain in Par14 and no additional interaction.

In contrast to the results for Par14, additional chemical shift changes between Par17 and Par14 could be observed (Fig. 5D). The chemical shift changes were smaller than thoese between the full-length proteins and the catalytic PPIase domain. However, there were more pronounced chemical shifts changes such as a difference of 0.034 ppm for Lys^{100}, because the residue is near the short helical flexible turn (Ala^{101}-Gln^{103}). Chemical shift changes for Val^{116} (0.017 ppm) and for Phe^{145} (0.011 ppm) could be observed. Additionally, some changes within the sequence of the overlapping N-terminus between Par14 and Par17 could be noted. These changes could be assigned to the amino acids Lys^{29}, Lys^{31}, Gly^{40}, Ser^{44}, Ser^{46}, Lys^{52} and Gly^{58}. It should be considered that these changes in Par17 due to the N-terminal 25 amino acids at the non-structured N-terminus were small. The shifts ranged up to 0.012 ppm except for the amino acid Lys^{52} with a shift of 0.027 ppm and the amino acid Lys^{29} with a shift of 0.072 ppm.

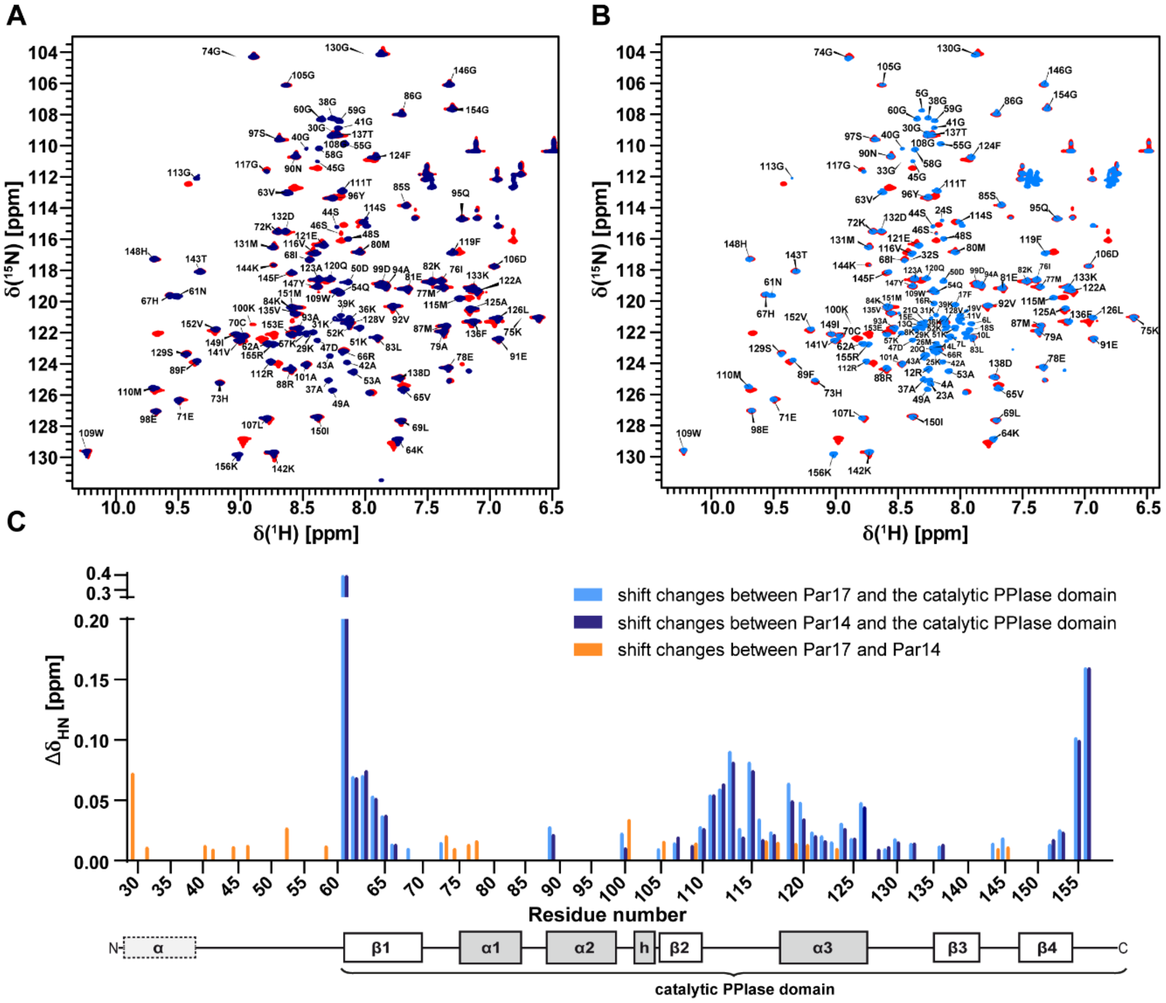

Figure 5: Differences between Par14 and Par17 investigated by the comparison of the ^{1}H^{15}N-HSQC spectra. A: Overlay of ^{1}H-^{15}N-HSQC spectra of Par14 (dark blue) and **B:** hPar17 (light blue) with the catalytic PPIase domain (red). Measurements were carried out at 25 °C in 50 mM KPi buffer and at pH 6.4. Amide resonances of residues were labeled. The residue labeling of Par14 corresponds to that of Par17. **C:** Chemical shift changes calculated for the amide resonances between the proteins were plotted against the residue number of Par17. Shift changes between Par17 (dark blue), Par14 (light blue) and the PPIase domain just as between Par17 and Par14 (orange) are depicted. The secondary structure of the sequence is shown below the graph. α-helices are shown as gray boxes, β-sheets as white boxes, and the small helix turn as “h”.

The residues which show chemical shift changes between Par14 and the isolated catalytic PPIase domain were highlighted on the structure of Par14 (Fig. 6A). The structure of Par14 was calculated by the I-TASSER server [161], taken into account the already known structure of the catalytic PPIase domain (PDB-ID: 3UI6 [91]) of Par14/17. Emphasizing the residues on the surface of the structure showed a shift for all amino acids around the beginning of Par14's N-terminus, including the amino acids with the strongest shift changes Asn^{61} and Lys^{156}. Additionally, the amino acids of the catalytic center surrounding Val^{116} shifted in the presence of the Par14's N-terminus. In general, it is noticeable that the shift changes cluster near the N-terminus of the isolated PPIase domain. This reinforce the suspicion already raised by the truncated variant that the shift changes are caused by the charge of the N-terminus, whose position changes in the different constructs.

Moreover, the chemical shift changes between Par17 and Par14 were highlighted on the structure of Par17 calculated by the I-TASSER server with the already known structure of the catalytic PPIase domain (Fig. 6B). The emphasized residues are affected by the presence of the 25 N-terminal amino acids of Par17. For one, amino acids in the overlapping sequence of the N-terminus of Par14 and Par17 are affected. Furthermore, the 25 N-terminal amino acids had a stronger effect on the chemical environment of the catalytic cleft around Val^{116}. The presence affected the amino acids Phe^{119}, Lys^{144}, Phe^{145} contributing to substrate binding [90]. Also worth mentioning, are the shift changes in the second α-helical loop covering the amino acids His^{73}, Gly^{74}, Ile^{76} and Met^{77}. Those changes were different from those observed between Par14 and the catalytic PPIase domain. This indicates that these shift changes were not only caused by the change of the charge position of the N-terminus, but also by a possible interaction. To investigate a possible interaction in more detail and to narrow down possible interaction segments, cross-linking was used in the further course of this study.

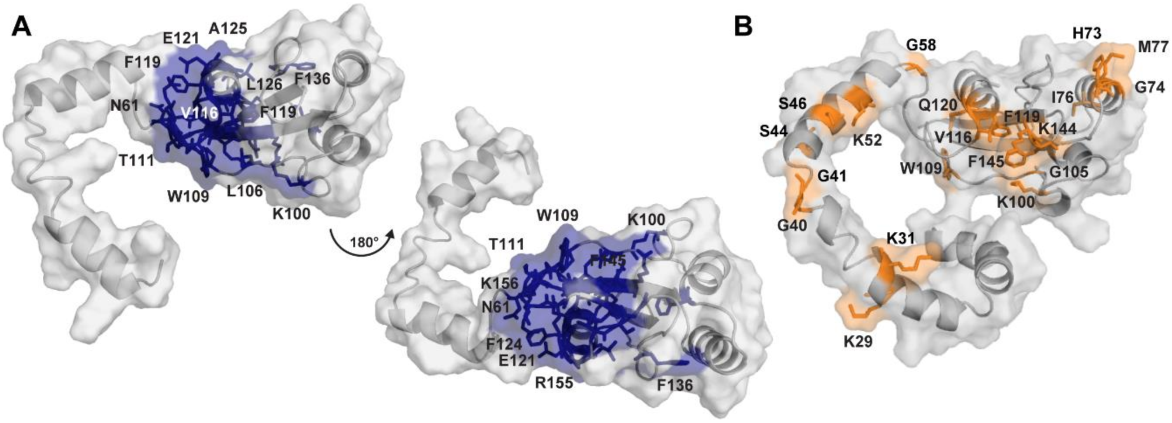

Figure 6: Mapping of the chemical shift changes in the $^1H^{15}N$-HSQC spectra on the structure of Par14 and Par17. A: Mapping of chemical shift changes between Par14 and the PPIase domain (dark blue) from Fig. 6C on the surface of the Par14 (calculated by the I-TASSER server based on the structure of the PPIase domain PDB: 3UI6). **B:** Shifts between Par17 and Par14 (orange) depicted on the surface of Par17 (calculated on the I-TASSER server based on the structure of the PPIase domain PDB: 3UI6)

3.2 Detection of the proximity of the N-terminus to the catalytic PPIase domain by cross-linking

Cross-linker can be used to fix stable and transient contacts between interaction partners. The cross-linker DSSO and photo-reactive amino acids were used to capture intramolecular interactions of Par14 and Par17. For this purpose, Par14 and Par17 were cross-linked with either DSSO or photo-reactive amino acids (Section 2.2.3). Cross-linking with photo-reactive amino acids primarily requires incorporation of photo-reactive amino acids into the proteins. Par14 and Par17 were expressed by *E.coli* in the presence of the photo-reactive amino acids photo-leucine and photo-methionine and the correct folding of the proteins was verified by circular dichroism spectroscopy (Fig. A3). Then the photo amino acid-labeled parvulins were cross-linked by irradiation. For the DSSO cross-linking the unlabeled parvulins were supplemented with the chemical cross-linker DSSO and the reaction was stopped after 1h with TRIS. During cross-linking not only intramolecular but also intermolecular connections emerge. To separate monomeric intramolecular cross-linked forms of the proteins from dimeric or polymeric forms, analytical gel permeation chromatography was performed. The chromatogram of the separation from the DSSO cross-linking showed three peaks for Par17 and Par14 (Fig. 7A). The fractions of the peaks of dimeric (~44kDa) and monomeric (~17kDa) sizes of the protein were collected and samples were loaded onto an SDS-gel (Fig. 7B). The third peak (~1 kDa) appeared at the same volume where DSSO reacts with TRIS. The SDS-gel showed that the monomeric and polymeric cross-linked parvulins were separated successfully. The chromatogram of the separation from cross-linked Par17 and Par14 by photo-reactive amino acids shows one peak for Par14 and Par17 at the size of the monomer form (~17kDa, Fig. 7C). Peaks of polymers could not be observed. The SDS gel of the samples from the fractions of the peaks (Fig. 7D) confirmed that the proteins were monomeric.

The samples from the monomeric parvulins were digested in solution and the cross-links were analyzed by the Analytic Core Facility Essen (ACE) using LC-MS/MS. The ACE Facility analyzed the DSSO cross-links with the program Proteome Discoverer and the search engines SEQUEST and XlinkX (Section 2.2.6). The cross-links caused by photo-reactive amino acids were analyzed with StavroX. All cross-links identified were listed in table A6. The cross-links above a score of 90 for DSSO cross-linking and above a score of 100 for photo-reactive amino acid cross-linking were displayed on the amino acid sequence of the corresponding parvulins. DSSO cross-links could be identified within the catalytic PPIase domain, within the N-terminus and between the catalytic PPIase domain and the N-terminus for both parvulins (Fig. 7E). Similarities of the cross-link pattern between Par14 and Par17 could be observed. In both proteins, connections of the small turn (Lys^{75}/Lys^{100}) of the catalytic PPIase domain with the N-terminus could be identified. The first α-helix (in Par14 Lys ^{50}, in Par17 Lys^{57}/ Lys^{82}) showed a connection to the N-terminus. Furthermore, connections between the flexible extended loop of the catalytic domain, which turns into the third β-sheet (in Par14 Lys^{108}/ in Par17 Lys^{142}, Thr^{143}), and the N-terminus were detected.

Cross-links originating from photo-reactive amino acids could be observed in Par14 and Par17 within the catalytic domain and between the catalytic domain and the N-terminus, but not within the N-terminus (Fig. 7F). Par14 showed an interaction of the loop (Met^{106}) with the N-terminus as observed by cross-linking with DSSO. Furthermore, a connection of the catalytic core (Met^{85}) with the N-terminus emerged. Cross-links with photo-reactive amino acids in Par17 occurred between the first α-helix (Met^{77}, Met^{80}, Glu^{81}) and the N-terminus, as observed by DSSO cross-linking.

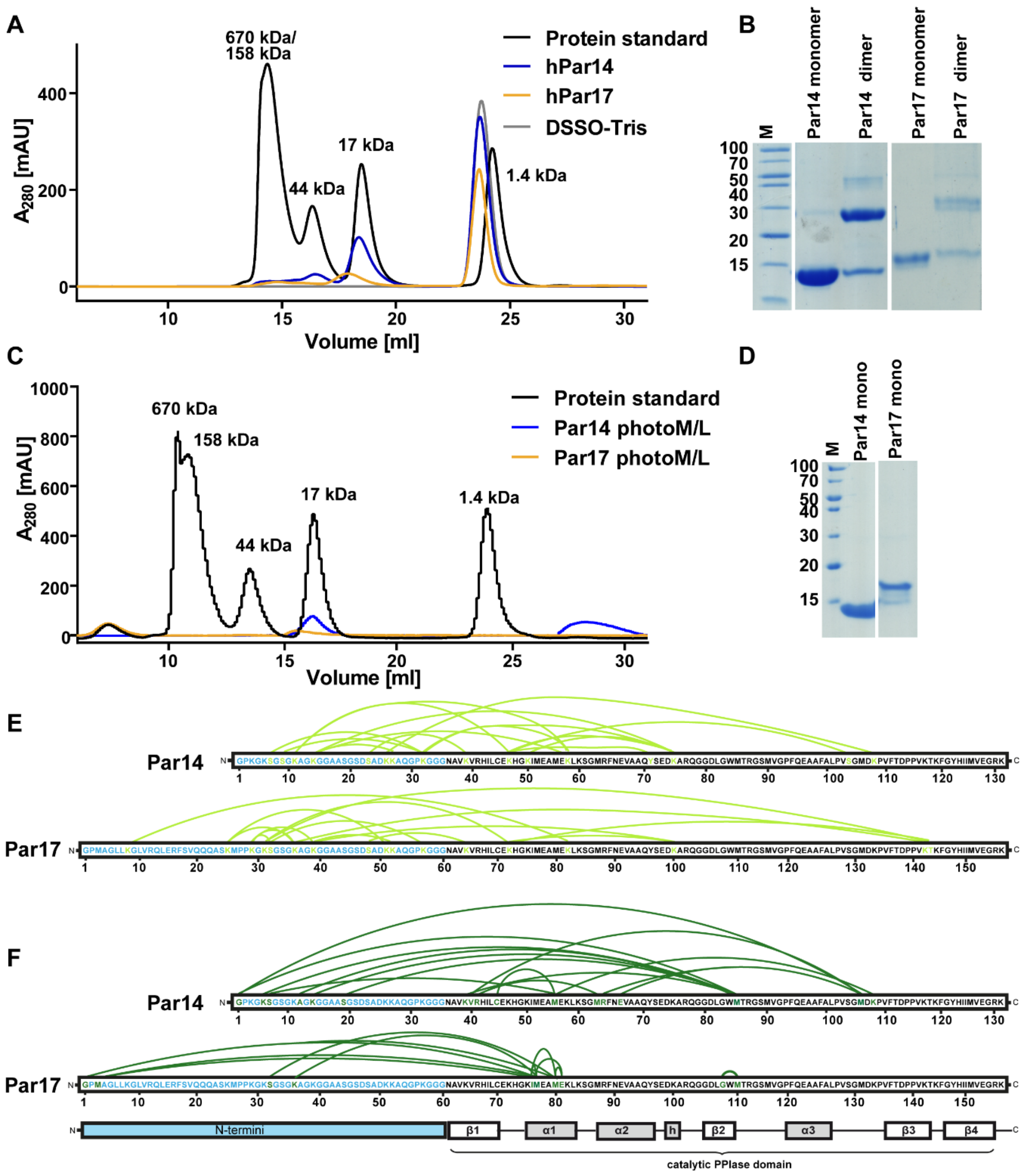

Figure 7: Intramolecular cross-linking of Par14 and Par17. Analytical gel-filtration chromatogram measured at 280 nm of cross-linked Par17 or Par14 by **A:** DSSO or **C:** Photo-reactive amino acids. The peaks of the protein standard (black curve) are labeled with the corresponding protein size. SDS gels of the fractions from the peaks in the gel permeation chromatography of **B:** DSSO cross-linking and **D:** Photo cross-linking experiment. Intramolecular cross-links identified by mass spectrometry by **E:** DSSO cross-linking with score ≥ 90 or **F:** Photo cross-linking with a score ≥ 100. The N-termini of Par14 or Par17 are highlighted in light blue.

The DSSO and photo cross-links between the catalytic domain and the N-terminus of Par14 were highlighted on the structure of Par14 calculated by the I-TASSER server (Fig. 8A). The cross-linked amino acids were connected with dashes and side chains shown were labeled with the residue name of Par17 (for comparison the residues of Par14 were labeled with the corresponding residue name of Par17). With the spacer of DSSO of a length of 10.1 Å the maximum distance of the cross-linked lysine residues is 26 Å measured from the α-carbons atoms [57]. The distances between the DSSO cross-linked residues (yellow) in the Par14 I-TASSER model were determined to be all bigger than 29.3 Å (Table A6, measured from amine of lysine or hydroxymethyl group of the cross-linked residue), which indicates that the N-terminus is closer to the PPIase than demonstrated in the model.

The photo cross-links appear, when the amino acids are close because there is no spacer. The maximum distance between the α-carbons depends on the linked residue and is about 10 Å [77]. However, the distance in the Par14 I-TASSER model of the photo cross-links (dark green dashes) was greater in all cases (Table A6). This supports the DSSO data and the hypothesis that the N-terminus adopts a position in spatial proximity to the catalytic domain. In addition to the cross-links, the chemical shift changes observed in the catalytic domain in the presence of the N-terminus of Par14, shown in Figure 6 were reflected on the structure. If the chemical shifts changes and the cross-links were close to each other or overlapped, the region was assumed to be a possible interactions patch. One interaction patch of Par14's N-terminus near the catalytic cleft could be revealed for Par14. The interaction patch (indicated in red) includes the cross-links Met^{110}, Lys^{100}, Lys^{64} and Met^{131} and the surrounding chemical shift changes.

In the calculated I-TASSER structure of Par17, the DSSO and photo cross-links are also shown with dashes, and in addition, the residues with chemical shift changes between Par14 and Par17 are highlighted (Fig. 8B). For the DSSO cross-links, one measured distance in the model met the distance acceptance assumed by the cross-link size. The distance between the residues Thr^{147} and Lys^{31} is 25 Å. However, for the other DSSO cross-links, the distance is larger than the cross-link length (Table A6), indicating that the N-terminus may actually be closer to the catalytic domain. Similar observations could be made for the photo cross-links. For these cross-links all measured distances were larger than 27.9 Å in the I-TASSER model of Par17 between the cross-linked residues. In case of the Par17 I-TASSER model, the interacting areas indicated by cross-linking are complemented by the observed chemical shift changes between Par14 and Par17 to two interacting regions. One interacting region is upstream of the catalytic cleft and includes the amino acids Lys^{100}, Lys^{144} and Thr^{143}. This region appeared to interact with the middle portion of the N-terminus of Par17 (Lys^{31} to Lys^{39}). This interaction region is also found in the N-terminus of Par14. However, in Par14, the interaction site with Met^{110} and Lys^{100} is slightly below the region found for Par17. The second N-terminal interaction region found for Par17 is located in the first α-helix of the PPIase domain (Lys^{72} to Lys^{82}). The α-helix is connected to the beginning of the N-terminus of Par17 by the amino acids Met^{1}, Met^{3}, and Lys^{8}.

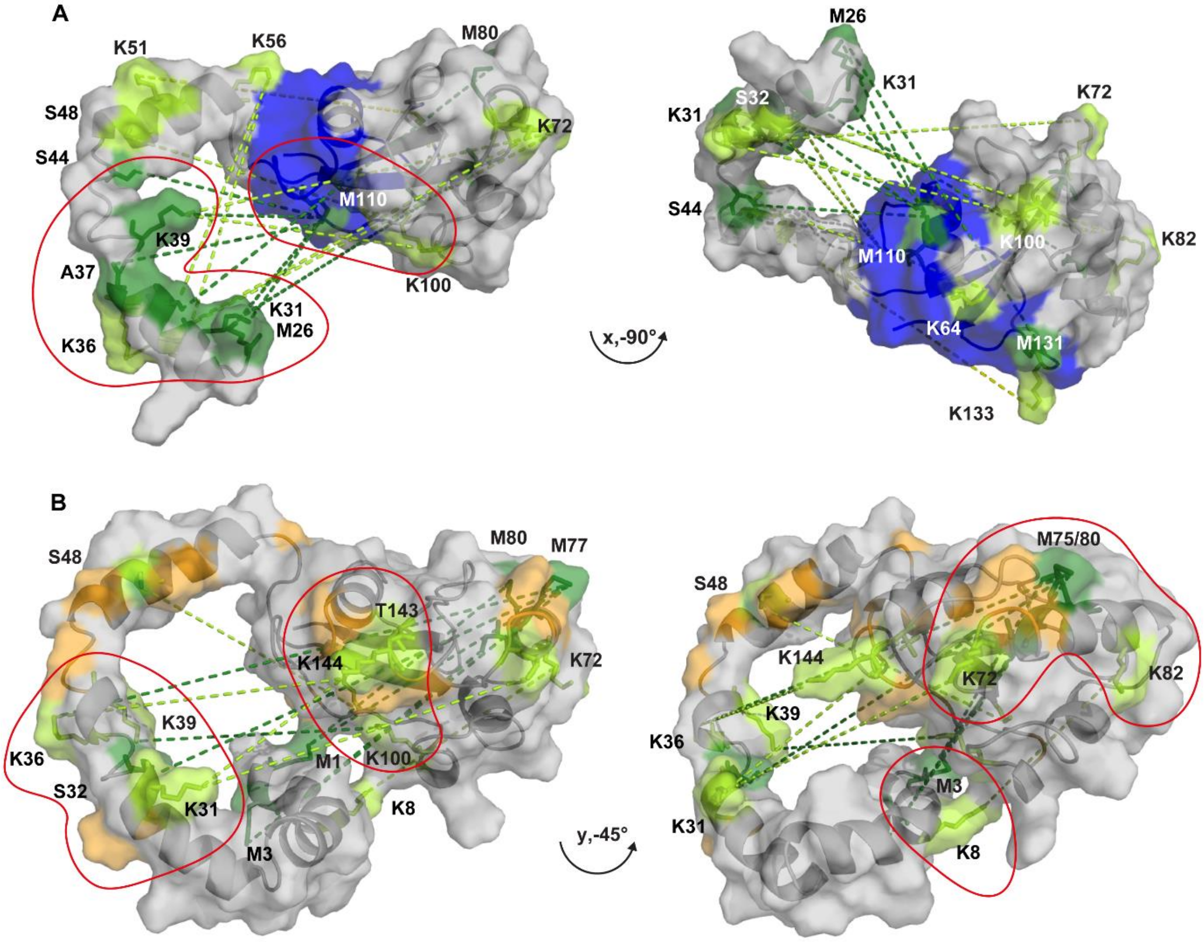

Figure 8: Cross-links of N-terminus and catalytic PPIase domain of Par14 and Par17. Cross-links between the catalytic domain and the N-terminus by DSSO (lime yellow) and by photo amino acids (dark green) are labeled and connected. Chemical shift differences from figure 6 between Par14 and the catalytic PPIase domain (blue) and between Par17 and Par14 (orange) are displayed as well. Shifting amino acids and cross-links depicted on **A:** The structure of Par14 calculated by the I-TASSER server based on the solved structure of the catalytic domain (modified PDB: 3UI6) and **B:** The Par17 structure calculated by I-TASSER server.

3.3 Catalytic function of Par17 in comparison to Par14 and the isolated catalytic PPIase domain

As mentioned, the catalytic activity and substrate selectivity of Par17 has rarely been investigated. One attempt was made in which the activity of GST-Par17 for model substrates was measured in comparison to a catalytically less active GST-Par17$_{D99A}$ mutant [142]. There is also limited data available on the shorter isoform Par14. Therefore, in this work the catalytic activities of both parvulins and the isolated catalytic PPIase domain were examined, and it was investigated whether the different lengths of their N-termini influenced the activity or substrate specificity.

3.3.1 Examination of the effect of the extended N-terminus on substrate specificity

To determine the efficiency and substrate specificity of Par17, the commonly used protease-coupled assay first described by Fisher et al. [30] were used. As described in the introduction, in the assay, the *trans* form of the model substrate is cleaved by chymotrypsin and the change in the absorption at 390 nm resulting from free pNa, is measured (Section 2.2.7). The assay consists of two reactions. When the model substrate is added, all *trans* isomers present in the solution are immediately cleaved by chymotrypsin. The extent of the first burst correlates with the proportion of *trans* isomers of the model substrate in solution at the start of the measurement. With the addition of the model substrate, the remaining *cis*-shaped model substrates slowly begin to isomerize by thermal or catalytic reactions. The newly formed *trans* model substrates are immediately cleaved and isomerization and can thus be measured over time. The catalytic activity of the isomerase can be assessed by calculating the rate constant from the observed isomerization in the presence of the enzyme followed by the subtraction of the rate constant of the thermal isomerization.

In the assay, the velocity of the reaction need to be proportional to the amount of added enzyme to exclude errors in rate measurements. Limitations during measurements could be the possible inhibition of the newly formed product or the decrease of the substrate concentration below the saturation levels needed to keep the enzyme-substrate complex in the steady state. To verify the linearity of the velocity of Par17 in relation to the used enzyme concentration the rate constant $k_{observed}$ –

$k_{thermal}$ was determined for the substrate peptide Suc-Ala-Ser-Pro-Phe-pNa at different enzyme concentrations.

Depending on the substrate peptide, there is a high or low percentage of *trans* isomers in the initial solution. When the concentration of the *trans*-isomer is high, the initial increase caused by the fast cleavage of pNa from these *trans* peptides will give a higher absorbance signal. As a result, there is less substrate remaining to measure the *cis*/*trans* isomerization reaction compared to a substrate peptide with a lower initial percentage of *trans* isomers. The substrate peptide with serine at the Xaa-Pro position is one of the peptides with the lowest initial *cis* population (table A4, [54]), correlating to the lowest substrate concentration. To ensure that at one of the lowest substrate concentrations, the substrate concentration is still above the saturation values, the substrate Suc-Ala-Ser-Pro-Phe-pNa was chosen as the candidate.

The absorption at 390 nm was measured over time after addition of the peptide (total concentration 75 µM) in the absence or presence of different concentrations of Par17 in three replicates each. The average baseline measurement (average of the first 200 data point) was subtracted from each data point measured after the addition of the substrate peptide (Fig. 9A, table A7). Measurements were performed in PBS buffer with a pH of 6.8, and at 10 °C to reduce thermic isomerization. For the model substrate Suc-Ala-Ser-Pro-Phe-pNa an initial *trans* population of around 85% and only around 15% *cis* isomers was revealed. With increasing Par17 concentrations, the slopes of the curves were steeper than the slope of the thermic reaction.

Nevertheless, the difference between the lower Par17 concentrations and the thermic reactions seemed to be small. The obtained data can be fitted with nonlinear regression to Eq. 2 (Section 2.2.7) under a pseudo first order assumption. This is the case if the $k_{observed}$ values behave linear under rising PPIase concentrations, which has to be verified and adjusted for a given set of substrates and enzyme concentration. Linearity between the observed rate constant $k_{observed} - k_{thermal}$ and the PPIase concentration is only given under the assumption that the PPIase concentration is low with regard to the initial concentration of the *cis* isomer of the substrate. To verify that $k_{observed}$ rises linear with the used concentration of Par17 rate constants from the progression curves were obtained by fitting. Since the observed reaction is composed additively of the thermal and the catalyzed reaction, the rate constant for the thermic reaction was subtracted from the observed rate constant. The results were plotted against the used Par17 concentration (Fig. 9B, table A7). The differences between the rate constants for Par17 with a concentration of 1 µM and the thermic rate constants were too small considering the acceptable standard deviations, so these values were excluded from the graph. Despite the high standard deviation, a linear slope was observed for the measured Par17 concentrations. The proportional growth of the velocity of the reaction to the amount of added Par14 and the isolated PPIase domain was already confirmed for the peptides in which Ser, His or Arg were preceding proline [54]. This implies that the tested parvulin concentrations were viable for the protease-coupled isomerase assay.

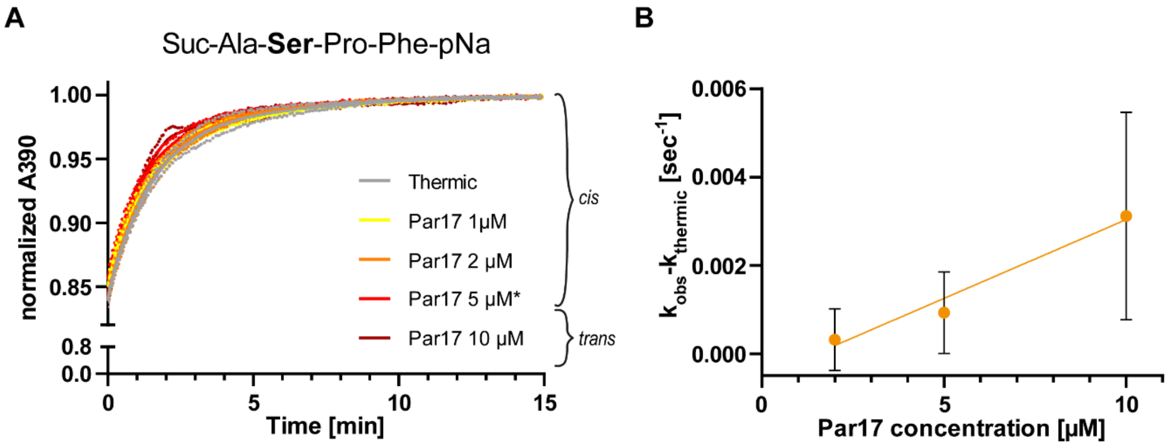

Figure 9: Linearity of the rate constant of the catalyzed reaction with the amount of added Par17. A: The mean change in absorbance at 390 nm after the addition of the model substrate Suc-Ala-Ser-Pro-Phe-pNa in the presence and absence of different concentrations of Par17 are depicted. Three replicates each were measured (asterisk marked: only two replicates). Dots represent the standard deviation of the corresponding mean. On the right side of the graph, the portions of *cis* and *trans* isomers at the beginning of the measurement are displayed. **B:** The calculated rate constant from measurements with different enzyme concentrations of Par17 for the substrate Suc-Ala-Ser-Pro-Phe-pNa are plotted against the concentration. A linear fit for the data points is shown.

In order to determine the first order rate constant from the progression curve by subtracting the thermic rate constant from the observed isomerized rate constant, the substrate concentration has to be less than the K_M of the PPIases (1990 Stein). The appropriate concentration required to remain below the K_M value has been determined for other PPIases [2, 63], but not for the investigated parvulin isoforms. Since other PPIases are much more active [52] this could be a restricting factor for the determination of the activity of the parvulin isoforms Par14 and Par17 in the assay.

As a representative substrate for the K_M determination Par14 was chosen. For the determination of the K_M value, the isomerization was measured for different concentrations of the substrate peptide Suc-Ala-Gln-Pro-Phe-pNa. The isomerization was monitored by measuring the absorption of free pNa at 390 nm. To calculate the initial velocity, the slope of the first data points (correspond to the initial velocity) of the catalyzed reaction was calculated, followed by the subtraction of the slope of the first data points of the thermal isomerization for the corresponding peptide concentrations. Then the absorption was converted into the quantity of the converted molecules. For this purpose, the slope was calculated from the absorption as a function of the pNa concentration (performed by Alma Rute, Fig. A4). The slope of the absorption per time was then divided by the slope of the absorption per pNa resulting in the initial velocity (Table A8).

The initial velocities of Par14 at different substrate concentrations were plotted against the substrate concentrations and the curve was fitted with a nonlinear regression according to Michaelis-Menten enzyme kinetics (Fig. 10A, table A8). The K_M value calculated by the program was 120.5 µM and the v_{max} was 34.76 µM/min. Since Par14 has only one active site, the applied enzyme concentration of 2 µM could be matched with the concentration of catalytic sites and the turnover number k_{cat} could be calculated (0.2896 s^{-1}). From these values, the catalytic efficiency k_{cat}/K_M could be calculated ($2.403 \cdot 10^3$ $M^{-1}s^{-1}$). The double-reciprocal plot 1/velocity against 1/substrate concentration, usually called Lineweaver-Burk plot, was generated (Fig. 10B). The x-intercept was -0.007963 and the y-intercept was 0.02909. The reciprocal values resulted in a K_M value of 125.5 µM and a v_{max} value of 34.37 µM/min, and confirmed the values calculated in the fit. For the isolated PPIase domain and Par17, it was demonstrated by Jennifer Borger under my supervision that the K_M values of both were in the same range [8].

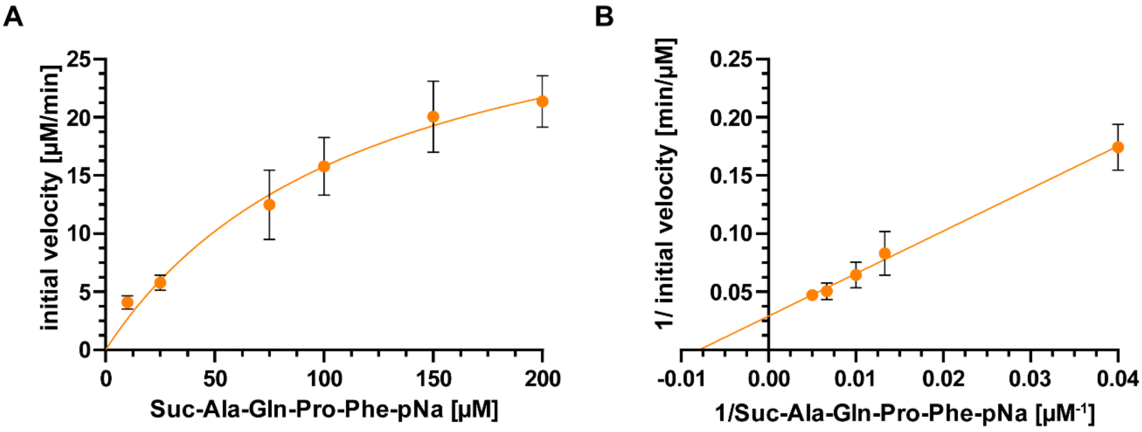

Figure 10: K_M determination of Par14. A: The initial velocity is plotted against the substrate concentration of Suc-Ala-Gln-Pro-Phe-pNa. The measurement was carried out in PBS pH 6.8 at 10°C and with a total concentration of 2 µM Par14. The bars represent the standard deviation from three measurements each. **B:** The Lineweaver–Burk plot displays the reciprocal velocity in relation to the reciprocal substrate concentration. The line shows a linear fit with the x-intercept.

Subsequently 18 different substrate peptides (Suc-Ala-**Xaa**-Pro-Phe-*p*Na) with varying amino acids at the Xaa position were measured to determine the isomerase activity and substrate selectivity. As before, the absorbance of the free pNa after cleaving by chymotrypsin was measured at 390 nm in PBS buffer with a pH of 6.8. The total enzyme concentration was 2 µM (Table A6). The substrate concentration of 75 µM was chosen, because it has already been proven in adequate concentration in other measurements [63, 127]. Each substrate peptide was measured at least three times for each set of conditions.

The graphs of the substrate peptides with serine, glycine, isoleucine, glutamic acid and lysine preceding proline were shown in this work as representative examples of different amino acid side chain groups. Gly was featured as an example of a polar, uncharged amino acid with a single hydrogen as its side chain (Fig. 11A). As with the substrate peptide with Ser preceding the Pro position, Gly had a small portion of about 22% *cis*-isomer at the beginning of the measurement (*cis/trans* ratios of all substrate peptides are listed in table A4). The slopes of the curve of the Gly peptide isomerized by the isolated PPIase domain and Par14 seem to be similar and steeper than the one from the thermic reaction. The conversion caused by Par17 lies between that of the Par14/isolated PPIase domain and the thermic reaction. Isomerase activity of all parvulin forms could be observed for the substrate peptide Suc-Ala-Gly-Pro-Phe-pNa.

Phenylalanine represented the nonpolar, strongly hydrophobic amino acids. Amino acids with an aromatic side chain tend to have a high proportion of *cis*-population in the LiCl/TFE buffer (table A4, [54]). For Phe preceding proline, the *cis*-isomers in the beginning made up about 50% of isomers in the solution, meaning that changes could be visualized clearly (Fig. 11B). The slope of the curve of Par17 is slightly steeper than the one of the thermic reaction. Par14 and the isolated PPIase domain catalyzed the reaction at a similar rate, and faster than Par17. Thus, all PPIases measured showed an enzymatic activity for Suc-Ala-Phe-Pro-Phe-pNa, although to varying extents.

Glu was shown as an example of a polar, negatively charged amino acid (Fig. 11C). When Glu is placed at the Xaa-Pro position the *cis*-isomer proportion at the beginning of the reaction was around 50%. The reaction with Par17 did not notably differ from the thermic one. In presence of the isolated PPIase domain or Par14 the curve was steeper than the thermic reaction. For the isolated PPIase domain a large standard deviation was observed so it is not certain, weather the PPIase is less active than Par14 or not. However, while Par14 and the isolated PPIase domain isomerized the substrate peptide Suc-Ala-Glu-Pro-Phe-pNa, Par17 did not.

Lys was displayed as an example of a positively charged, polar amino acid (Fig. 11D). Lys has a side chain residue containing a terminal amino group. For Lys preceding proline the *cis*-isomer proportion was approximately 50%. The curves for Par14, Par17 and the catalytic PPIase domain were similar, and all were sharper than the curve of the thermic reaction. Therefore, all measured parvulin forms catalyzed the peptide Suc-Ala-Lys-Pro-Phe-pNa in a similar manner.

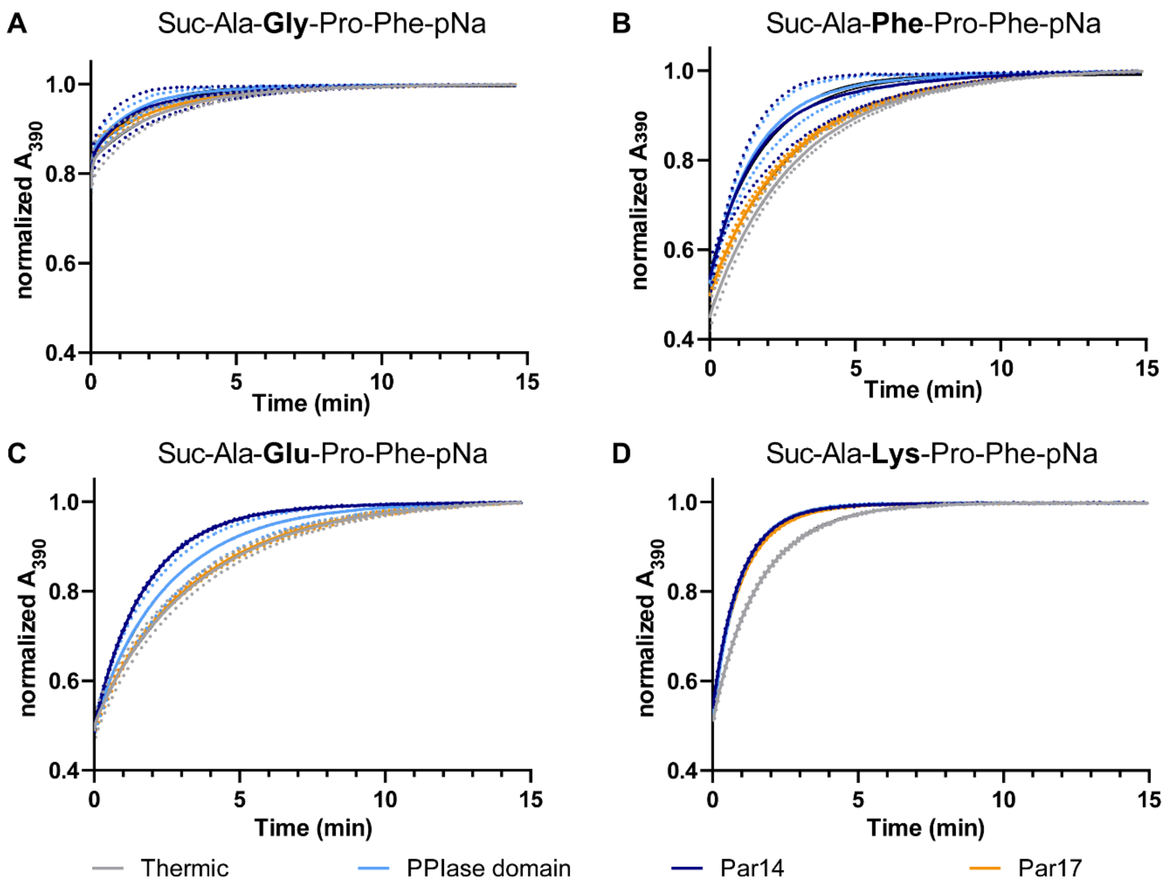

Figure 11: Thermic and catalyzed reactions of protease-coupled isomerase assay for representative substrate peptides measured with Par17, Par14 and the catalytic PPIase domain. The mean changes in absorbance over time for model substrate **A:** Suc-Ala-Gly-Pro-Phe-pNa, **B:** Suc-Ala-Ile-Pro-Phe-pNa, **C:** Suc-Ala-Glu-Pro-Phe-pNa and **D:** Suc-Ala-Lys-Pro-Phe-pNa within the protease-coupled isomerase assay with different enzymes are depicted. The dots represent the standard deviation of at least three measured replicates (for the exact number of measurements see table A9).

Additional graphs for the remaining amino acids preceding proline are presented in the appendix (Fig. A5). Although the graphs could provide an initial assessment of enzyme activity through the incline of the curves and could also reveal differences between the different substrate peptides and the parvulin isoforms, it was easier and more accurate to judge the selectivity according to the respective calculable rate constants. The rate constants from the observed progression curves were obtained by fitting with nonlinear regression (exponential, one phase association), followed by the subtraction of the rate constant of the thermic reaction. Knowing that the number of active centers corresponds to the enzyme concentrations for the parvulin isoforms, the k_{cat}/K_M could be calculated from the rate constants (Eq. 2). All calculated values for the different substrate peptides and parvulin isoforms are presented with the number of repeat measurements that were performed (Table A9). The catalytic efficiency of the parvulin isoforms and the catalytic domain varied within a range of 10^2 to 10^3 $M^{-1}s^{-1}$. If the activity was below 10^2 $M^{-1}s^{-1}$, it could no longer be clearly determined with the assay, since the difference from the thermal reaction with the higher standard deviations was too small. Moreover, the catalytic efficiency under a value of 10^2 $M^{-1}s^{-1}$ is low. The highest activity could be observed for Par14 with Ala preceding proline with an efficiency of $6.4 \cdot 10^3$ $M^{-1}s^{-1}$ and for the isolated PPIase domain with Arg at the Xaa position with an efficiency of $5.7 \cdot 10^3$ $M^{-1}s^{-1}$. In this order of magnitude, the catalytic efficiency is still moderate.

However, some differences in the catalytic efficiency could be observed for the different substrate peptides (Suc-Ala-Xaa-Pro-Phe-pNa) with varying amino acids at the Xaa position. For visualization of the differences, the $k_{cat/}K_M$ values were plotted in a bar graph and arranged according to the activity of Par17, starting from the highest catalytic efficiency (Fig. 12). Par17 only had an efficiency above 10^2 $M^{-1}s^{-1}$ for five substrate peptides. When the efficiency of Par17 for the substrates was the same, the peptides were ranked according to the efficiency of the PPIase. It offers a good comparison value, since Par14 and Par17 contain this domain.

For five substrate peptides, Par17 showed an efficiency higher than 10^2 $M^{-1}s^{-1}$. In descending order, the peptides with Arg, Lys, Leu, Gln and His preceding proline ranged from $3.9 \cdot 10^3$ $M^{-1}s^{-1}$ to $0.3 \cdot * 10^3$ $M^{-1}s^{-1}$. Two of these five amino acids at the Xaa position in the model substrates have a positive charge at a physiological pH (Arg, Lys). The activity of the positively charged amino acids preceding proline had an efficiency approximately 10 times higher than the peptides with Leu, Gln and His preceding proline. The k_{cat}/K_M values were $3.9 \cdot 10^3$ $M^{-1}s^{-1}$(Arg) and $2.7 \cdot 10^3$ $M^{-1}s^{-1}$ (Lys). Furthermore, both substrate peptides had an efficiency about 30 times higher than the other measured substrate peptides. In addition, the substrate peptides with the positively charged amino acids in the Xaa position were the only ones for which Par17 showed a similar efficiency to Par14 and the isolated PPIase domain. For the other substrate peptides except for Asp, Par14 and PPIase always showed a higher efficiency than Par17.

Table14: Mean rate constant k, the standard deviation and the k_{cat}/K_M value of the target proteins calculated from the data of protease-coupled isomerase assay. The assay was performed with different model substrate peptides. Xaa stands for the varying amino acid in the model substrate preceding the proline (Suc-Ala-Xaa-Pro-Phe-pNa).

Xaa	**$k = k_{observed} - k_{thermal}$ [min^{-1}] and standard deviation with number of measurements**						**k_{cat}/K_M [$M^{-1}\cdot s^{-1}$]**		
	Par17	**n**	**Par14**	**n**	**PPIase domain**		**Par17**	**Par14**	**PPIase domain**
Ala	0.017 ± 0.043	10*	0.770 ± 0.608	9*	0.508 ± 0.262	9*	0.1*10^3	6.4*10^3	4.2*10^3
Arg**	0.470 ± 0.037	3	0.582 ± 0.094	3	0.683 ± 0.064	3	3.9*10^3	4.9*10^3	5.7*10^3
Asn	<0.01 ± 0.157	6*	0.192 ± 0.322	8*	0.173 ± 0.303	6*	<0.1*10^3	1.6*10^3	1.4*10^3
Asp	0.013 ± 0.013	6	0.028 ±0.063	6	0.015 ± 0.032	6	0.1*10^3	0.2*10^3	0.1*10^3
Gln	0.040 ± 0.022	6*	0.537 ± 0.424	11*	0.618 ± 0.367	9*	0.3*10^3	4.4*10^3	5.2*10^3
Glu	<0.01 ± 0.029	6*	0.267 ± 0.011	3*	0.114 ± 0.074	8*	<0.1*10^3	2.2*10^3	1.0*10^3
Gly	<0.01 ± 0.029	5*	0.390 ± 0.457	6*	0.275 ± 0.214	5*	0.3*10^3	3.3*10^3	2.3*10^3
His**	0.036 ± 0.006	3	0.067 ± 0.009	3	0.068 ± 0.029	3	0.3*10^3	0.6*10^3	0.6*10^3
Ile	0.013 ± 0.013	6	0.146 ± 0.270	5	0.147 ± 0.019	6	0.1*10^3	1.2*10^3	1.2*10^3
Leu	0.063 ± 0.021	7*	0.304 ± 0.291	10*	0.223 ± 0.178	10*	0.5*10^3	2.5*10^3	1.9*10^3
Lys**	0.33 ± 0.012	3	0.412 ± 0.014	3	0.442 ± 0.006	3	2.7*10^3	3.4*10^3	3.7*10^3
Phe	0.01 ± 0.005	4*	0.268 ± 0.284	6*	0.298 ± 0.197	6*	0.1*10^3	2.2*10^3	2.5*10^3
pSer**	<0.01 ± 0.001	3	-	-	-	-	<0.1*10^3	-	-
Ser	<0.01 ± 0.098	6*	0.332 ± 0.054	3	0.327 ± 0.273	6*	<0.1*10^3	2.7*10^3	2.7*10^3
Thr	<0.01 ± 0.048	3	0.229 ± 0.334	5	0.141 ± 0.218	5	<0.1*10^3	1.9 *10^3	1.2*10^3
Trp	0.012 ± 0.001	3	0.148 ± 0.007	6	0.063 ± 0.034	6	0.1*10^3	1.2*10^3	0.5*10^3
Tyr	0.012 ± 0.005	4	0.371 ± 0.176	6	0.198 ± 0.148	6	0.1*10^3	3.1*10^3	1.7*10^3
Val	0.011 ± 0.005	6*	0.408 ± 0.432	6	0.289+ 0.166	5	0.1*10^3	3.4*10^3	2.4*10^3

* Some measurements were performed by Jennifer Lynne Borger under my supervision [8]
** All measurements were performed by Jennifer Lynne Borger under my supervision [8]

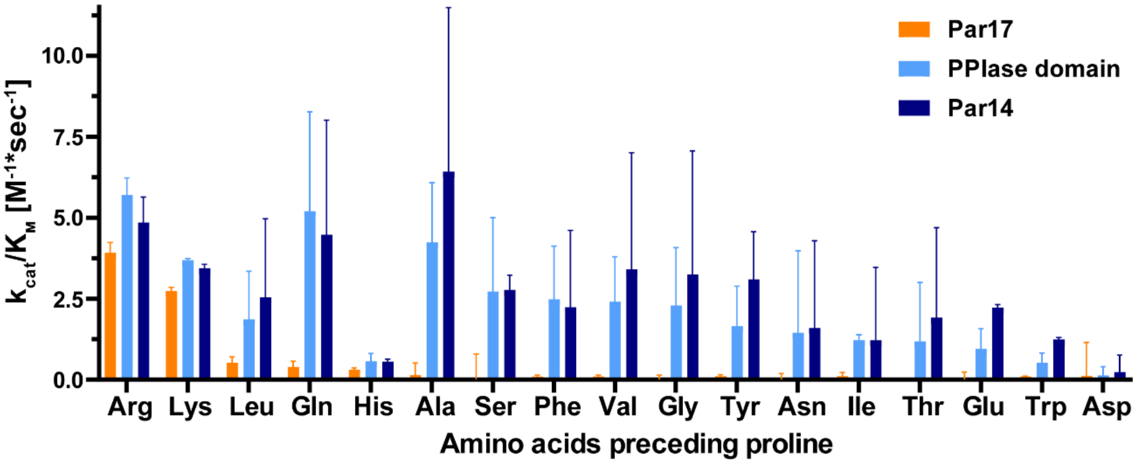

Figure 12: Substrate specificity of the parvulins. Catalytic efficiency of Par17 (orange), of the isolated catalytic PPIase domain (light blue) and of Par14 (dark blue) with various substrate peptides. The order is set by decreasing Par17 activity up to an activity of 0.1 and then arranged by the decreasing activity of the isolated catalytic PPIase domain.

In addition to the positive charged amino acids, Par17 had an efficiency 3-5 times higher than for the other model substrate peptides for the amino acids Leu and Gln at the Xaa position with an efficiency of $0.3 \cdot 10^3$ $M^{-1}s^{-1}$ and $0.5 \cdot 10^3$ $M^{-1}s^{-1}$, respectively. Leucine has a non-polar aliphatic side chain and glutamine a polar one, but both have no charge. Leucine's side chain is made up of an isobutyl group. Interestingly, for the constitutional isomer isoleucine Par17 was 3 times less efficient. One other branched-chain amino acid is valine, which lacks one methylene in comparison to leucine. Par17 was also 3 times less efficient for the substrate peptide with Val. Furthermore, glutamine is an uncharged derivate of glutamate. The hydroxyl unit of the carboxyl group is replaced by an amine. Remarkably, Par17 was 5 times more efficient for the Gln-Pro peptide than for the Asn-Pro peptide. The only difference between the two amino acids is that the side chain of glutamine has one more methylene group than asparagine.

Par14 and the isolated catalytic PPIase domain were similarly active for the measured substrate peptides. Considering the standard deviation, no real differences could be determined. Moreover, the substrate selectivity of Par14 and the catalytic PPIase domain was not as definite as for Par17.

Nevertheless, the highest efficiency could also be observed for the two positively charged amino acids Leu and Arg preceding proline in the substrate peptides and additionally for Gln and Ala. The mean efficiency ranged from $6.4 \cdot 10^3$ $M^{-1}s^{-1}$ (Arg, Par14) to $3.4 \cdot 10^3$ $M^{-1}s^{-1}$ (Lys, Par14). For most of the other substrate peptides, Par14 and the isolated catalytic domain showed a moderate efficiency. The kinetic efficiency for the peptides with the amino acids Val, Gly, Tyr, Ser, Leu, Phe and Glu ranged between $3.0 \cdot 10^3$ $M^{-1}s^{-1}$ (Val) to $2.2 \cdot 10^3$ $M^{-1}s^{-1}$ (Glu) for Par14. For the substrate peptides where Thr, Asn, Trp or Ile were at the Xaa position, Par14 and the PPIase domain seemed to be slightly less efficient by a factor of about 3-6 times, ranging from $1.9 * 10^3$ $M^{-1}s^{-1}$ (Thr) to $1.21 * 10^3$ $M^{-1}s^{-1}$ (Ile). Par14 and the catalytic PPIase domain had the lowest efficiency for the substrate peptides with His and Asp at the Xaa position with the respective values $0.5 \cdot 10^3$ $M^{-1}s^{-1}$ and $0.2 \cdot 10^3$ $M^{-1}s^{-1}$ for Par14. Therefore, Par14 was still more efficient for the His-Pro peptide than Par17 was for most of the substrate peptides.

Interestingly, Par14 and the catalytic PPIase domain tend to be less efficient for negatively charged amino acids in the Xaa position. For Glu preceding proline an efficiency of $2.2 \cdot 10^3$ $M^{-1}s^{-1}$ for Par14 was determined. For Asp the efficiency was around 10 times less. In addition, it was the worst efficiency measured for both Par14 and the PPIase domain. The only difference between the two negatively charged amino acids is the length of the residues. Asp is the shorter amino acid and lacks one methylene group. The abating effect due to the length could also be observed for the amide forms of the negatively charged amino acids. Par14 was approximately 3 times less efficient for the shorter amino acid residue Asn preceding proline than for the longer residue Gln with one additional methylene group. As already mentioned, this effect in the amide forms was also observed for Par17.

In conclusion, Par17 was more selective for the amino acid preceding proline than the shorter Par14 isoform and the isolated catalytic PPIase domain. Par17 was most efficient for the positively charged residues Arg and Lys preceding proline in the substrate peptide. For other substrate peptides, Par17 was less efficient. The efficiency pattern of Par14 and the catalytic PPIase domain were similar. They showed the tendency to be slightly more efficient for positively charged amino acids. The lowest activity was determined with negatively charged amino acids, but they were still more efficient than Par17 for most of the substrate peptides. With the negatively charged amino acids and their amide forms at the Xaa position, it is notable that the efficiency decreases if the amino acid residue is shortened.

3.3.2 Exploring the effects of the N-terminus on substrate specificity by NMR

Concerning the stronger substrate sepecificity of Par17 compared to the shorter isoform and the catalytic domain for positive amino acids preceding proline, it was investigated whether there are differences between Par17 and the isolated PPIase domain in the binding of the substrate peptides. Due to the single residue resolution, NMR spectroscopy was used again to identify residues of Par17 and the isolated PPIase domain involved in binding (Section 2.2.8). Representative substrate peptides were titrated to ^{15}N-labeled Par17 and the ^{15}N-labeled isolated PPIase domain. BEST-TROSY-HSQC spectra of the parvulins were recorded in the absence or presence of various peptide concentrations of the model substrates with Lys and Glu preceding proline at 20 °C in 50 mM KPi buffer (pH 6.7). The peaks were assigned and combined chemical shift changes between the bound and free signals were calculated. The shift differences in Par17 and the isolated catalytic PPIase domain in the presence of the substrate peptides were plotted against the residue number of Par17 (Fig. 13, table A10). One representative measured substrate peptide was the positively charged Suc-Ala-Lys-Pro-Phe-pNa. For this substrate peptide, an isomerization activity of Par17 could be determined and it was catalyzed by all measured parvulin isoforms with around the same efficiency. The observed chemical shift changes upon addition of the substrate to Par17 and to the catalytic PPIase domain were similar (Fig. 13A). The most continuous shift changes due to the presence of the peptide could be observed for the residues ranging from Arg^{112} to Phe^{124}, with the highest values of 0.186/0.208 ppm (Par17/PPIase domain) for Val^{116} and 0.061/0.059 ppm (Par17/PPIase domain) for Gly^{113}. Val^{116} was indicated to make up the hydrophobic active side together with the amino acids Leu^{69}, Leu^{107}, Met^{110}, Met^{115}, Phe^{119} and Phe^{145}. Leu^{107} and Phe^{119} also showed shift changes upon addition of the substrate peptide. The neighboring amino acids of Leu^{107}, the residues Asp^{106} and Gly^{105} also showed shift changes. The residues that showed chemical shift changes were highlighted on the structure of Par17 calculated by I-TASSER. Overlapping chemical shift changes between Par17 and the PPIase domain were displayed in yellow, shifts found only at Par17 in orange, and shifts found only at the catalytic domain in blue (Fig. 13B). The most striking differences that could be observed between Par17 and the isolated PPIase domain were the shifting signals of amino acids Asn^{61}, Arg^{66}, His^{67} and Ile^{68} in the isolated PPIase domain. These changes were not observed in Par17. Normally, the N-terminus is attached to these amino acids in the isolated PPIase domain. Another interesting observation was that only in Par17, the amino acid Asp^{99} shifted slightly. The other representative substrate peptide measured was the negatively charged Suc-Ala-Glu-Pro-Phe-pNa (Fig. 13A). For this substrate peptide, no activity could be measured with Par17, whereas the shorter isoform Par14 and the isolated catalytic PPIase domain showed a moderate efficiency. Within the overlapping residues of Par17 and the PPIase domain, the measured chemical shifts changes were similar. However, there were more shift changes observed with the negatively charged substrate peptide compared to the positive one throughout the catalytic PPIase domain. Four regions stand out in particular: the region with the greatest shifts between the residues Arg^{111} to Phe^{124}, the region at the N-terminus of the PPIase domain, the region at the C-terminus and additionally the third α-helix with the transition to the loop ranging from Met^{87} to Arg^{101}. The greatest shift changes were 0.272/0.2805 ppm (Par17/PPIase domain) for Val^{116}, 0.179/0.169 ppm (Par17/PPIase domain) for Gly^{113} and 0.182/0.169 ppm (Par17/PPIase domain) for Phe^{119}. Thus, the chemical shifts in this area were greater than those observed in experiments with the positive substrate peptide at the same concentration. On closer examination, the application of chemical shifts at different substrate peptide concentrations and the fitting of a K_D value indicated that the binding of the negative substrate peptides is slightly stronger (Fig. A6). Yet, the most striking difference to the positive substrate peptide is the fact that chemical shifts in the N-terminus of Par17 were observed in the first 25 amino acids. The shifts in the N-terminus occurred discontinuously between residues Ala^4 and Met^{26}. These are the amino acids found exclusively in Par17, except for Met^{26}. The strongest shifts in the N-terminus were observed with a moderate change of 0.026 ppm for Arg^{12}, 0.018 ppm for Glu^{15} and 0.018 ppm for Gln^{21}. The chemical shift changes for the negatively charged substrate peptide were depicted on the structure of Par17. Overlapping shift changes were highlighted in yellow, shifts that occur only in the PPIase domain in blue and shifts that occur only in Par17 in orange (Fig 13C). It is striking that again only in the N-terminus of the isolated PPIase domain the signals of the amino acids His^{67} and Ile^{68} shifted. Another interesting observation was that with both substrate peptides, the amino acid Lys^{133} on the back of the protein changed with a small extent of 0.01 ppm only in Par17.

To investigate whether the N-terminus of Par14 also showed a change upon substrate addition, the negatively charged substrate peptide was also added in the same concentration to the full-length ^{15}N-labeled Par14. The observed chemical shift changes were plotted against the residue number and compared to those of the isolated catalytic PPIase domain (Fig. A7). The chemical shift changes upon substrate addition were virtually the same in Par14 and in the isolated PPIase domain. The only conspicuous feature was that the amino acids His^{67} and Ile^{68} showed no change in Par14. For the N-terminus of Par14, the addition of the negative substrate did not result in any consistent changes. The only amino acid that showed a chemical shift change was the amino acid Gly^{33}. However, the chemical shift change was small, at 0.01 ppm.

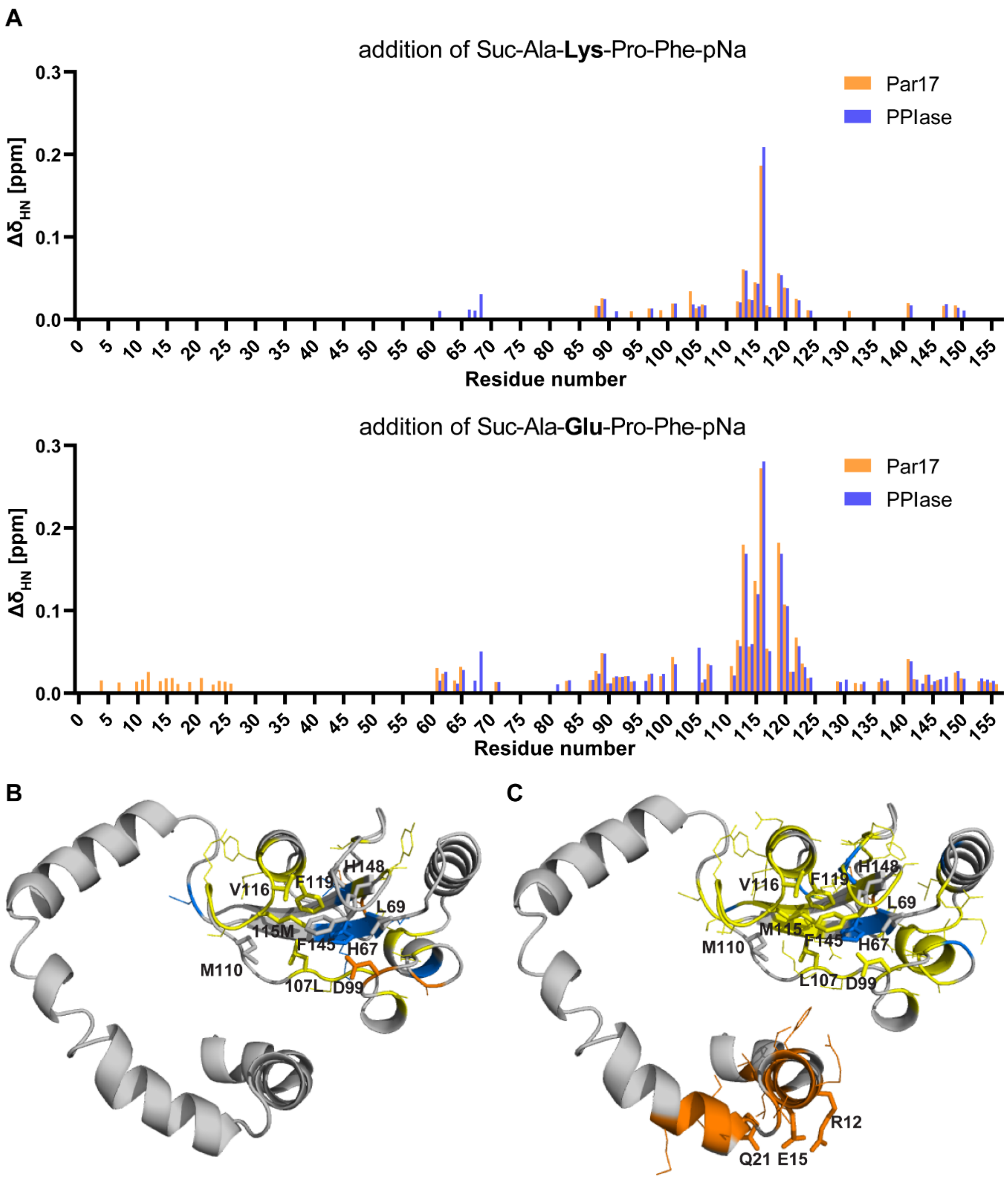

Figure 13: Shift changes in Par17 and the catalytic PPIase domain after the addition of a positive or negative charged representative of model substrate. A: Chemical shift changes measured for amide resonances of Par17 and the PPIase domain before and after addition of the model substrate Suc-Ala-Glu-Pro-Phe-pNa (3 mM) or Suc-Ala-Lys-Pro-Phe-pNa (3 mM). Shift changes were calculated from the overlaid BEST-TROSY-HSQC spectra recorded at 20 °C in 50mM KPi buffer at pH 6.7. **B, C:** Shift changes are highlighted on the I-TASSER structure of Par17. Shifts that occurred only in Par17 (orange) or in the catalytic PPIase domain (blue) and similar chemical shift changes between Par17 and the isolated catalytic domain (yellow) are emphasized. Shift differences between free and bound signals with Suc-Ala-Lys-Pro-Phe-pNa (B) and Suc-Ala-Glu-Pro-Phe-pNa (C) are highlighted. Residues important for catalysis and the strongest shifting amino acids in the Par17 N-terminus are emphasized as bigger sticks and labeled with the residue number.

The next step was to investigate how Par17 behaves with other substrate peptides for which lower substrate efficiency was observed. For this purpose, the model substrate with Val or Gly at the Xaa-Pro position was added to ^{15}N-labled Par17. Here, Val was chosen as a representative of the amino acid residue group of the nonpolar uncharged amino acids and glycine as an amino acid of the group of polar and uncharged amino acids. Upon addition of both substrate peptides with Val or Gly preceding proline, in the PPIase domain of Par17, the same substrate-binding pattern could be observed as for the Glu-Pro and Lys-Pro substrate peptide (Fig. A8, table A10). It is particularly noteworthy that the extent of the chemical shift changes for most of the residues within the PPIase domain upon addition of the two substrate peptides (Val-Pro, Gly-Pro) occurred between the shift changes caused by the other two substrate peptides (Glu-Pro, Lys-Pro). The chemical shift changes can be susceptible to small concentration differences or a slightly different pH and in these studies. The concentration of the ^{15}N-labeled proteins was always kept similar (between 190 µM and 350 µM) but was not identical. Nevertheless, the chemical shift changes of the two peptides (Val-Pro, Gly-Pro) confirm that the influence of the less efficiently catalyzed peptides caused a greater change in the PPIase domain than the substrate peptide with Lys at the Xaa position, which was one of the most efficient catalyzed. However, the most interesting observation is that the addition of the two substrate peptides (Val-Pro, Gly-Pro) also induced chemical shift changes in some of the additional 25 amino acids of Par17's N-terminus (discontinuously between residues Val^{11} and Lys^{25}), even though it was to a slightly lesser extent than Glu-Pro substrate peptide (Fig. A8 B).

It was also investigated whether the isolated N-terminus of Par17 is also capable of binding the substrate. The isolated ^{15}N-labeled N-terminus (Par17$_{\Delta 61\text{-}156}$) was purified as described in the material and methods section and BEST-TROSY-HSQC was recorded with the same settings as for the full-length proteins. The residues were assigned on the basis of the assignment of Par17 [124]. Next, the substrate peptides with Glu or Lys at the Xaa position were added to the isolated Par17 N-terminus and shift changes were monitored. With the substrate peptide with Lys at the Xaa-Pro position, no chemical shift changes could be determined in Par17$_{\Delta 61\text{-}156}$ with a final substrate concentration of 5 mM (Fig. A9A). For the substrate peptide in which Glu was preceding proline, chemical shift changes in Par17$_{\Delta 61\text{-}156}$ could be observed (Fig A9B, table A10). The changes were plotted against the residue number (Fig A10) and the addition of Glu-Pro substrate peptide (4.5 mM) showed a similar pattern to that of the full-length Par17. Even at a lower substrate concentration (3 mM), chemical shift changes could already be observed for the following four amino acids in the isolated N-terminus: Arg^{12}, Arg^{16}, Val^{19} and Gln^{21}. This indicates independent binding of the N-terminus to the substrate.

In summary, binding to the catalytic cleft can be observed for both the positively and negatively charged substrate peptides and the two additional measured substrate peptides (Val-Pro, Gly-Pro). The binding of the negative substrate peptide appears to have a greater effect on the protein. The substrate peptide triggers stronger shifting in both the isolated PPIase domain and in Par17 in the corresponding regions. Most strikingly, the N-terminus with the 25 amino acids unique to Par17 shows changes with the negative amino acid (Glu-Pro) in the substrate peptide preceding proline and the substrate peptides with Val and Gly at the Xaa-Pro position. With these substrate peptides the isomerization efficiency is lowered in Par17 compared to the shorter isoform. However, the N-terminus showed no changes upon addition of the peptide to the positive amino acid preceding proline (Lys-Pro), where the substrate efficiency of Par17 is similar in the shorter isoforms.

3.4 Interaction partners identified by photo crosslinking for Par17, Par14 and the isolated N-termini of Par14 and Par17

Since Par14 and Par17 prefer different substrates, the role of the different localizations of the two isoforms must now be considered in a new light. As these facts indicate that both parvulins have different binding partners and therefore might control different metabolic and signaling pathways. Therefore, in this work, we searched for possible interaction partners of Par14 and Par17. To capture weak interactions more efficiently, photo affinity labeling was used to cross-link the parvulins and their isolated N-termini to their interactors. For this purpose the proteins (Par17, Par14, Par17$_{\Delta 61\text{-}161}$-Strep (68 aa), Par14$_{\Delta 36\text{-}136}$-Strep (44 aa)) were recombinantly expressed by *E.coli.* The full-length proteins Par14 and Par17 were expressed in the presence of the photo amino acids L-photo-leucine and L-photo-methionine. During expression, the photo amino acids were incorporated into the proteins. After adding the labeled proteins to HeLa lysate, the samples were irradiated to covalently attach putative interactors. In a slightly different approach, the unlabeled N-termini were added to labeled HeLa lysate, in which the proteins had incorporated the photo-reactive amino acids and were irradiated. Following this, the parvulin-interactor complexes were isolated from the cell lysate by co-immunoprecipitation with bead-linked anti-PIN4 antibodies. The N-termini-interactor complexes were isolated using magnetic strep beads. To identify the putative interactors the complexes were digested on the beads and analyzed by liquid chromatography-mass spectrometry by the Analytic Core Facility Essen (ACE).

3.4.1 Interacting proteins of the full-length parvulins identified by mass spectrometry

For the full-length parvulins four technical replicates each were investigated. As a background control, non-irradiated, non-parvulin supplemented HeLa lysate was used in four technical replicates in each experiment. For peptide identification and relative quantification, the software MaxQuant was used by the Core Facility (ACE) to match the MS/MS spectra against a *Homo sapiens* database (Section 2.2.6). The identified Label-Free Quantitation (LFQ) intensities of the proteins were compared by the software Perseus. The intensities were logarithmized and false positive interactors (reverse proteins, the proteins that were only identified by site and potential contaminants) were excluded. Afterwards, proteins with at least three valid values out of four technical replicates of at least one investigated group were filtered out. In the cross-linking experiments with Par14 and Par17, 1265 and 1855 proteins remained, respectively. A two-sided t-test was calculated from the LFQ intensities of proteins identified in the Par14 or Par17 cross-linked samples in comparison to the non-irradiated, non-parvulin supplemented HeLa lysate (significant data points were determined with a permutation-based False discovery rate (FDR) for Par14 of 0.01 and Par17 of 0.05, S0 = 0.1 for both). The results of the p-values of the LFQ intensities were plotted against the differences between means in a volcano plot (published in Goehring et al. 2020, [37]). Above the cut off curve in the volcano plot 126, proteins could be identified as enriched in the cross-linking samples of Par14 and 56 in the crosslinking samples of Par17 [37]. As expected, in both samples PIN4 (Par14/Par17) is the protein with the highest difference compared to the lysate. This is because the recombinant protein was supplemented in high concentration and PIN4 was the target of the precipitation. For Par14 many ribosomal proteins could be identified with high differences compared to the HeLa lysate (RPL30, RPL36, RPS15A, RPS9 etc.). In the case of Par17 the most abundant proteins compared to the HeLa lysate were the survival motor neuron protein (SMN1) and probable ATP-dependent RNA helicase DDX20 (DDX20) both of which are part of the spliceosome [37].

When the proteins that were enriched in the Par14 and Par17 cross-linking experiments were compared, only eight of the 180 proteins were overlapping between Par14 and Par17 (Fig. 14, table A11). Remarkably, this result occurred in the experimental setting without cell compartments present, and the only difference between the two isoforms was the extended N-terminus. The overlapping proteins included four ribosomal proteins (RPLP0, RPS15, RPS27A, RPS28), aspartyl/asparaginyl beta-hydroxylase (ASPH), histone-1H1B (HIST1H1B); tubulin β-6 chain (TUBB6) and a zinc finger CCCH-type antiviral protein (ZC3HAV1) [37].

Although not many interactors of Par14 and Par17 are known, a few have been identified. Some of those interactors of PIN4 are listed in the Biological General Repository for Interaction Datasets (BioGRID, [133]), a database that holds and disseminates genetic and protein interaction data from high-throughput datasets and publications. In 2019 there were 38 interactors listed and only the 40S ribosomal protein S19 (RPS19) overlapped with the proteins enriched by the cross-linking experiment of Par14 [37]. Since that time, seven additional interactors have been added to the database (Protein bicaudal D homolog 2 (BICD2) [109], ewing's tumor-associated antigen 1 (ETAA1) [1], three erbB receptor tyrosine-protein kinases (ERBB2, ERBB3, ERBB4) [59], the non-structural protein of SARS-CoV-2 (ORF8-COV2) [69] and heterogeneous nuclear ribonucleoprotein H1 (HNRNPH1)) [150]. Still, RPS19 remains the only interactor overlapping with the identified interactors in the cross-linking experiment (Fig. 14, table A11).

Additionally, research by Fujiyama et al. [33, 34] uncovered interactors of Par14 from nuclear extract by precipitation with GST-Par14 identified by mass spectrometry. It was discovered that 114 proteins were associated with the pre-ribosomal ribonucleoprotein (pre-rRNP) complexes and 46 of them, mainly ribosomal proteins, were overlapping with the interactors of Par14 identified in this work. Two of the overlapping interactors (TUBB6 and HIST1H1B) were also enriched in the Par17 cross-linking experiment [37]. The overlapping of the data reinforces the finding that these proteins are interaction partners. In another study, interactors of PIN4 were investigated where PIN4 was likely to be phosphorylated at the amino acids Tyr^{122}/Tyr^{147} in Par14/Par17 [32]. The phosphorylation of PIN4 occurs in the examined cancer cell line due to the mutation of the Fibroblast growth factor receptor 3 with a cytoplasmic tyrosine kinase domain. A comparison of the proteins disclosed four proteins also enriched by either Par14 or Par17 in the crosslinking experiments (Fig. 14, table A11). The candidates overlapping for Par14 were three ribosomal proteins (RPL32, RPS5, RPL6) and Y box binding protein 1 (YBX1). For Par17 the candidates were two proteins that are involved in transport, namely the sodium/potassium-transporting ATPase subunit alpha-1 (ATP1A1) and transportin-1 (TNPO1), as well as lysophosphatidylcholine acyltransferase (LPCAT1) and trifunctional enzyme subunit alpha (HADHA).

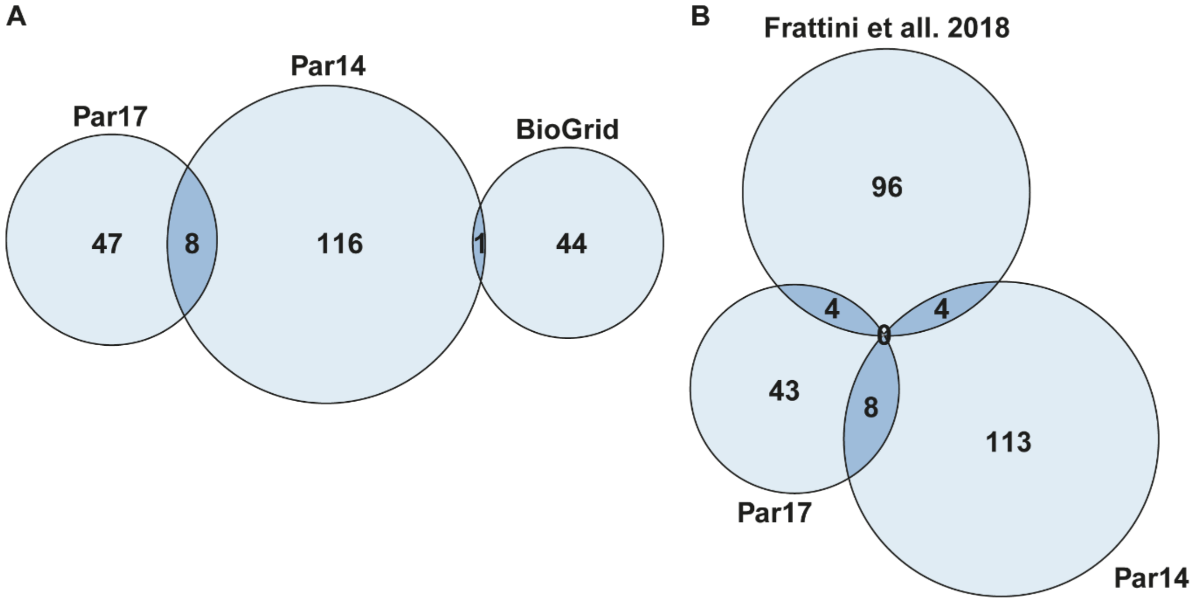

Figure 14: Relations between interactors of Par14 and Par17 identified by different analysis methods shown in a Venn diagram. The overlap of interactors from photo cross-linking of Par14 and Par17 (this work) with interactors (of PIN4) from BioGRID DB [133] (left) and with the interactors found by Frattini et al. [32] (right) were depicted. PIN4 was excluded from the comparison.

To gain an overview of which processes the identified interactors are involved in, the enriched proteins of Par14 and Par17 were categorized. The categorization was based on the information from the databases KEGG, GOBP, GOMF, GOCC implemented in Perseus and on additional information from UniProt (published in Goehring et al. [37]). Based on this data Par14 participates in the pre-ribosomal ribonucleoprotein (rRNP) complexes as already demonstrated by Fuijyama-Nakamura and coworkers [33]. Par14 is also indicated to participate in RNA- and DNA-directed processes. These processes include splicing (e.g. ALREF, HNRNPM, HNRPU, SF3B2, SRPK1), DNA-repair and DNA-remodeling (e.g. DHX9, DNAJC9, GRWD1, PARP1, TOP1, XRCC6) [37]. As expected from Par17 localization, Par17 was associated with mitochondrial proteins, which includes proteins of the respiratory chain (e.g. COX2, COX20, CY1, NDUA5, NDUS8) and β-oxidation (MFF, HADHA/ECHA, STML2) [37]. In addition, a connection of Par17 with many proteins of internal cell transport could be determined, among them transport proteins of the Golgi apparatus and endoplasmic reticulum (e.g. ASPH, COPB, COPG1, SEC22B, SRPRA, OST48, SSRD). The proteins of internal transport are also associated with another protein class, proteins of the cytoskeleton, which Par17 was found to interact with as well (e.g. ACTB, CAN2, ITA6, RASN, TBA4A, TBB4B, TBB6, PRAF3). These proteins are involved in transport, but are also responsible for cell dynamics and cell motility [37]. A function in this area has previously been suggested [14, 142].

3.4.2 Interacting proteins of the N-termini of the parvulins identified by mass spectrometry

Since the only difference between the two parvulin isoforms is the elongated N-terminus of Par17, it is reasonable to assume that this difference is responsible for the different interaction partners. Therefore, it was investigated which interaction partners could be found when using both isolated N-termini (Par17$_{\Delta 61\text{-}161}$-Strep, Par14$_{\Delta 36\text{-}136}$-Strep) in an interaction study and whether some interaction partners of the full-length proteins could be confirmed.

As described in the material and methods section (Section 2.2.6), the purified Strep-tagged N-termini were each added to the photo amino acid labeled HeLa lysate, irradiated and precipitated. An isolated Strep-tag was added to the labeled HeLa lysate as a reference sample, as the tag can also influence interactions. After precipitation, the protein complexes were digested and analyzed by mass spectrometry by the ACE facility. The software MaxQuant was used for peptide identification and relative quantification of the MS/MS signals of four technical replicates of each application. Afterwards the delivered LFQ intensities were processed and analyzed by Perseus. The values were logarithmized and false positive interactors were removed (potential contaminants, reverse proteins and the proteins that are only identified by site), 1680 identified proteins remained as possible interactors. To filter out relevant interaction partners, the result of the t-test of the LFQ intensities was plotted against the appearance ratio of the respective signals in a volcano plot. A cutoff curve of an FDR of 0.01 yielded 54 enriched proteins for the Par14 N-terminus and 106 for the Par17 N-terminus (Figure and table published in Goehring et al. [37].

The interactors found for the varying length N-termini of Par14 and Par17 were compared with each other, and 35 superordinate proteins were found (Fig. 15A, table A12). The overlapping identified proteins were more than the eight matching interactors for the full-length parvulins, and one-third of the overlapping proteins are ribosomal. However, there are also differences, especially for Par17's N-terminus where 71 additional proteins were enriched.

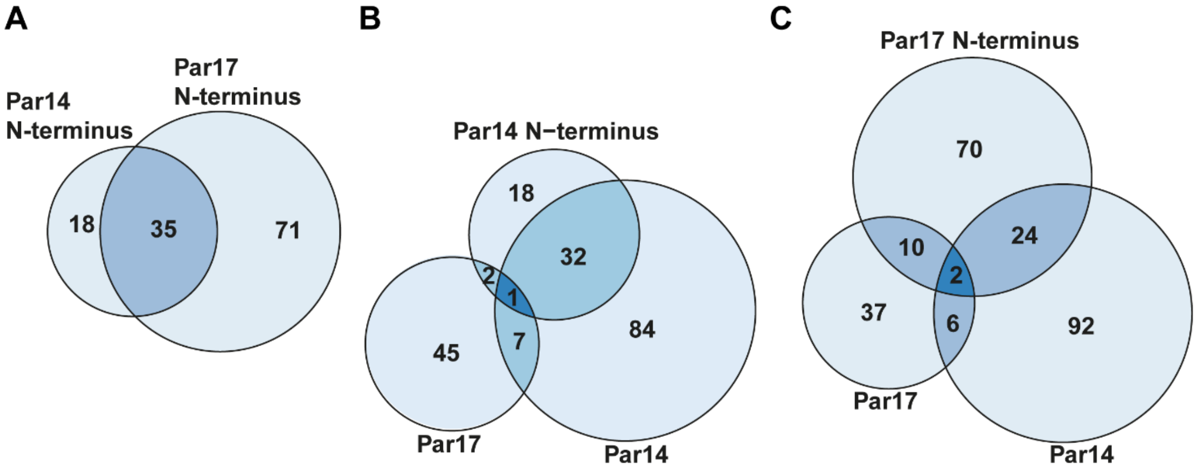

Figure 15: Comparison of the interactors enriched by the Par14 N-terminus and Par17 N-terminus with the interactors found for the full-length parvulins in a Venn diagram. **A:** The overlap of interactors identified for the varying lengths of N-termini of Par14 (44aa) and Par17 (68 aa). B: Number of the common and distinct interactors identified for the N-terminus of Par14 and the full-length protein Par14. **B:** Overlap of interactors of the Par17 N-terminus with the interactors found for the full-length proteins Par17 and Par14. PIN4 was excluded from comparison.

In terms of the comparison between the enriched proteins of the N-termini (Par17$_{\Delta 61\text{-}161}$-Strep, Par14$_{\Delta 36\text{-}136}$-Strep) and the full-length proteins (Par14, Par17), the agreement between Par14 and its N-terminus was high (Fig. 15B, table A12). About one-third of the enriched proteins of Par14 N-terminus were also identified to interact with the full-length protein. Of the 33 overlapping proteins, 20 were proteins that are part of the ribosome. Additionally, the N-terminus enriched heterogeneous nuclear ribonucleoproteins (HNRNPA2B1, HNRNPDL, HNRNPH1, HNRNPK), of which six others have already been identified as potential interaction partners by Par14 (table

A12). Three proteins identified by the Par14 N-terminus were overlapping with the interactors enriched by Par17 (COPG1, HADHA, HIST1H1B).

For the N-terminus of Par17, the agreement with the proteins that could be enriched by the full-length protein was not as high. However, 12 proteins could be identified in both enrichment experiments. This corresponds to one fifth of the proteins enriched by Par17. Among these proteins, the main group belongs to the cytoskeleton (ACTB and three tubulin subunits, table A12). In addition, it was striking that of the 106 proteins enriched by Par17's N-terminus, 26 proteins were also enriched by Par14, which was more than the overlap between full-length Par14 and Par17. More than half of the overlapping proteins were ribosomal proteins.

Overall, the impression that the additional 25 amino acids in which the two N-termini and parvulins differ are responsible for binding of a different set of interaction partners is strengthened. In addition, the experiment provides further evidence for some proteins as interaction partners, and suggest new proteins that could also be considered as potential interaction candidates.

To link the new identified interactors to a cellular role, the enriched proteins from the N-termini were categorized based on the information from different databases (KEGG [55], Gene ontology resources: GOBP, GOMF, GOCC [140] and UniProt [141]) included in Perseus.

The enriched proteins of the Par14 N-terminus could be categorized into four groups (Fig. 16A, table A13). The largest group comprises the RNP-complex associated proteins. This group also showed the greatest agreement with the proteins found for full-length Par14. 20 of the proteins included were also found for the full-length Par14 and most of the proteins were ribosomal. This confirms the participation in pre-ribosomal ribonucleoprotein (rRNP) complexes already described by Fujiyama et al. [33, 34]. Furthermore, three signal recognition particle subunits were identified for the Par14 N-terminus (SRP9, SRP68, SRP72). The signal recognition particle is involved in the targeting of synthesized proteins from the ribosome to the endoplasmic reticulum and is normally made up of six subunits and a 7SL RNA [131]. In addition to two identical subunits identified by the N-terminus of the full-length protein, the subunit SRP14 could be identified. This points to an additional, more general function of Par14 in ribosomal ribonucleoproteins.

The other two groups, DNA- and RNA-directed processes, were also the same for the Par14 N-terminus and the full-length protein, even though the agreement of the proteins found for these groups were smaller. For the Par14 N-terminus and full-length Par14 protein in the category of DNA repair and chromatin remodeling, four of the eight identified proteins for the N-terminus were overlapping (XRCC6, DHX9, HIST1H1B, HIST1H1E). The X-ray repair cross-complementing proteins (XRCC6, XRCC5) identified by the Par14 N-terminus are connected to DNA repair. Proteins such as histone acetyltransferase type B catalytic subunit (HAT1) and histones (HISTH1B, HIST1H1E) are involved in chromatin remodeling. For the Par14 N-terminus and full-length Par14, only one protein is overlapping in the category of RNA binding and processing (NSUN2). The RNA cytosine C(5)-methyltransferase NSUN2 (NSUN2) methylates cytosine to 5-methylcytosine (m5C) in various RNAs [143] and stabilizes it. Moreover, four heterogeneous nuclear ribonucleoproteins (HNRNPA2B1, HNRNPDL, HNRNPH1, HNRNPK) were enriched by the Par14 N-terminus. The full-length Par14 also enriched seven other HNRNPs, which are classified in the same category. According to the KEGG database [55] the HNRNP proteins are either part of the spliceosome (Par14 N-terminus: HNRNPK; Par14 FL: HNRNPM, HNRNPU, HNRPA1) or associated to the spliceosome (Par14 N-terminus: HNRNPDL, HNRNPH1, HNRNPA2B1; Par14 FL: HNRNPA0). Approximately 10% of the enriched proteins could not be clearly assigned to a group.

Another way to categorize proteins is through the use of the STRING database [138] with a cluster algorithm. The STRING database holds information about known and predicted protein-protein interactions. By entering the gene names of the identified proteins and the organism *Homo sapiens*, all predicted and known interactions between the proteins in the database are returned in a network. The interaction is rated by a score and the certainty is reflected by the thickness of the lines. Based on the score, the interactions can be clustered by the Markov Cluster (MCL) algorithm. In the case of the Par14 N-terminus for the identified proteins, two main clusters appeared (Fig. 16C, table A14). The largest cluster (red) comprised ribosomal proteins and thus coincided with the largest category of RNP-complexes. The second cluster (yellow) included proteins associated with RNA and DNA associated processes. The fact that the categories for these processes occurred in one cluster and in several small connections could be due to the size of the network. If the number of proteins entered into the STRING database is small, the algorithm groups proteins into larger groups [12]. In addition, many of the proteins found act in different processes that often involve DNA and RNA, for example splicing. However, collectively, the enriched proteins of N-terminus reinforced the cellular functions predicted for Par14.

The enriched proteins of the Par17 N-terminus could be categorized in nine groups (Fig. 16B, table 15). One of the largest was the group of ribosome organization, which comprises 18 proteins and overlapped strongly with the enriched proteins of the full-length protein Par14. Two other large groups, RNA and DNA associated processes, comprising 15 and 9 enriched proteins, respectively, also showed a strong overlap with the full-length Par14. These three groups are mainly comprised of previously mentioned proteins. The group of ribosome organization proteins was mainly made up of ribosomal proteins. The group of RNA binding and processing proteins included, among others, HNRNP proteins. The DNA repair and chromatin remodeling group included different histones and XRCC6.

More noteworthy were the other groups that were either more consistent with the cellular functions found for the full-length Par17 or newly identified. These were the groups of internal transport, internal cell motility, oxidative phosphorylation, lipid metabolism and amino acids metabolism. Among these, the largest group is the internal cell motility comprising 18 enriched proteins. Five proteins were enriched from both the Par17 N-terminus and the full-length Par17, which were subunits of tubulin and actin (TUBA4A, TUBB4B, TUBB6, ACTB). They were thereby strengthened as proper interaction partners. Also noticeable were the identified subunits of the chaperonin-containing T-complex (TRiC) (CCT3, CCT4, CCT5, CCT6A, CCT8) enriched by the Par17 N-terminus. This complex is probably involved in the cilia function and in chaperoning actin and tubulin folding [35, 129]. Another large group with 16 interactors was the internal transport proteins. An overlap between the proteins of the Par17 N-terminus and the full-length protein in this group could be observed for three proteins (SEC22B, KPNB1, TNPO1). These proteins are involved, in addition to others in this group, in transport between the ER and Golgi (SEC22B, RAB14, RAB1B), mitochondrial transport (SLC25A13, SLC25A5, SLC25A6) and nuclear transport (KPNB1, TNPO1, KPNA2). Moreover, for the full-length Par17 seven proteins could be identified in energy conversion [37]. For the Par17 N-terminus, a more detailed impression could be elucidated. Six proteins that are fundamental components of oxidative phosphorylation were enriched (UQCRC2, ATP1A1, ATP5A1, ATP5B, ATP5C1, ATP5J2). In addition, two proteins were found to have a function in fatty acid degradation (β-oxidation) (HADHB, HADHB), and were assigned to the new group of lipid metabolism. In this group a total of six proteins were classified. Another group was established comprising five proteins that are involved in amino acid metabolism (PHGDH, GCLM, GPC1, CPS1, MAT2A). Since no proteins of this group could be found for the full-length proteins, a function in this area remains uncertain. Again, about 10% of the enriched proteins could not be assigned to any group, among them different heat shock proteins with elusive functions (HSP90AA1, HSP90AB1, HSPA5, HSPA8).

To obtain an impression of the quality of the grouping, the gene names of the enriched proteins from Par17 were used to create a network in the STRING database (Fig. 16A, table A16). The network revealed three large distinct clusters (red, orange and purple) and a rather diffuse large group (yellow). The other clusters were smaller accumulations. The largest cluster (red) comprised 36 proteins and included proteins from the group of ribosomal organization and most of the proteins from the group RNA binding and processing. The second largest cluster with 19 proteins (orange) comprised the proteins classified in the internal cell motility group. The third cluster (purple) contained mitochondrial proteins, including all proteins of the oxidative phosphorylation group. The more distributed cluster (yellow) did not coincide with any of the groups and mainly contained proteins of the groups associated with DNA and RNA processes. The proteins of internal transport were either associated with the larger clusters or formed smaller clusters of four or less proteins (e.g. the light blue cluster). Three proteins of the category lipid metabolism are also clustered together in the network (dusty pink). A cluster of the proteins classified in the group amino acid metabolism could not be observed. Still, there are many similarities between the categories and the clusters, reinforcing the functional categories.

In the network of proteins enriched by the Par17 N-terminus, as in the other networks, the gene of Par17 was added (PIN4). In this network, for the first time, a predicted or specific interaction of PIN4 with the enriched proteins was observed in comparison to the full-length proteins and the Par14 N-terminus. Three interactions of different confidence were observed. The interaction with the highest confidence was with the bifunctional glutamate/proline-tRNA ligase (ERPS; score = 0.675). The score was made up by neighborhood on chromosomes, co-expression and text mining. It was followed by the interaction with T-complex protein 1 subunit epsilon (CCT5; score = 0.520). The score was composed of experimentally proven interactions and text mining. The third interaction found was with the heat shock protein HSP 90-α (HSP90AA1 score = 0.406) with a score slightly over the threshold. The score was obtained by values of neighborhood on chromosomes, co-expression and text mining. The presence of the predicted or known interactions reinforces that these proteins are true interaction partners. Nevertheless, only the interactions of the N-terminus were shown and the role of the PPIase domain in the interaction must also be taken into account. Therefore, mass spectroscopy is suitable for obtaining a first insight into the function and interaction of a protein. However, the identified interaction partners and functions in mass spectroscopy should still be confirmed by other methods.

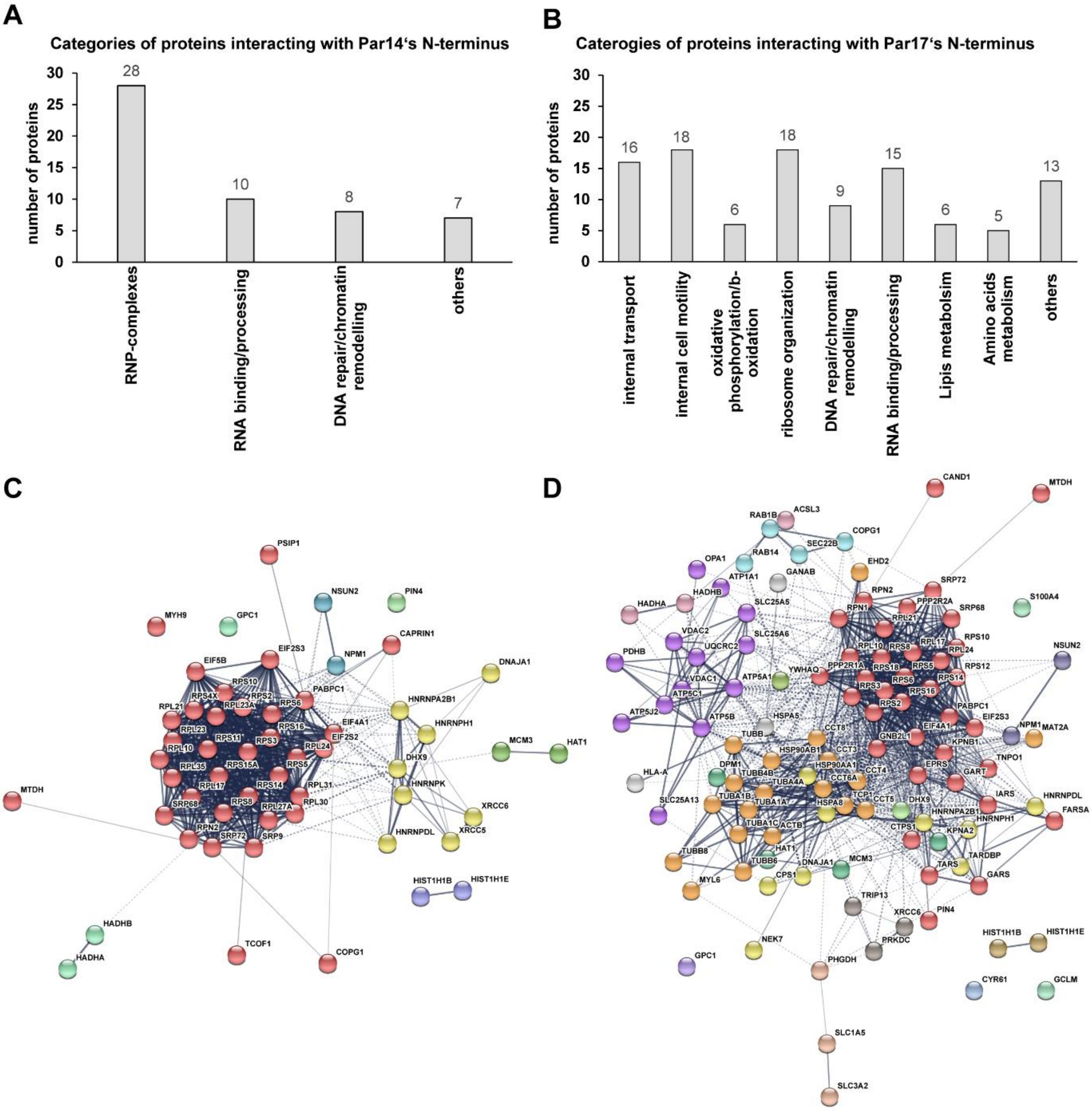

Figure 16: Categories of interactors from the N-termini of Par14/Par17 and their protein-protein interaction network. The enriched proteins of the **A:** Par14 N-terminus and **B:** Par17 N-terminus were grouped into functional categories based on the information of the databases KEGG, GOBP, GOMF, GOCC and UniProt. The protein-protein network of predicted and known interactions of the proteins from the organism homo sapiens were generated by the STRING server through the input of the gene names of proteins enriched by the **C:** Par14 N-terminus or **D:** Par17 N-terminus. The nodes in the network correspond to the gene and the edges are the known or predicted connections. The thickness of the lines reflects the confidence of the interaction, which was set to medium (score > 0.4). Matching colors of the nodes indicate clusters calculated based on the score for each interaction with the Markov Cluster Algorithm (MCL). Proteins of a cluster have a high probability of interacting with each other.

3.5 Function of Par17 in actin polymerization and migration

Recently a role for Par17 in microtubule assembly in vitro was demonstrated [142]. In addition to tubulin as an interaction partner for Par17 and the Par17 N-terminus, actin as part of the cytoskeleton and a variety of its binding proteins were identified as possible interaction partners. Therefore, a possible binding of Par14/17 to actin was investigated [37].

For this purpose, non-muscle actin was added stepwise to the fluorescently labeled (Atto594) parvulins and the changes in fluorescence anisotropy were measured (Fig. 17A). The calculated dissociation constant revealed that the binding of Par17 to non-muscle actin with a K_D of 0.7 µM assuming a 1:1 binding model was about 5 times stronger than the binding of Par14 with a K_D of 4 µM [37].

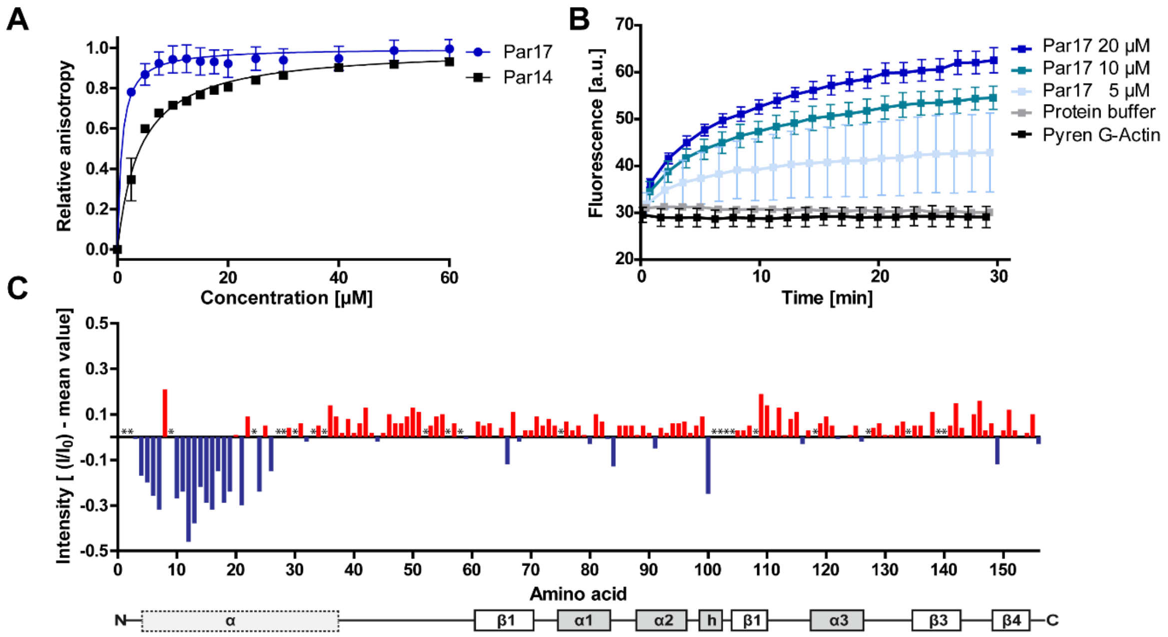

Figure 17: Par17 function in actin binding and polymerization. **A:** “Saturation curves monitoring the changes within fluorescence anisotropy of Atto-labeled Par14/17 (100 nM) when adding increasing amounts of non-muscle actin. The binding curves were fitted to triple experiments and exhibit R2 values of 0.88 (Par17) and 0.96 (Par14).” [37] **B:** “Time dependence of polymerization of non-muscle actin monitored by pyrene-actin fluorescence. Each experiment was done in three replicates in presence of various amounts of Par17.” [37] **C:** “Plot of intensity changes within NH resonances observed in an 1H-15N-HSQC spectrum of Par17 by addition of non-muscle actin. Differences were calculated from mean signal values in absence and presence as described in material and methods. Blue bars depict intensity changes that are smaller than the calculated mean intensity changes, while the red ones represent those that are higher. Asterisks represent amino acids, which intensity changes could not be determined. The changes are mapped to the secondary structure of Par17; the N-terminus is only predicted to be α-helical.” [37] Republished with permission of Walter de Gruyter and Company, details can be taken from the references section.

Furthermore, it was investigated whether Par17, in addition to binding, also has an effect on the polymerization of actin. Actin polymerization can be simply and flexibly reconstituted in vitro by using pyrene labeled actin [24]. Human non-muscle actin was prepared in a solution with a 1:10 ratio between actin and pyrene labeled actin that favors the monomeric form. Polymerization could be tracked by an increase in fluorescence intensity (Section 2.2.9). Upon addition of varying concentrations of Par17 to the actin solution, polymerization could be observed (Fig. 17B). The polymerization occurred in a concentration dependent manner [37].

To determine the putative binding regions of Par17 and actin different approaches were chosen. Initially a ^{1}H-^{15}N-HSQC spectrum of ^{15}N-labeled Par17 (290 µM) in the absence and presence of 45 µM non-muscle actin was recorded and changes in amide peak intensity were monitored (Section 2.2.8, Fig. 17C). In the presence of actin an intensity reduction was observed within the catalytic domain for the residues Arg^{66}, Leu^{84}, Lys^{100} and Ile^{149}. The most striking reductions were in the region of the unique part of the N-terminus of Par17. A reduction in signal intensity was observed for almost all 25 amino acids with the greatest effect for residue Arg^{12}. As there was only the one set of reduction in signal intensities, it indicated a putative binding epitope of Par17 to actin. Additionally, it was consistent with the observation that actin was found to be an interactor of Par17 and the Par17 N-terminus but not of Par14 and its N-terminus in mass spectrometry [37].

Furthermore, a peptide array was designed based on the amino acid sequence of actin. A library of overlapping peptides (12-mers), each shifted by two amino acids across the entire sequence of β-actin (Aa 1-375), was immobilized repeatedly on cellulose membranes (Helmut Tourné, AG Ehrmann). The membranes were incubated with either fluorescence labeled Atto594-parvulins or the Atto594-dye (Section 2.2.11, Fig. 18A). Dark spots signified interactions between the single 12-mer peptide and the parvulins. All sequences with a length equal to or greater than three were classified as possible binding sites. The unpaired Atto594-dye showed no interaction with the peptides. For Par14, four sequences could be recognized. Three of the sequences ranging from B3-E3, D4-J4 and H9-J9 overlapped with the sequences identified for Par17. One unique sequence that could only be observed for Par14 ranged from G6-I6. Nevertheless, Par17 showed a clearly stronger binding to the peptides owing to a higher intensity of the spots as well as the higher number of possible binding sequences. In total ten sequences could be determined for Par17 as putative binding sites with the strongest and largest ranging from N1-T1, D4-L4, N5-R5, C7-H7 and D9-J9.

For a better correlation of the results, the two proteins were additionally cross-linked with DSSO (Section 2.2.3 and 2.2.6). The cross-linking of actin and Par17 could be observed in an SDS-gel (Fig. A11). Cross-links were analyzed by mass spectrometry and identified with the program Proteome Discoverer and the search engines SEQUEST and XlinkX by the ACE facility (Table A17). The resulting cross-links were further analyzed by xiView Analyzer and cross-links between Par17 and actin with a score >130 were depicted in a 2D network (Fig. 18B). Four interaction regions were identified by the DSSO cross-linking on the actin side and two more fenced regions on the Par17 side. Three regions identified in the cross-linking for actin agree with the putative binding sides from the peptide array experiment. The region in actin for which the most cross-links were found is the one between the actin residues Gly^{188}-Pro^{204}. Furthermore, in Par17, cross-links were found with actin in the first 25 amino acids of the N-terminus and some cross-links were also found for Lys^{100}, which showed intensity differences in the HSQC spectra after the addition of actin. Overall, the cross-linking results reinforced the identified putative binding sites of actin and Par17.

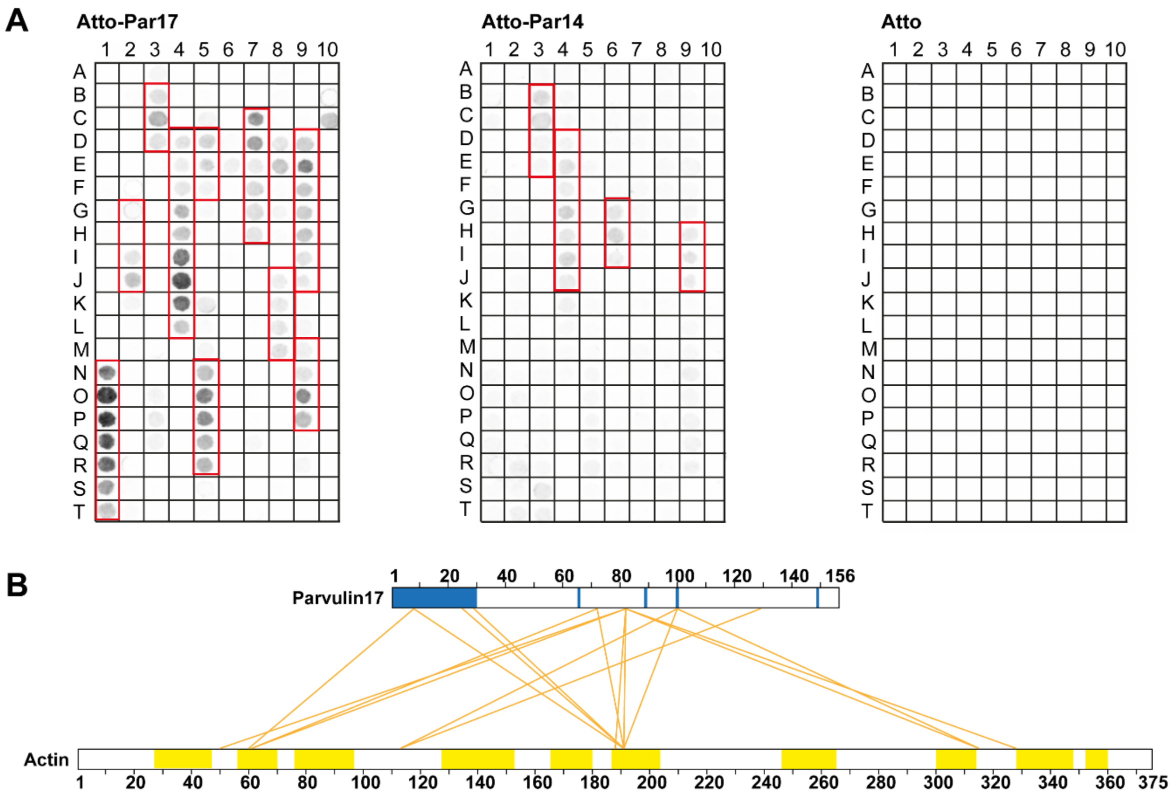

Figure 18: Defining the binding of Par17 and actin using peptide spotted array and cross-linking. A: Peptide array with 12-mers of β-actin amino acids (Peptide walk: 2 amino acids per step) incubated with Atto594-labeled parvulins to identify putative binding sides of actin. The membranes were processed after incubation with Atto594-Par17 (left), Atto594-Par14 (middle) or the unpaired Atto594-dye (right). **B:** The binding of actin and Par17 was anchored by the cross-linker DSSO and the cross-links were analyzed by mass spectrometry. Crosslinks found with a score higher 130 were depicted by the connection of the residue numbers. The amino acids of Par17 with reduced intensities in the presence of actin (blue) and the putative actin binding regions of Par17 (yellow) are highlighted.

Subsequently, the polymerization ability of the parvulins was examined in detail and certain properties like the presence of the N-termini and requirement of catalytic activity was evaluated. For this purpose, the same amount of different isoforms, the isolated catalytic domain and a catalytically restricted mutant of Par17, Par17$_{D99A}$ were measured in the non-muscle polymerization assay (Fig. 19A). The isolated catalytic PPIase domain did not have the ability to polymerize actin. Full-length Par14 was most efficient in polymerizing actin. Par17 with its additional 25 amino acids at the N-terminus could polymerize actin around 30% less effectively than its truncated isomer. Moreover, the Par17$_{D99A}$ mutant showed about a 50% reduced polymerization capability in comparison to the catalytic fully active Par17 [37]. For the substitution of Asp99 with an alanine in Par17 it was demonstrated that the k_{cat}/K_M of the enzyme was reduced by one order of magnitude [142]. The decline of the polymerization ability of the catalytically inefficient Par17 revealed the participation of *cis*/*trans* isomerization in polymerization *in vitro*. Furthermore, the presence of the N-terminus was necessary for actin polymerization and in conclusion the necessary for the physical interaction between Par14/Par17 and actin [37].

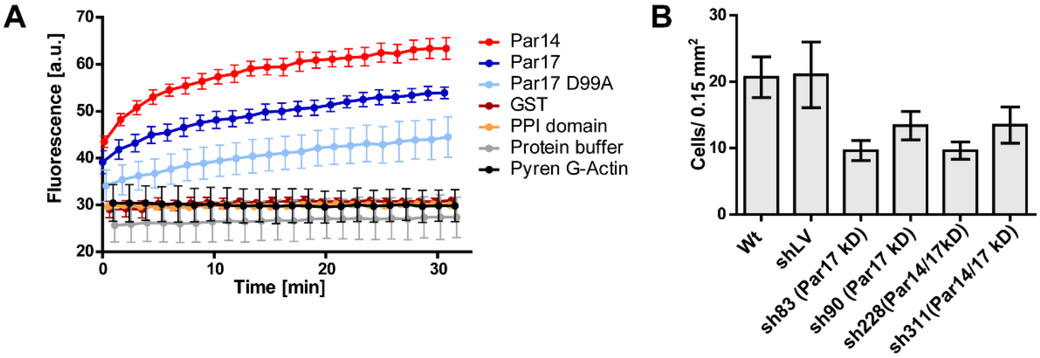

Figure 19: Actin polymerization and influence on cell motility. A: "Time dependence of polymerization of non-muscle actin monitored by pyrene-actin fluorescence. Each experiment was done in three replicates in presence of equal amounts (20 µM) of either Par17, Par14, PPIase domain or Par17D99A. GST was used as a negative control." [37] **B:** "Migration of knockdown cells were compared to WT cells by counting the migrated cells in defined areas. 25 areas were chosen by chance and counted per experiment with three different DAPI filters each. For each cell line 5 experiments were performed." [37] Republished with permission of Walter de Gruyter and Company, details can be taken from the references section.

Actin and tubulin are major components of the cytoskeleton and have a main function in cell migration. Actin is the driving force of the motion with a fast-growing side and slow-growing side causing polarization and resulting in membrane protrusion [113]. Microtubules built by tubulin function as transport tracks, as compressive elements, as signaling platforms and generate force during motion [36]. Since Par14/17 could influence polymerization of both proteins *in vitro*, it was investigated whether an influence of the parvulins on the functions in which actin and tubulin are involved can also be observed in living cells. Therefore, a stable knockdown of Par17 or Par14/17 was introduced into HCT116 cells. The knockdown was confirmed on the RNA level and showed a reduction of about 50% relative to the wild type (WT) on the protein level (Goehring). The cell migration of the HCT116 knockdown and control cell lines on collagen-coated wells through a membrane with 8 mm pores was then evaluated by fixing, staining and counting using microscopy as read-out tool [37] (Fig. 19B, section 2.2.15, experiments performed by Irina Michin, Tina Gerdes and Nina Schulze, except for the protein level determination of the knockdown and the evaluation). Migration was reduced by approximately 50-60% for all knockdown cell lines and was unequivocal distinguishable from the migration of the WT cell line in three cases (sh83, sh90, and sh228). This included the two knockdown cell lines in which only Par17 was downregulated, suggesting a functional role of Par17 in the process of cell migration [37].

3.6 Function of Par17 in energy conversion

Recombinant Par17 was demonstrated to be transported to the inner mitochondrial matrix in a membrane potential dependent manner, with the N-terminus functioning as a mitochondrial targeting and import sequence (MTS) [61]. Nevertheless, the function of Par17 within the mitochondrion remains obscure. The interaction partners identified in the cross-linking experiment point to a function of Par17 in energy conversion, particularly in oxidative phosphorylation. During this process, the energy stored in the relatively weak double bond of O_2 is released and used to produce adenosine triphosphate (ATP). The consumption of O_2 in a cell can be determined and this was done using in a Seahorse Cell Mito Stress Test to assess the oxidative phosphorylation pathway. To determine the influence of Par17 in oxidative phosphorylation, the Par17 knockdown cell lines HCT116 sh90 and sh83 were measured in the assay and compared with the results from the control cell lines.

Ideally, the influence should also be determined in another knockdown cell line. For this purpose, additional Par17 knockdown cells were generated using the clustered regularly interspaced short palindromic repeats (CRISPR)-Cas9 system [105]. HEK293 cells were transfected with a vector containing the gene for the modified Cas9 nuclease and the precise guidRNA to target the start sequence of Par17 (section 2.2.16). In one trial with only the guidRNA sgRNA3, it was desired that after cleavage by the nuclease, the sequence would be repaired by non-homologous end joining, resulting in changes to the start sequence. In another trial with the guidRNA sgRNA2 and an additional single stranded DNA template, in which the start codon of Par17 was altered, it was assumed that homologous recombination repair would take place. Both attempts resulted in a HEK293 clone (sgRNA3 = K3.9 and sgRNA2 = K2s.4) with changes in the sequence at the desired region and a reduced relative protein production of about 30% (Fig. A12).

During the Mito Stress Test the oxygen consumption rate (OCR) is measured under different circumstances [10, 119]. First, the basal respiration is determined, which is equivalent to the consumption of oxygen and the production of ATP under normal conditions of the cells. Then, the ATP synthase is inhibited by the addition of Oligomycin and only the oxygen consumption, which is not associated with the ATP production, is measured. This includes the oxygen conversion that occurs independently of the ATP synthase and is driven by a proton leak. The difference between the basal respiration and the protein leak correlates with the ATP production under normal conditions. Subsequently, the oxygen conversion is measured after the addition of the uncoupler FCCP. FCCP transports the hydrogen ions across the membrane and causes the respiratory chain to operate at maximum capacity. Finally, the oxygen conversion is measured after the addition of the inhibitors Rotenon and Antimycin A. These inhibit, respectively, complexes CI and CIII of the respiratory chain. The inhibition reveals the amount of oxygen turnover triggered by other cellular enzymes that consume oxygen.

Prior to the measurements of the assay, the optimal concentrations of the compounds and the seeding density of the cells had to be determined (Section 2.2.17). For the HCT116 cells the optimal seeding density was 70.000 cells/well, the concentration for Oligomycin was 1 µM, for FCCP 2 µM, and for Rotenon and Antimycin A 1 µM. For the HEK WT cells the best conditions were a seeding density of 80.000 cells/well and the same compound amounts as used for the HCT116 cells. The HEK knockdown cell lines were found to always be detached from the surface and washed away during the measurement process. It was concluded that they were not suitable for the assay. Therefore, the measurements were performed only with the HCT116 cell lines.

The results for one Mito Stress test were depicted in a flow chart where the oxygen consumption rate of the HCT116 cells was measured at different time points with the described treatments and was normalized to the number of cells/well (Fig. 20A). The mean of one measurement contains the data from five technical replicates per cell line (except HCT116 sh83: four replicates). The flow diagram revealed a tendency of the basal respiration and the maximal respiration in the knockdown cells (sh83, sh90) to be slightly higher than in the control cell lines (WT, empty vector LV). The biggest difference of the means between the LV cell line and the knockdown cell line (sh90) measured in the experiment was 50 $\text{pmol}\cdot\text{min}^{-1}\cdot$normalization(norm.) unit^{-1} in the maximal respiration. Small changes were also indicated in the proton leak and non-mitochondrial respiration.

To get a more accurate impression, the experiment was repeated two more times with five replicas each (except for the WT, which was repeated only once). The data for the individual respiration components was normalized to the values of the LV and combined (Fig. 20B, table A18), after which the tendency that had been indicated in the flow diagram was more clearly visible. The basal respiration, the ATP linked respiration and the maximal respiration were higher in the knockdown cell lines. The biggest effect could be observed in the ATP linked respiration, which was 1.5 times more efficient in the knockdown cell lines (sh83, sh90) compared to the control cell lines (WT, LV). For example, the mean OCR in ATP-linked respiration for the LV cell line was 117 $\text{pmol}\cdot\text{min}^{-1}\cdot\text{norm.unit}^{-1}$ and for the knockdown cell line sh90 was 152 $\text{pmol}\cdot\text{min}^{-1}\cdot\text{norm.unit}^{-1}$, depicted in the flow diagram. For the proton leak, the tendency remained that this was slightly higher in the knockdown cells, but with overlapping confidence intervals. For the knockdown cell line sh90 the tendency was not confirmed. Non-mitochondrial respiration of the knockdown cell lines did not appear to differ from the control cell line with the empty vector (LV). However, the non-mitochondrial respiration was reduced about 50% in the WT in comparison to the cell line with the empty vector (LV). Under the unlikely assumption that there is a difference in proton leakage and non-mitochondrial respiration between the control cell lines and the knockdown cell lines, the measured values and not the ratios were considered again. For example in the depicted measurement (Fig. 20A) the OCR difference of the proton leakage and non-mitochondrial respiration between the knockdown cell lines and the LV cell line had a maximum of about 15 $\text{pmol}\cdot\text{min}^{-1}\cdot\text{norm.unit}^{-1}$. Consequently, it cannot be sole cause for the differences in the other respiratory components. Therefore, it can be concluded that the knockdown of Par17 has an influence on the respiratory chain in HCT116 cells. The reduction of Par17 leads to increased oxygen consumption, caused by the respiratory chain. The effect could be observed in basal respiration, ATP-dependent respiration and in maximal respiration. Since an increase in OCR could also be noticed when the ATP synthase was inactivated, an effect on the respiratory chain on the complexes acting upstream of ATP synthase is possible.

To obtain an indication of whether the effect was triggered by protein regulation or gene regulation of the respiratory proteins, the amount of protein present in the cells was examined by western blot. A change in gene regulation often leads to a change in the amount of proteins. An antibody cocktail was used that contains antibodies for analyzing oxidative phosphorylation (OXPHOS) complexes. Three of the five complexes were detected in the western blot for the different cell lines, namely Complex II, Complex III and Complex IV (ATP synthase) (Fig. 20C). Actin was used as a loading control. The protein levels of the detected complexes were quite similar between the control cells and the knockdown cells. Thus, it can be concluded that for the detected complexes, gene regulation is likely similar in the cell lines studied.

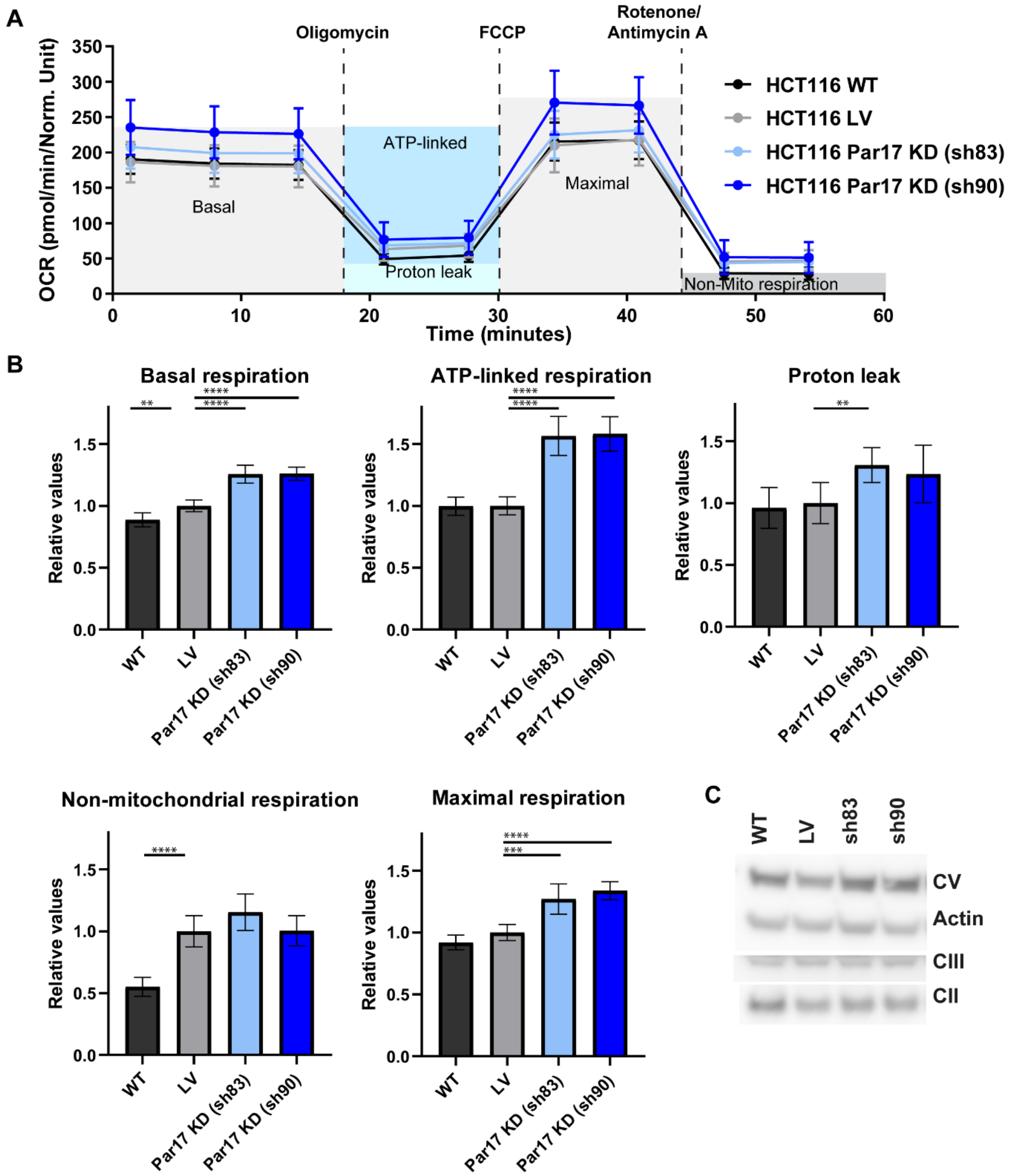

Figure 20: Assessing the mitochondrial function after Par17 knockdown. A: The Seahorse Cell Mito Stress Test was used to investigate the mitochondrial function. The oxygen consumption rate (OCR) of counted cells/well was measured and is presented in a flow chart. Results are presented as the mean ± CI (n=5). The experiments were performed using the XF24 extracellular flux analyzer. **B:** Three biological replicates of the experiment were performed with five technical replicates each (except for the WT cell line with which only two experiments were carried out) and the relative ratios with respect to the LV cell line were calculated and merged. The bar graphs of the basal respiration, the ATP-linked respiration, the proton leak, the non-mitochondrial respiration and the maximal respiration with the mean ± 95% CI are shown. **p< 0.01, ***p< 0.001, ****p<0.0001 vs. LV (two-sided t-test). **C:** Western blot analysis of OXPHOS complex subunits in the knockdown and control cell lines. UQCRC2 (complex III) and ATP5A (complex V), SDHB (CII) and actin as control were targeted.

4 Discussion

4.1 Proximity and impact of Par17's N-terminus on its catalytic PPIase domain

In order to investigate differences between Par17 with and its shorter isoform Par14 the structural elements of both parvulins were first compared. In this work, the $^{1}H^{15}N$-HSQC spectra of the full-length protein were recorded under the exact same conditions and were compared to the spectra of the isolated PPIase domain. The comparison revealed changes in the chemical shifts due to the presence of the different N-termini. Most of the chemical changes were likely caused by the position of the charged N-terminus, because the chemical shift changes of isolated PPIase domain and the truncated form of Par14 (Par14$_{\Delta 1\text{-}22}$) and the chemical shift changes of Par14 relative to the isolated PPIase domain were almost identical. In contrast, the additional N-terminal 25 amino acids of Par17 resulted in weak but additional changes in the chemical shifts of resonances within the catalytic domain. This could indicate binding of the N-terminus to the PPIase domain. Interaction of a flexible N-terminus lacking any secondary structure elements with its PPIase domain could also be observed for other PPIase, such as the human FKBP38 [56] and FKBP42 from Arabidopsis thaliana [13].

The 25 N-terminal amino acids in Par17 also influence residues that were stated to be important for catalysis, such as Val^{116}, Phe^{119} and Phe^{145} [90]. This observation is in agreement with the identification of minor chemical shift changes found in resonances of Lys^{100}-Ala^{125} when comparing the HSQC-spectra of Par14 and Par17 found by Burgardt and coworkers [14]. However, the cited experiment was performed under different environmental conditions. In a similar manner, this work has also observed structural changes in the first α-helix of Par17's PPIase domain that affected the amino acids His^{73}, Gly^{74} and Ile^{76}. Moreover, the additional N-terminal 25 amino acids of Par17 resulted in some minor chemical shift changes in the resonances of the residues of Par17 that are also part of the N-terminus in Par14. This may point towards structural differences within these elements in both isoforms.

Amino acids like Lys^{8} and Gly^{9} as well as Phe^{17} of Par17 were suggested to participate in an interface between the PPIase domain and the N-terminus, but no long-range NOE signals could be found which confirm such an interaction [14]. Thus, a putative interaction might be weak and transient. In order to detect a possible transient binding, cross-linkers were used, which covalently fixes such interactions and thus make them detectable by mass spectrometry [3, 72]. DSSO which links lysine residues to each other [57] and the photo-reactive amino acids photo-methionine and photo-leucine [101, 136] were used as cross-linkers. An estimation of residue distance from the cross-linking experiment suggested that the N-terminus might be closer to the PPIase domain than shown in an I-TASSER model calculated without cross-links constrains. The data of the cross-linkers and the chemical shift changes between the full-length protein and the isolated PPIase domain were combined by labeling the affected residues on the protein surface. Areas that showed impaired residues in both experiments were determined to be possible interaction patches. One binding patch for the N-terminus of Par14 was identified in front of the catalytic cleft of the PPIase domain. This binding epitope could also be identified in Par17. In Par17, the same part of the N-terminus was linked to approximately the same region at the catalytic groove. In addition, the first few residues of the N-terminus of Par17 are connected by cross-links to the first α-helix of the PPIase domain. This is consistent with chemical shift changes observed in resonances assigned to this region in the HSQC spectrum of Par17 when compared to the HSCQ spectrum of Par14.

A structural model was calculated with the program YASARA [66] based on the Par17 structure derived by I-TASSER using the cross-links between the N-terminus and the PPIase domain as restraints. An energy minimization of the structure was performed with this information (Section 2.2.18). The model obtained shows that the interaction between Par17 and its N-terminus could shield the catalytic center (Fig 21). In addition, it indicates an interaction of the first α-helix of the PPIase domain with the initial residues of the N-terminus of Par17. Binding of the N-terminus to the long, deep, curved groove that is surrounded by the side chains of Lys^{133}, Val^{135}, Pro^{127}, Ala^{125} and Glu^{121} on the one side and Lys^{84}, Asp^{138} and Pro^{139} on the other, as suggested by Matena et al. in 2018 for the N-terminus of Par14, could not be observed [84].

For the PPIase FKBP38 and part of its N-terminal domain, a weak interaction was also demonstrated [56]. By solvent paramagnetic relaxation enhancement was demonstrated that the interaction did not protect the interaction surface. In analogue to the observations made in this study, a weak interaction of the catalytic and part of its N-terminal domain was also demonstrated for FKBP38 [56]. Here, chemical shift changes were observed in the presence of the N-terminus in the core domain and close to the putative isomerase active center of FKBP38. For FKBP38 the presence of part of the N-terminus resulted in inactivation of the PPIase domain, most likely caused by their interaction. Whether the N-terminus of Par17 influences the function of the catalytic PPIase domain in a similar way was further explored in this work.

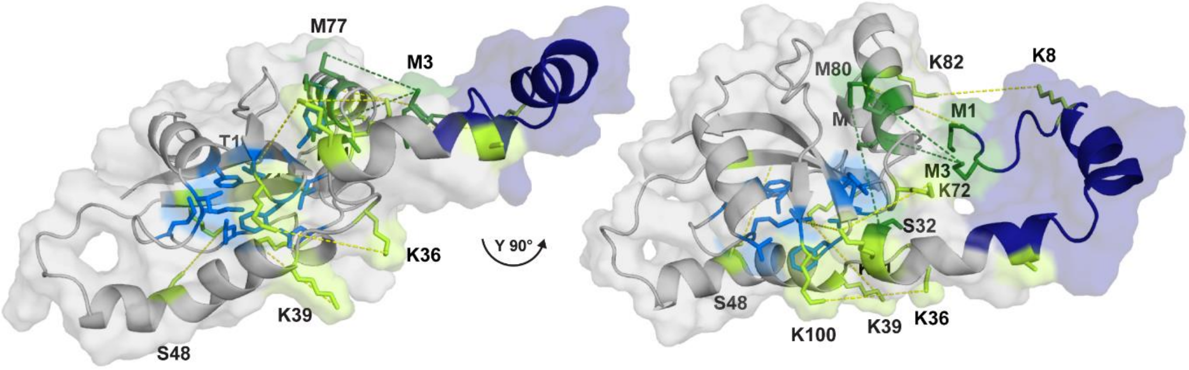

Figure 21: Model of the interdomain contact of Par17. The model was calculated by YASARA on the basis of the Par17 I-TASSER model used in this work. As distance restraints the identified cross-links were used. The identified photo-reactive cross-links (dark green) and the DSSO cross-links (lime yellow) between the PPIase domain and the N-terminus are connected and labeled. Amino acids involved in the catalytic process (marine blue) and the 25 N-terminal amino acids of Par17 (dark blue) are highlighted.

4.2 The 25 N-terminal amino acids in Par17 cause a higher substrate specificity by binding the model substrate

To test the effects of the 25 N-terminal residues in Par17 on the catalytic efficiency and substrate specificity, Par17 were investigated *in vitro*. The catalytic efficiency was compared to the one of Par14 and the isolated PPIase domain. For its determination, a well-established protease coupled PPIase assay introduced in 1984 [30] with some improvements [63] was used.

The applicability of the assay for the parvulins was investigated in this work in a two-step process. First, at a constant substrate concentration of a model substrate in which Ser preceded proline the direct proportionality of the rate constant and the Par17 concentration (2 µM to 10 µM) was demonstrated. A similar linearity was also obtained within experiments performed in presence of either Par14 or the isolated PPIase domain when using peptides in which Ser, His or Arg were preceding proline [54].

Second, the K_M value had to exceed the *cis*-substrate concentration used in the experimental setting to ensure a pseudo first order condition under which first order rate constant can be determined by exponential fitting [43]. The K_M was to be exemplarily determined for the enzymes in presence of a model substrate. For many other members of the PPIase family this condition holds as they have a high efficiency and high K_M values and the used substrate concentration ranged from nM to the low µM [52, 62, 76]. For the human FKBP12, for example, a K_M value of 500 µM for the model substrate Suc-Ala-Leu-Pro-Phe-pNa was shown [22]. For the human cyclophilin a K_M of about 870 µM for the model substrate Suc-Ala-Ala-Pro-Phe-pNa was revealed [63]. However, for the very inefficient non-phosphate specific human parvulins, it could be a limiting factor for the application of the assay. The K_M value was determined to be about 120 µM and the k_{cat} value was approximately 0.3 s^{-1} for Par14 using two different evaluation methods. The K_M values of Par17 and the isolated PPIase domain were demonstrated to be in the same range [8]. At 120 µM, the K_M was about a factor of 2- to 16-fold greater than the amount of substrate peptide used (total substrate 75 µM but the *cis*-portion was lower, see table A4 for exact content). Although the difference is not quite as great as with other PPIase, the applicability of the assay for Par14 and Par17 is possible, especially when measurements are compared under the same conditions as done in this work. Interestingly, for the efficient phosphate specific parvulin Pin1, the K_M value was determined to be 120 µM for the unphosphorylated substrate peptide Ala-Glu-Pro-Phe, too [146]. This is an indication of a similar binding strength but a difference in the k_{cat} of Par14 and Par17 compared to Pin1 [6].

Moreover, the applicability of the assay for the parvulins is also confirmed by its reproducibility. At least for Par14, there are already a few comparative k_{cat}/K_M values that were determined using the protease-coupled assay. The first attempt was made in 1999 by Uchida et al. [145], where the enzyme efficiency was measured for seven substrate peptides under slightly different conditions than in this work (35 mM HEPES buffer, pH 7.8, exact substrate concentration is not indicated, substrate diluted in dimethyl sulfoxide). Despite this, Uchida and coworker showed a low efficiency of Par14, around $0.1 \cdot 10^3$ - $4 \cdot 10^3$ $M^{-1}s^{-1}$ [145]. This corresponds to the values found in this work with a range of efficiency from $0.2 \cdot 10^3$ - $6.4 \cdot 10^3$ $M^{-1}s^{-1}$. In addition, Uchida et al. also showed a slightly more efficient conversion when the positively charged Arg was preceding proline (Table 15) [145].

The substrate specificity of Par14 has also been investigated using a protease free assay by Zoldák and coworkers [167]. In this assay, the N-terminus of the model substrate is additionally labeled with a 2-aminobenzoyl (Abz) group. In the *cis* conformation, the signal of Abz in the peptide is quenched. In the *trans* conformation emission can be detected at 416 nm after excitation at 316 nm. The catalytic efficiency can then be determined from the thermic and observed isomerization as in the protease-coupled assay. The catalytic efficiency of Par14 determined by Zoldák et al. with the protease-free assay ranged from $0.1 \cdot 10^3$ - $5.9 \cdot 10^3$ $M^{-1}s^{-1}$ [167]. With these values, the catalytic efficiency determined with the protease-free assay were similar to those determined in this work. Yet, the ranking for the efficiency of the model substrates with varying amino acids at the Xaa-Pro position slightly differs from the one found in this work (Table 15). This may either be due to the high standard deviation of the measurements in this work resulting in not yet accurate enough mean values or the results are affected by the different tags (Abz/pNa) used in the described experiments.

In this work, the efficiency of Par14 for the best converted substrate peptide did not even differ by a factor of ten from the efficiency of most of the other peptides. Nevertheless, in case of Par14 the same pattern of substrate conversion efficiency was observed in all three experimental setups [145, 167]. Par14 shows one of the highest preference for the positively charged amino acids Arg and Lys preceding proline in all three experiments. However, for the amino acid His, which is very bulky and can be partially positively charged under certain conditions at the physiological pH, Par14 shows one of the worst efficiencies in all three trials. Likewise, the efficiency seems to be very low for negatively charged amino acids (Glu, Asp) preceding proline, in the experiments that includes the respective substrate peptides [167].

Moreover, it was shown that Par17 was only efficient for substrate peptides in which Arg or Lys were preceding proline. A low efficiency could be observed for the His at position Xaa, just as for Leu and Gln. For the other substrate peptides, hardly any efficiency was found. The substrate specificity for positive amino acids preceding proline already indicated in Par14 is further increased by the additional 25 N-terminal amino acids of Par17. Such a strong substrate specificity for positive amino acids was also demonstrated for other non-phosphate specific parvulins such as TcPar14, TcPar45, BsPrsA and NmPinA (Table 15) [26, 46, 48]. The PPIase domain of TcPar45 for example was 4-20 times more efficient for the substrate peptide with Arg preceding proline than for the other peptides measured in the experiment by Erben and coworkers [26]. Among the non-phosphate specific parvulins there are also parvulins that are slightly more efficient for Leu at the Xaa position such as Par10, CdPrsA2 and LjPar2 [64, 104, 149]. For these parvulins, the additional charge is not necessarily beneficial for catalysis. In addition, there is also one non-phosphate specific parvulin SaPrsA that was most efficient when Glu with a negative charge was preceding proline [46]. Despite some differences, the substrate specificity of Par17 for positively charged amino acids preceding proline further supports the hypothesis that the non-phosphate specific parvulins may have an evolutionarily conserved substrate spectrum [84]. This substrate spectrum is even more constricted in Par17, a protein unique to *Hominidae*.

Table 15: Specificity of non-phosphate specific parvulins. The parvulins are ordered by the similarity of their substrate specificity to that of Par17.

Protein name	Species	Branch	Substrate specificity	Assay	Reference
Par17	H. sapiens	Human	Arg>Lys>Leu>Gln>His> Ala, Ser, Phe, Val, Gly, Tyr, Asn, Ile, Thr, Glu, Trp, Asp	Protease-coupled	This work
Par14	H. sapiens	Human	Arg>Leu>Gln>Ala>Lys>Phe, His	Protease-coupled	Uchida 1999 [145]
			Arg>Lys>Ser>Thr>Leu>Phe>Met>Cys>Ile> Asp, Ala, Tyr>Val>Trp>Gln>Gly> Pro, Glu, Asn, His	Protease-free	Zoldak 2009 [167]
			Ala, Arg, Gln, Lys > Val, Gly, Tyr, Ser, Leu, Phe, Glu > Thr, Asn, Trp, Ile, His, Asp	Protease-coupled	This work
Par14	T. cruzei	Trypanosoma	Arg>>Leu> Ala, Glu, Phe	Protease-free	Erben 2010 [26]
Par45	T. cruzei	Trypanosoma	Arg>Leu> Glu, Ala, Phe	Protease-free	Erben 2010 [26]
PinA	N. maritimus	Archea	Arg>Leu>Ala>Phe>Ser	Protease-coupled	Hoppstock 2016 [48]
PrsA	B. subtilis	Bacteria	Lys>Glu>Ala>Asn, pSer, pThr	Protease-coupled	Heikkinen 2009 [46]
PinA	C. symbiosum	Archea	Leu>Arg>Ala>Phe>Ser	Protease-coupled	Hoppstock 2016 [48]
Par2	L. japonicus	Archaeplastida	Leu>Ala>Arg>>Glu	Protease-coupled	Kouri 2009 [64]
Par3	L. japonicus	Archaeplastida	Leu>Ala>Arg>>Glu	Protease-coupled	Kouri 2009 [64]
PrsA2	C. difficile	Bacteria	Leu>Arg>Met>Lys>Gln>Phe>Ala>Trp>Tyr>Ile, Glu, Val	Protease-free	Ünal 2018 [149]
Par10	E. coli	Bacteria	Leu>Phe>Ala>Trp>Ile>His>Val>Lys>Glu>Gly	Protease-coupled	Rahfeld 1994 [104]
PrsA	S. aureus	Bacteria	Glu>Ala>Lys>Asn, pSer ,pThr	Protease-coupled	Heikkinen 2009 [46]

Since Par17 showed a stronger substrate selectivity than its shorter isoform, the differences in binding of the substrate peptides between Par17 and the catalytic PPIase domain were investigated by NMR. Changes in resonances of residues of Par17 and the isolated PPIase domain were measured after addition of the substrate peptide with a positively or a negatively charged amino acid preceding proline. Upon addition of the substrates (Lys-Pro, Glu-Pro), the chemical shift changes in resonances assigned to NH residues in the catalytic domain were comparable for both, the isolated PPIase domain and Par17. In general, binding of the peptide exhibiting a negatively charged Glu preceding proline had a stronger effect on the chemical environment of Par17 and the isolated PPIase domain than the substrate with the positively charged Lys preceding proline. In addition to a higher number of chemical shift changes and stronger chemical shift changes, binding of Par17 to the peptide with Glu at the Xaa position appears to be stronger than binding to the Lys peptide, suggested by slightly different microscopic dissociation constants.

Strong chemical shifts are found upon addition of each substrate peptides (Lys-Pro, Glu-Pro) for resonances of residues positioned along the active center of Par17 (Fig. 22). A similar observation has been made upon addition of oxidized DTT to the PPIase domain of Par14 [90, 115]. Resonances of amino acids that showed the greatest chemical shift changes after addition of either substrate peptides were Gly^{113}, Met^{115}, Val^{116}, Gly^{117}, Phe^{119} and Gln^{120}. Val^{116} and Phe^{119} are involved in the catalysis [90]. The corresponding residues to Phe^{119} and Leu^{107} (Phe^{134} and Leu^{122}) were found to participate in hydrophobic interactions within Pin1 when complexed to the proline-mimic moiety of an inhibitor [165], suggesting a stabilizing function of the proline of the substrate for Phe^{119} and Leu^{107} in the Par17-substarte complex. The amino acids around Gln^{120} may contribute to the interaction of the *trans* form as the *trans*-mimic inhibitor occupies [165] the region around Gln^{120} (Glu^{135}), Gly^{113} (Gly^{128}) and Met^{115} (Met^{130}) in Pin1. With the substrate peptide that had Glu at the Xaa position, the additional amino acids Phe^{89}, Ala^{101}, Arg^{112}, Ala^{122}, Ala^{123}, Ala^{141} were affected, which are mainly distributed around the catalytic center.

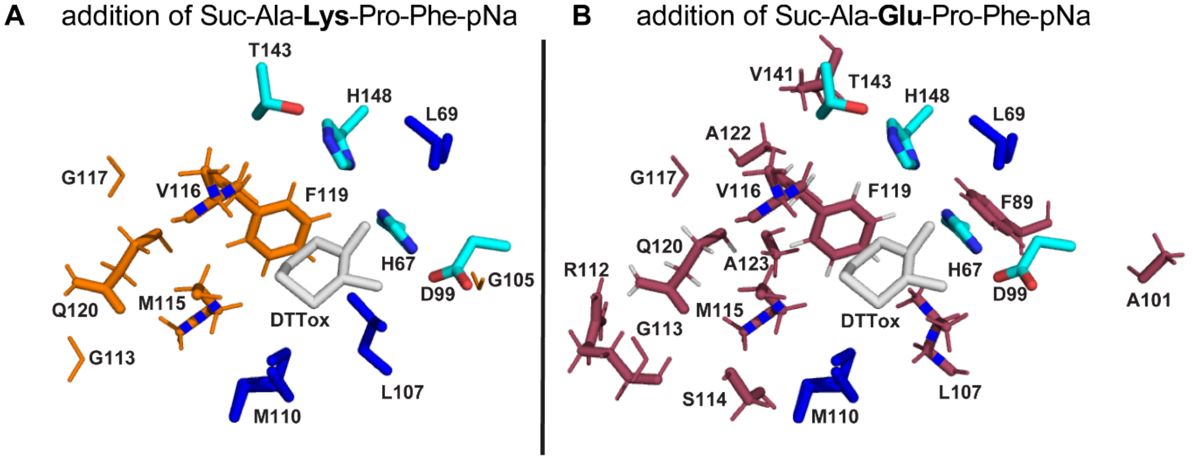

A addition of Suc-Ala-**Lys**-Pro-Phe-pNa **B** addition of Suc-Ala-**Glu**-Pro-Phe-pNa

Figure 22: The active center of the PPIase domain occupied by DTT is demonstrated with highlighted amino acids whose resonances undergo chemical shift changes upon substrate peptide addition. The active center of the PPIase domain in complex with DTT is shown (PDB-ID: 3UI6). The amino acid side chains that are important for the catalysis (blue) and are part of the hydrogen bond network (cyan) are shown (lit Müller 2013). The resonances of amino acids that shifted strongly (exceed the overall mean chemical shift changes) upon addition of the substrates (**A:** orang Xaa=Lys, **B:** red berry Xaa=Glu) are presented.

The most notable difference between the addition of the Glu-Pro and the Lys-Pro peptide to Par17 is that the negatively charged peptide (Glu-Pro) triggers shift changes of resonances resending in the N-terminal part of Par17 (discontinuously between residue Ala^{4} and Met^{26}), while the positively charged peptide (Lys-Pro) does not. The N-terminal 25 amino acids of Par17 may be correlated to the increased substrate specificity of Par17 by binding the model substrate peptides. To strengthen this hypothesis, the binding of substrate peptides in which Val or Gly were at the Xaa position was analyzed. For both substrates, Par17 also showed low catalytic efficiency. Chemical shift changes in the N-terminus of Par17 (discontinuously between residues Val^{11} and Lys^{25}) were also observed after addition of the two substrates (Val-Pro, Gly-Pro), however the chemical shift changes for the same resonances was less intense than for the Glu-Xaa substrate. Whether binding of the N-terminus to the peptides also occurs independently of the PPIase domain was investigated by adding the Glu-Xaa substrate peptide to the isolated N-terminus of Par 17 (Par17$_{\Delta 61\text{-}156}$). The binding pattern for the Glu-Xaa substrate peptide was approximately the same as for the N-terminus of the full-length protein. In addition, the positively charged peptide (Lys-Pro) was added to the isolated N-terminus. This did not result in any chemical shift changes. Thus, the N-terminus binds the inefficiently catalyzed substrate peptide (Glu-Pro) also separately from the PPIase domain. Taken together, the results strengthen the suggestion that the N-terminal 25 amino acids of Par17 are related to the increased substrate specificity of Par17 through binding of the model substrate peptides.

Pin1 is a close relative of Par17. The N-terminus of Pin1 is about the same length as the N-terminus of Par17, but it has structured parts (residue 1-39, WW-domain) that can bind pSer/pThr-Pro motifs [106, 114]. A transient interaction of both domains of Pin1 was demonstrated [9]. In analogy to Par17 no NOEs could be detected in NOESY-like NMR spectra, which could allow to define the interdomain interface [85]. Therefore, the weak and transient binding was further investigated by analyzing the contact of both domains upon monitoring the chemical exchange of open and closed domain conformations or with paramagnetic relaxation enhancement (PRE). Both experiments revealed that the transient domain interaction in Pin1 facilitates ligand binding (PEG400) to the WW domain [85]. For Pin1, the binding of a ligand (Cdc25) to the WW domain results in an increased inter-domain separation [164]. This separation results in altered *cis*/*trans* isomerization of the PPIase domain [157]. A similar relationship between substrate binding and catalysis may apply for the N-terminus of Par17 and its catalytic domain. However, the exact mechanism awaits more detailed investigation.

4.3 Par17 interacts with target proteins involved in various cellular events

The discovered difference in substrate specificity of Par14 and Par17 in conjunction with the different localization of the two isoforms suggests different interaction partners and involvement in different metabolic pathways of the proteins. In this work, photo-crosslinking and mass spectrometry led to the identification of new interaction partners of Par14 and Par17 as well as to the confirmation of already known interaction partners. Thereby the standard application, in which photo-reactive amino acids were added to the cell medium and incorporated into all proteins to identify interaction partners in living cells [44] was modified. The photo-reactive cross-linkers were incorporated directly into the full-length parvulins and were then added to the cell lysate. This new application used for the full-length proteins within this work has the advantage that only the interaction partners that bind to parvulins are cross-linked. In addition, by adding the isolated N-termini to labeled cell lysate, the involvement in binding of these subunits can be studied. Detrimentally, the application enforces the loss of integrity of cellular compartments, since cell lysate was used. It is therefore astonishing that beside this adverse condition only few interaction partners could be found that bind both parvulin isoforms. Between Par14 and Par17, only 8 common interactors out of a total of 172 binding proteins could be detected, and for the two isolated N-termini, only 32 out of a total of 124 proteins. This demonstrates that the interaction partners of Par14 and Par17 discriminate with relative high selectivity between the two isoforms, despite the high sequence identity of both enzymes.

Structurally, Par17 is hardly different from Par14 with almost the identical structure of the PPIase domain, except that it exhibits 25 additional N-terminal amino acids. This has hampered discrimination of the two isoforms in previous studies and putative functional differences were neglected. To narrow down the individual functional features of Par14 and Par17, the interaction partners found in this work were classified in categories. The confirmed or suggested new functions of the parvulins indicated by these categories were depicted graphically (Fig. 23). For Par14, the largest category of binders is made up of ribosomal proteins, with 77 members found [37]. Also, for the isolated N-terminus of Par14 more than half of the identified proteins were grouped into the category of proteins related to RNP-complexes. This is consistent with the previously described association of Par14 with the RNP-complex and its function as an rRNA processing factor [33, 34]. The two other groups of proteins that were classified by the categorization of the Par14 binders and interactors of Par14’s N-terminus are RNA- or DNA-associated processes. These processes mainly take place in the nucleus and the nucleoli, agreeing with Par14’s primary location [34, 137] The identified interactors for Par14 or Par14’s N-terminus in these groups contain overlapping proteins (XRCC6, DHX9, HIST1H1B, HIST1H1E, NSUN2) and similar proteins of the same protein family, such as the different heterogeneous nuclear ribonucleoproteins (HNRPS). The identified HNRPS are either part of the spliceosome or associated with it [55]. In addition, other proteins relevant to splicing (ALREF, SF3B2, SRPK1) were identified. Together, this point to a function of Par14 in splicing. In addition, for Par14 and the Par14 N-terminus four common binding proteins were identified that are involved in chromatin remodeling and DNA repair. This is consistent with the ability of Par14 to bind DNA with high affinity and its association with chromatin [120, 137]. In general, the work indicated a more general role of Par14 in DNA- and

RNA- associated processes in addition to the maturation of the ribosome. In addition, the suitability of the method for finding real interaction partners is supported by the fact that the interaction partners of Par14 found were approximately 50% consistent with a study that determined the interaction partners of Par14 only from the nuclear extract [34]. Furthermore, new interaction partners were found that had not yet been identified elsewhere [32–34, 45, 59, 69, 109, 116, 133, 134, 150, 153].

For Par17 and its isolated N-terminus, the interaction partners could be divided into five functional categories. The confirmed or suggested new functions of Par17 indicated by these categories were depicted graphically (Fig. 23). In detail, a so far unattended function of Par17 is related to cellular transport. Proteins involved in cellular transport events are highly represented and found as interactors of both the full-length protein and Par17's N-terminus. Proteins involved in different transport processes have been determined such as between the ER and Golgi, into the cell nucleus and into the mitochondrion. This correlated with the fact that Par17 is transported into the inner membrane of the mitochondrion [50]. Notably, most Par17 N-terminal binders belong to the category of internal cell motility. Four proteins (TUBA4A, TUBB4B, TUBB6, ACTB) were confirmed as putative interaction partners by both interaction studies for Par17's N-terminus and the full-length protein. This finding matches with the ability of Par17 to activate tubulin polymerization in a calmodulin dependent way in vitro [14, 142]. As Par17 is translocated into the inner membrane of the mitochondrion [89] one expects to find binding partners within this cellular compartment. Indeed, the interaction studies of the full-length protein complemented by data obtained on interaction studies of the N-terminus suggest a role of Par17 in energy conversion. On the one hand, Par17 seems to be involved in oxidative phosphorylation (Par17-fl: COX2, COX20, CY1, NDUFA5, NDUFS8; Par17 N-term: UQCRC2, ATP1A1, ATP5A1, ATP5B, ATP5C1, ATP5J2). On the other hand, it seems to take part in lipid metabolism (ACSL3, PDHB, DPM, CTPS1), such as in β-oxidation (HADHB, HADHB). Finally, some interactors of its N-terminus indicate a function of Par17 in amino acid metabolism. However, this finding should be treated with care, as there are no representatives of such binders found in the cross-linking experiments carried out with the full-length protein.

In summary, the categories into which the identified interaction partners are classified give a first insight into processes both parvulins are potentially involved in. Nevertheless, classification into categories also entails a certain degree of inaccuracy. The identification of proteins by mass spectrometry always carries the probability of finding false positive interaction partners. Therefore, additional methods should be used to confirm individual identified interaction partners [37].

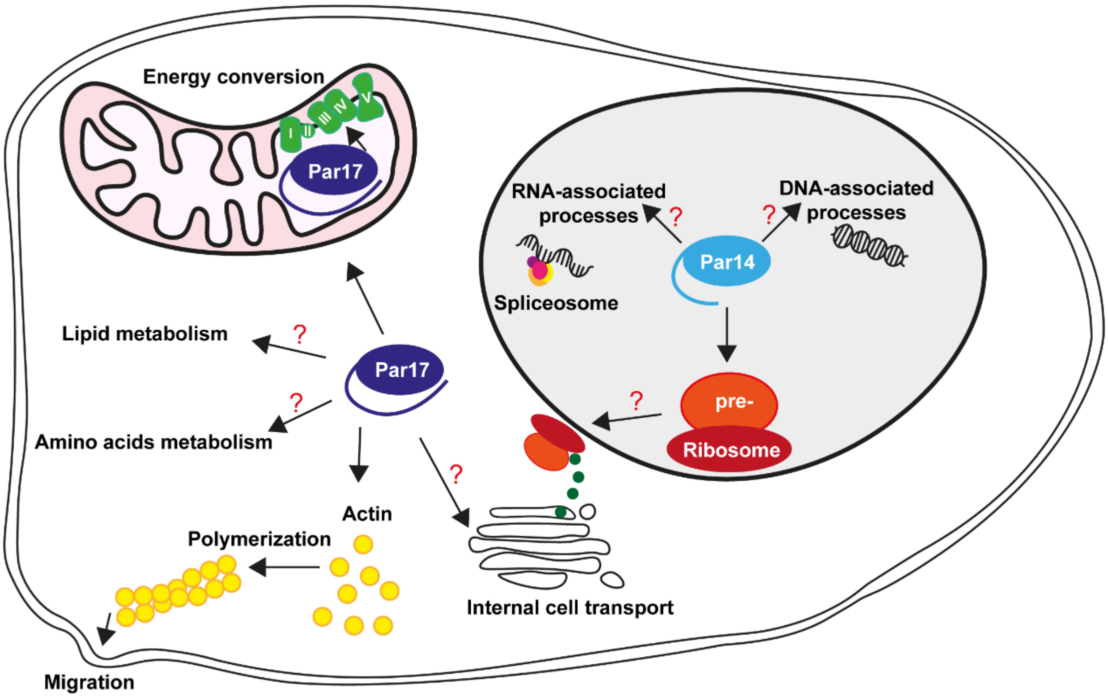

Figure 23: Graphical representation of the indicated cellular roles of Par14 and Par17. The scheme represents the functions of Par14 (light blue) and Par17 (dark blue), which were suggested in this work by the categorization of the interactors identified by mass spectrometry. Cytoplasm (white) and nucleoplasm (grey) and mitochondrion (pink) are colored.

4.4 Narrowing down the functional role of Par17 within the cell

As mentioned, an interaction of Par17 with tubulin was reported [14, 142]. Besides tubulin, actin is another major component of cytoskeleton and it is also a driving force cellular motion [113]. Actin was found in this study as an interaction partner of Par17. Therefore, it is interesting to further investigate the putative interaction of both proteins. First, the interaction of Par17 with actin was studied and compared with that of Par14. Par17 efficiently bound actin, which is going to polymerize in the presence of the enzyme in a concentration-dependent manner. Interestingly, the shorter isoform Par14 was even slightly more efficient within this process, although it binds actin more poorly and actin was not enriched as an interacting partner in cross-linking experiments using

Par14 as bait. These properties suggest that Par14 initiates actin polymerization well in vitro, since it possesses the same PPIase domain as Par17, but is less involved in this process within the cell due to its more nuclear localization and poorer binding [37]. Following up, the binding of Par17 to actin was studied in more detail using NMR. Upon titration of actin to isotopically labelled Par17 chemical shift intensity changes occurred mainly for resonances of residues located within the N-terminus of Par17. However, some amino acids of the PPIase domain were also affected by actin. Interestingly, calmodulin was also shown to bind the first 25 amino acids of the N-terminus of Par17, and thus completely blocks the polymerization of tubulin [14]. The binding of the same segment by both Par17 interactors (actin and calmodulin) suggest that actin polymerization triggered by Par17 also could be affected by calmodulin. However, this has been not further explored within this work.

In order to identify the target region of Par17 in actin a spotter array displaying a 12-meric overlapping peptide scan of actin was used and incubated with Atto-labeled Par17. Ten segments were identified as possible target regions. Seven of these segments had an Xaa-Pro motif with varying amino acids at the Xaa position. For comparison, in tubulin a binding segment which contained the Xaa-Pro motif with Arg86-Pro87-Asp88 was found as a potential binding motif [14]. In this work, DSSO cross-linking was used to confirm four Par17 binding segments within actin. With all this information, a possible interaction model of actin and Par17 was calculated (Fig. 24) to further discuss this interaction. For this approach the program High Ambiguity Driven protein-protein DOCKing (HADDOCK) was used [151]. For Par17 the amino acids affected in the NMR studies upon addition of actin were set as ambiguous interaction restrains. For actin, the amino acids that were identified by the spotter array as putative interacting segments and that were additionally exposed to the surface were set as ambiguous interaction restraints. In parallel, the respective cross-link sites between Par17 and actin were set as unambiguous distance restrains. The resulting model of the complex gives a first impression of what the interaction between Par17 and actin, which is made up by four subunits [23] could look like (Fig. 24). The binding site of Par17 appears to be at the interdomain interface of all four subunits of actin.

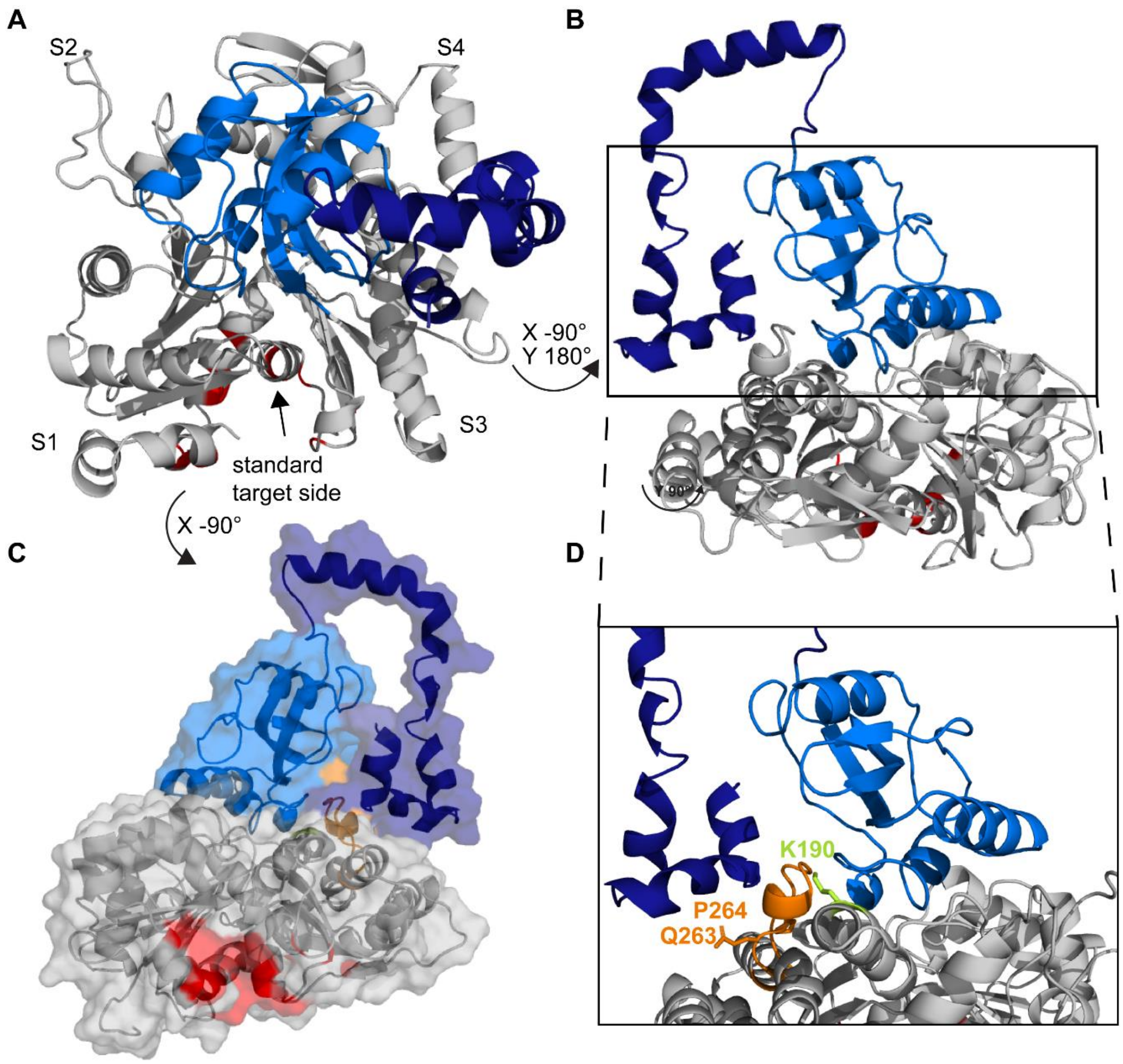

Figure 24: Protein-protein complex model of Par17 and β-actin. The interaction model between β-actin (PDB-ID: 6ANU, gray) and Par17 (PPIase domain: light blue, N-terminus: dark blue) is depicted from different angles. The model was calculated by HADDOCK based on the presented experimental data. Energy minimization was performed with YASARA. **A:** The interaction model is shown from the top and the subunits of actin and the standard binding side are labeled. **B:** The interaction model depicted from the side and **C:** with the protein surface. **D:** In the magnification of a part of the model the loop of actin that is enclosed by the N-terminus and the PPIase domain of Par17 is highlighted (orange).

Interestingly, the computationally determined binding site is not the standard binding site of actin to which many actin-binding proteins are attached. The standard binding site of proteins is a hydrophobic cleft between subdomain 1 and 3 (highlighted in the structure of Fig. 24A) [23, 99]. Although, the spotter experiment showed that Par17 can also bind to the sequence of an α-helix in the standard actin-target side including the actin residues Tyr^{143}, Ala^{144} and Gly^{146} [23], cross-links in this region could not be detected. Most of the cross-links were found for the amino acid Lys^{190} in actin. This residue is localized at the interface of the four subunits of actin.

Actin binding proteins that exhibit a long and flexible N-terminus such as thymosin-B4 [51], tropomodulin [107] or the β-III-spectrin actin binding domain [154] often wrap this structural element along actin regions without covering a recognizable binding motif or pattern. In the calculated HADDOCK model of the Par17 and actin complex, this does not seem to be the case for Par17's N-terminus (Fig. 24B, C). In the calculated model a loop element of actin (Gln^{263}-Gly^{273}) resides between the binding side of Par17's N-terminus and the PPIase domain (Fig. 24D). A Gln-Pro motif is found at the beginning of this loop, which might be a putative target site for *cis*/*trans* isomerization by Par17. Nevertheless, the model is only a first impression. More specific and informative experiments need to be performed to confirm and narrow down the actin binding site of Par17 in more detail. The high number of available binding sites revealed by the spotter array experiment may negatively influence the calculation of the docking complex experiment which is reflected in the number of violations of the restraints, where 77% of the cross-links are not in the constrained distance range.

A further investigation of the polymerization of actin by Par17 revealed that the PPIase domain without the N-terminus is not able to facilitate polymerization, but that Par17 needs an intact catalytic domain for efficient polymerization. Interestingly, the knockdown of Par17 in cells has a pronounced negative effect on cell motility. However, it is still unclear how exactly the polymerization of actin and tubulin triggered by Par17 affects the migration of the cell. Furthermore, it is unclear under which conditions parvulins are involved in this process. Since polymerization of actin by Par17 within the cell has not yet been described, the protein may play a role in certain processes, such as in cell division or stress response [37].

A function of Par17 in energy conversion, specifically in the oxidative phosphorylation, was suggested from the cross-link studies. To investigate this mechanism in more detail, a Mito Stress Test was performed in which the effect on different subunits of the respiratory chain can be studied. A Par17 knockdown in cells results in an increased oxygen consumption rate (OCR) under basal conditions. Since there is no significant difference in non-mitochondrial respiration, this argues for an increased oxidative phosphorylation. Inhibition of ATPase still resulted in increased oxygen conversion in the Par17 knockdown cells, indicating that the influence of Par17 in the respiratory chain occurs upstream of the ATPase. Interestingly, in the study by Frattini et al. in 2018 [32], an enhancing effect on the OCR by PIN4 that is stronger phosphorylated at Tyr^{122} by the mutation of F3-T3 was observed in F3–T3 human astrocytes. Unfortunately, it is not clear from the study which isoform was used and whether a discrimination was made between the isoforms. Nevertheless, the study supports the possibility of an effect of parvulins on the respiratory chain. In addition, the equally expressed amounts of respiratory chain proteins in all cell lines makes an altered gene regulation as a reason for the increased OCR unlikely. Otherwise, the respiratory proteins would have to be more abundant in the knockdown cells. Therefore, the equally amount of proteins in the different cell lines is an indication that the effect is triggered by protein regulation of Par17. Considering the interaction studies performed with Par17, some proteins involved in oxidative phosphorylation, upstream of the ATPase were found. These proteins include COX2, COX20, CY1, NDUFA5, NDUFS8. The results of the Mito Stress Test make them even more interesting target proteins for additional interaction studies.

Not much is known about the function of other PPIases in the mitochondrion. Mitochondrial cyclophilin D (CypD) is one of the PPIases with a function in the mitochondrion. In addition to its well-studied function in controlling the mitochondrial permeability transition pore, it also interacts with the ATPase and the electron transport chain complex I and complex III [100]. CypD overexpression results in an increased activity of complex III and interaction of both could be demonstrated, accompanied by an increased number and formation of supercomplexes. For CypD it was assumed that it regulates the mitochondrial mechanisms by increased formation of the respiratory chain that which leads to a more efficient electron transport [27]. Perhaps Par17 has a similar regulatory function in mitochondrial mechanisms except that, unlike CypD, it does not lead to an increase, but to a negative regulation as indicated by the Mito Stress Test.

4.5 Conclusion and future prospective

In summary, this work has shown that the N-terminal 25 amino acids of Par17 have a major impact on the function of the protein. First, the presumed interaction of the N-terminus with the PPIase domain was investigated in more detail. The N-terminus of Par17 seems to shelter the catalytic core and the end of the N-terminus resides close to the first α-helix of the PPIase domain. In this work, it was shown that the presence of the N-terminal 25 amino acids of Par17 lead to a higher substrate selectivity in the PPIase assay. Par17 was more efficient for peptides with positively charged amino acids preceding proline. It was also demonstrated that the inefficient catalyzed substrate peptides were bound next to the catalytic domain by the N-terminal 25 amino acids of the N-terminus of Par17. To investigate the effect in detail, and figure out if the weak transient interaction has in impact on Par17's activity paramagnetic relaxation enhancement could be used, as it was demonstrated in the case of the WW domain of Pin1 [17, 47, 85, 164]. If a paramagnetic label in the N-terminus results in paramagnetic relaxation enhancement in the PPIase domain, it could be further investigated whether changes occur in the interaction area due to the addition of substrate. Another interesting aspect is whether the model substrate peptide with a positively charged amino acid preceding proline is really the best binding partner for Par17's N-terminus. Alternatively, there could be a better peptide combination, possibly with a posttranslational modification such as the phosphorylation at serine or threonine in the recognition motif of the WW-domain. This could be an interesting feature related to the ability of Par17 to recognize its interaction partners, since the N-terminal 25 amino acids are also crucial for the import into the mitochondrion and binding of calmodulin [14, 61] and actin. For this purpose, a peptide screening with the N-terminus of Par17 could be suitable. A general attempted could be a peptide array target screening, where based on a database search likely peptides are synthesized as peptide arrays on a membrane and screened for binding [132, 158]. Moreover, the binding of Par17's N-terminus to the peptide sequences already identified as possible binding segments in the peptide spotter array with actin and Par17 could be investigated with fluorescence anisotropy [87].

Furthermore, the additional N-terminal 25 amino acids of Par17 lead to the identification of different interaction partners than for Par14. This identification allowed narrowing down the so far widely unexplored functions of Par17 in the cell. Possible areas in which Par17 plays a role include internal transport, internal cell motility, lipid metabolism, amino acid metabolism and oxidative phosphorylation. Gene knockdown experiments in cells confirmed an influence of Par17 in migration and oxidative phosphorylation. To study the role of Par17 in oxidative phosphorylation more closely, the indications from this work that Par17 probably has a regulatory function upstream of ATPase could be addressed. First, the association of Par17 to the interaction partners identified in the cross-linking experiments upstream of ATPase could be investigated by co-immunoprecipitation followed by western blot and immunostaining [73, 92]. In addition, the impact of Par17 on the activity of the identified individual complexes complex I and complex III could be determined using the knockdown cell lines [4, 81, 98, 162]. Further investigation of these all the mentioned aspects is important, as it has recently become apparent that Par17 and Par14 may have an overlooked role in cancer [32, 155] and viral infections [118].

5 Appendix

5.1 Appendix figures

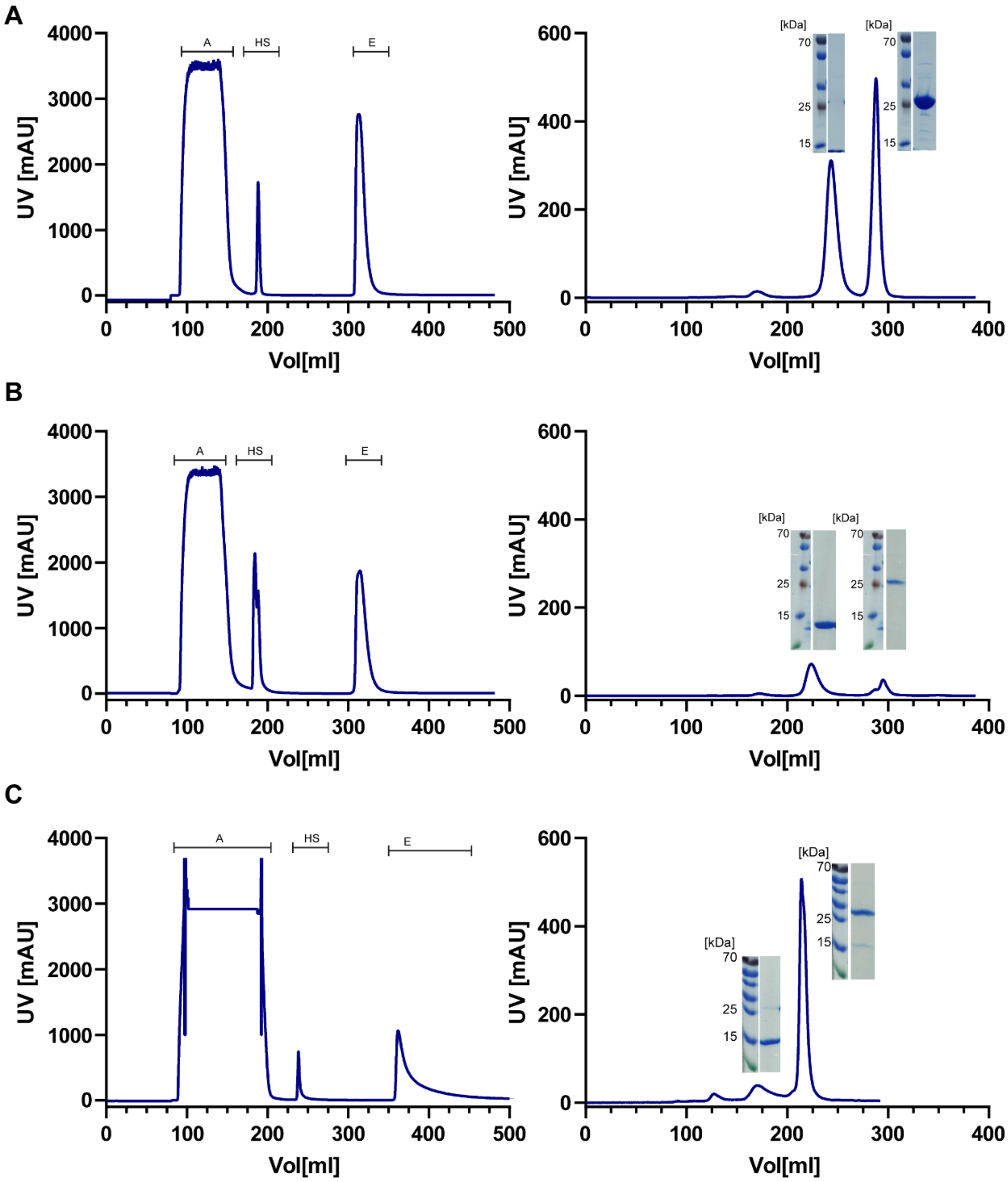

Appendix figure 1: Chromatogram and SDS-gels from the purification of the ^{15}N-labeled proteins. The GST-tagged proteins were expressed in *E.coli* and purified by affinity chromatography (right chromatogram). The GST-tag was cleaved off by PreScission protease and the target protein was separated by gel size exclusion chromatography (SEC, left chromatogram). Fractions of SEC were applied to a SDS gel. Purification of A: the isolated catalytic PPIase domain, B: Par14 and C: Par17.

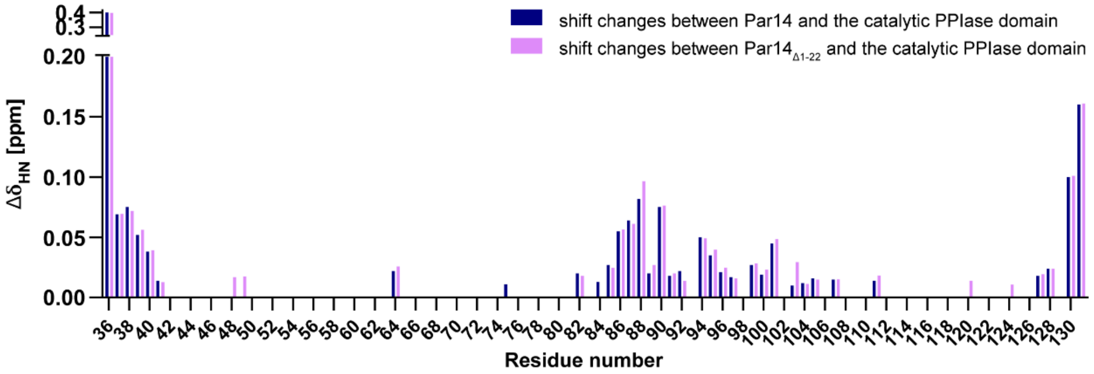

Appendix figure 2: Chemical shift changes of Par14 and Par14$_{\Delta 1\text{-}22}$ in comparison to the isolated catalytic PPIase domain. The calculated combined chemical shift changes from the 1H15N-HSQC spectra for shifting residues of Par14 (blue) and Par14$_{\Delta 1\text{-}22}$(purple) in comparison to the catalytic PPIase domain are plotted against the residue number of Par14.

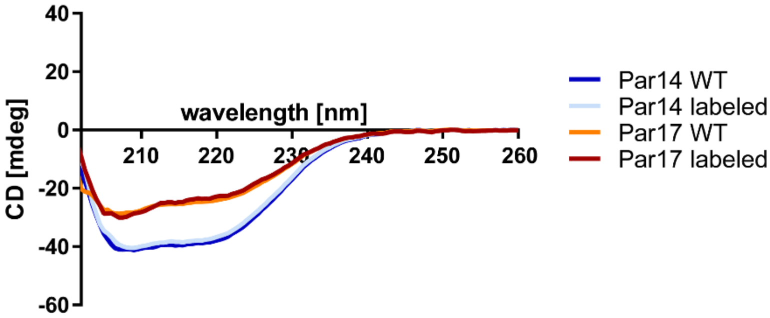

Appendix figure 3: CD spectra of WT parvulins compared to photo-reactive amino acid labeled parvulins. The proteins were measured at 25 °C in their native buffer (50mM HEPES, 150 mM NaCl) diluted with 50 mM KPi buffer to a concentration of 25 µM. CD spectra were measured from 190 to 260 nm. The wavelengths between 190 nm and 202 nm were omitted because the salt in the buffer influenced the measured values in this region. Each spectrum was recorded with 25 scans. For comparison, the intensity of Par14 WT was multiplied by a factor of 1.19 and that of Par17 labeled by 1.5. The shape of the curves of the labeled proteins and the native proteins were quite similar.

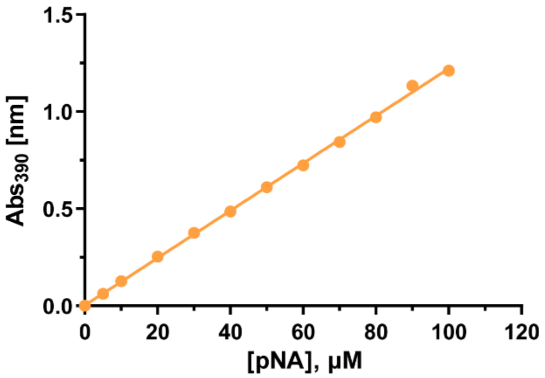

Appendix figure 4: Absorption of free para-Nitroaniline at 390 nm at different concentrations. Measurements were carried at 10 °C. Data points were fitted linearly and the slope (0.01219) was determined (row data: table A8).

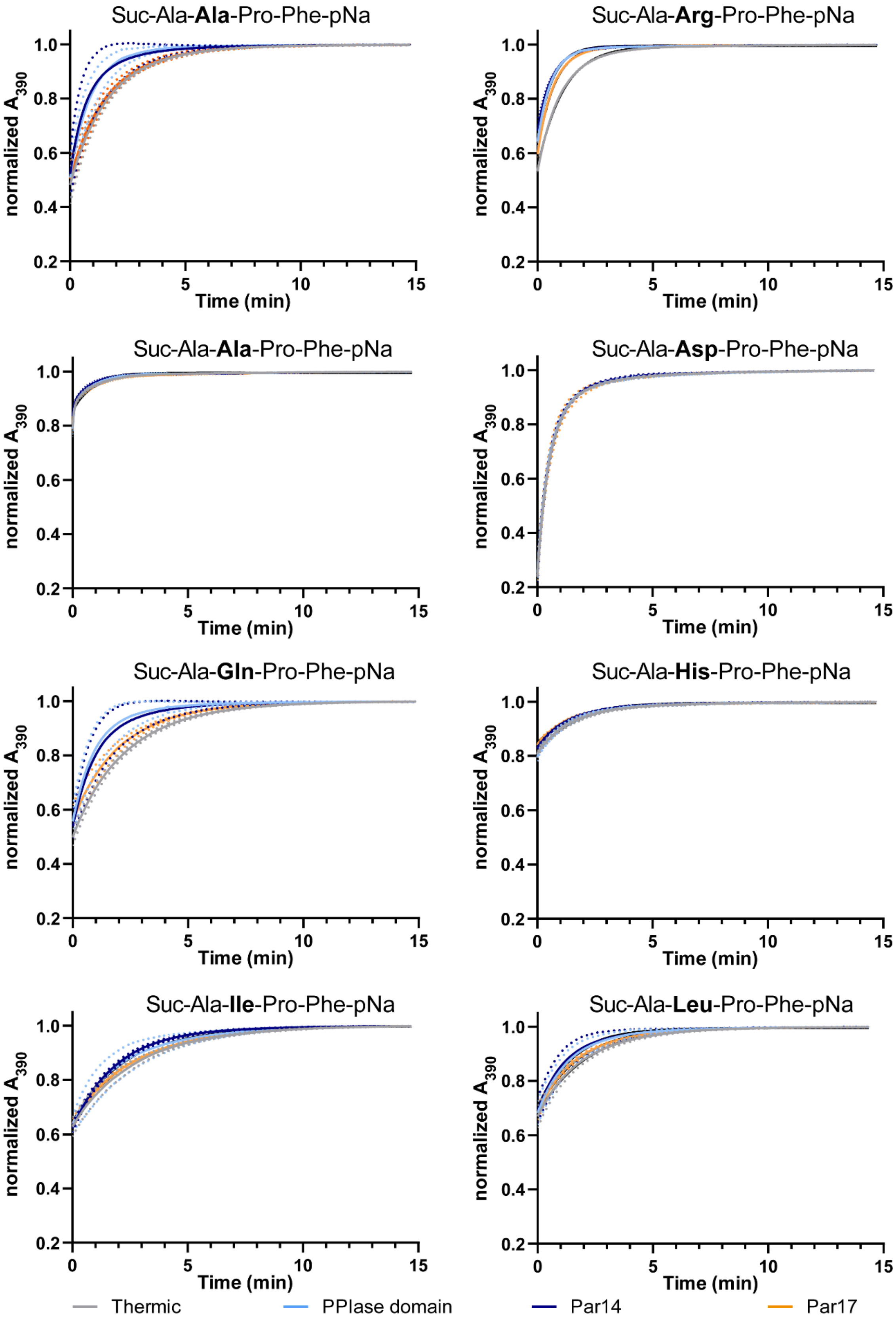

Appendix figure 5: Thermic and catalyzed reactions of the protease-coupled isomerase assay for different substrate peptides measured with Par17, Par14 and the isolated catalytic PPIase domain. [Continues on the next page]

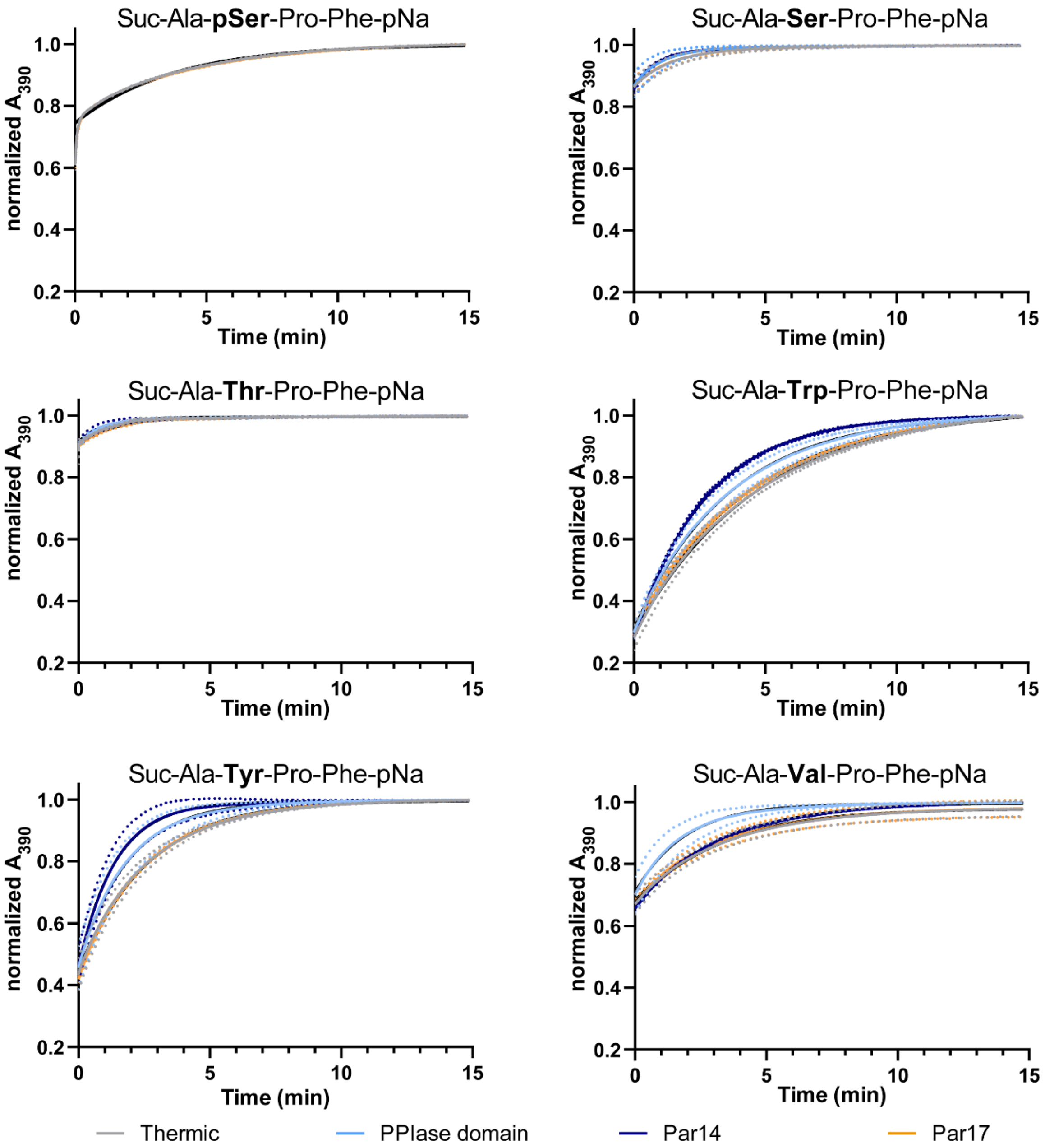

Appendix figure 5: Thermic and catalyzed reactions of the protease-coupled isomerase assay for different substrate peptides measured with Par17, Par14 and the shared catalytic PPIase domain. The mean changes in absorbance at 390 nm over time for different model substrate are displayed. The heading indicates the measured peptide. The dots represent the standard deviation of at least three measurements (exact number of measurements see table A7).

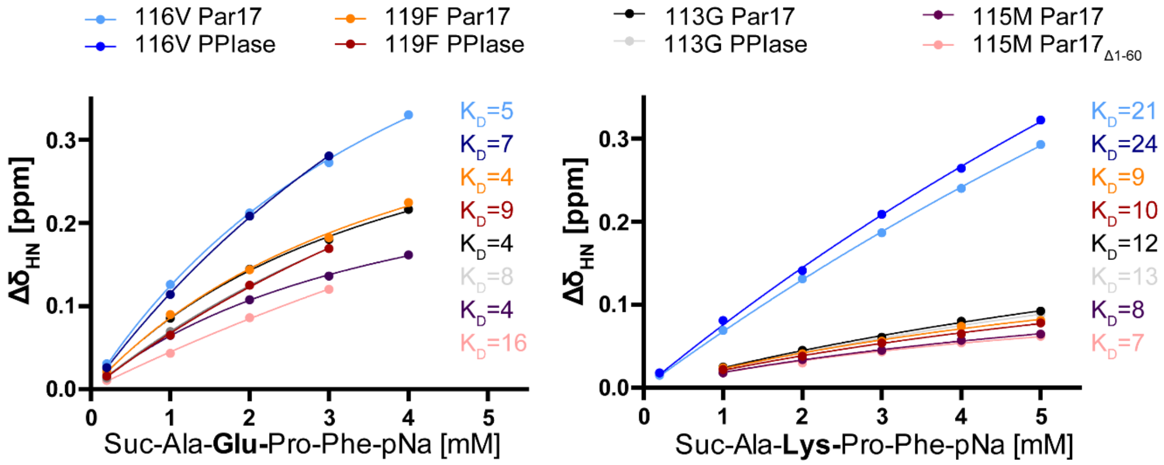

Appendix figure 6: NMR titration of Par17 and the isolated PPIase domain with two model substrate peptides. Chemical shift changes of the strongest changing amino acids of Par17 or the catalytic domain PPIase domain plotted against the used concentration of model substrate in which either glutamine (left) or lysine (right) is preceding proline. The dissociation constant KD was fitted with equation 4 and is shown in the corresponding color of the amino acid.

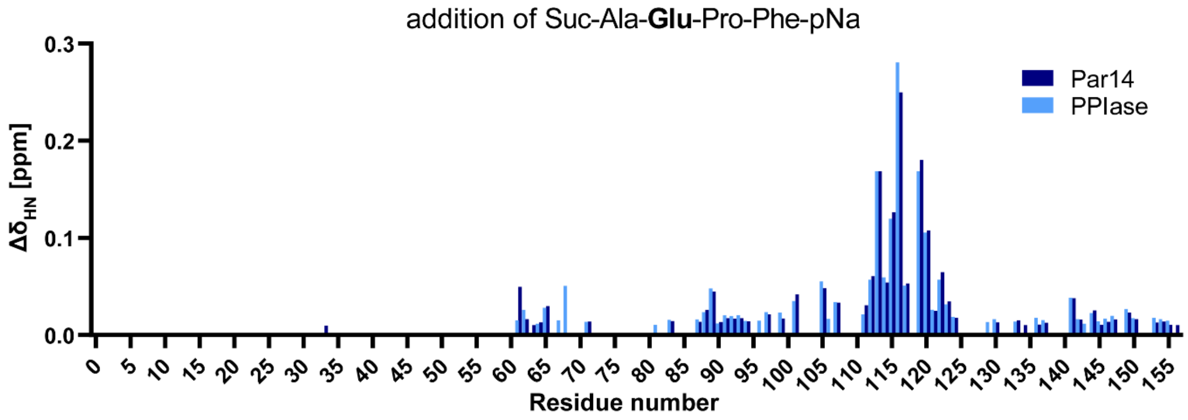

Appendix figure 7: Chemical shift changes in Par14 and the isolated PPIase domain after the addition of the model substrate Suc-Ala-Glu-Pro-Phe-pNa. Chemical shift changes measured for amide resonances of ^{15}N labeled Par14 (350 µM) and PPIase domain (200 µM) before and after the addition of the model substrate (3mM) at 20 °C in 50 mM KPi buffer and at pH 6.7 (chemical shift change values in table A10). The residue numbers of Par14 correspond to the one of Par17 for comparison (each amino acid number + 25).

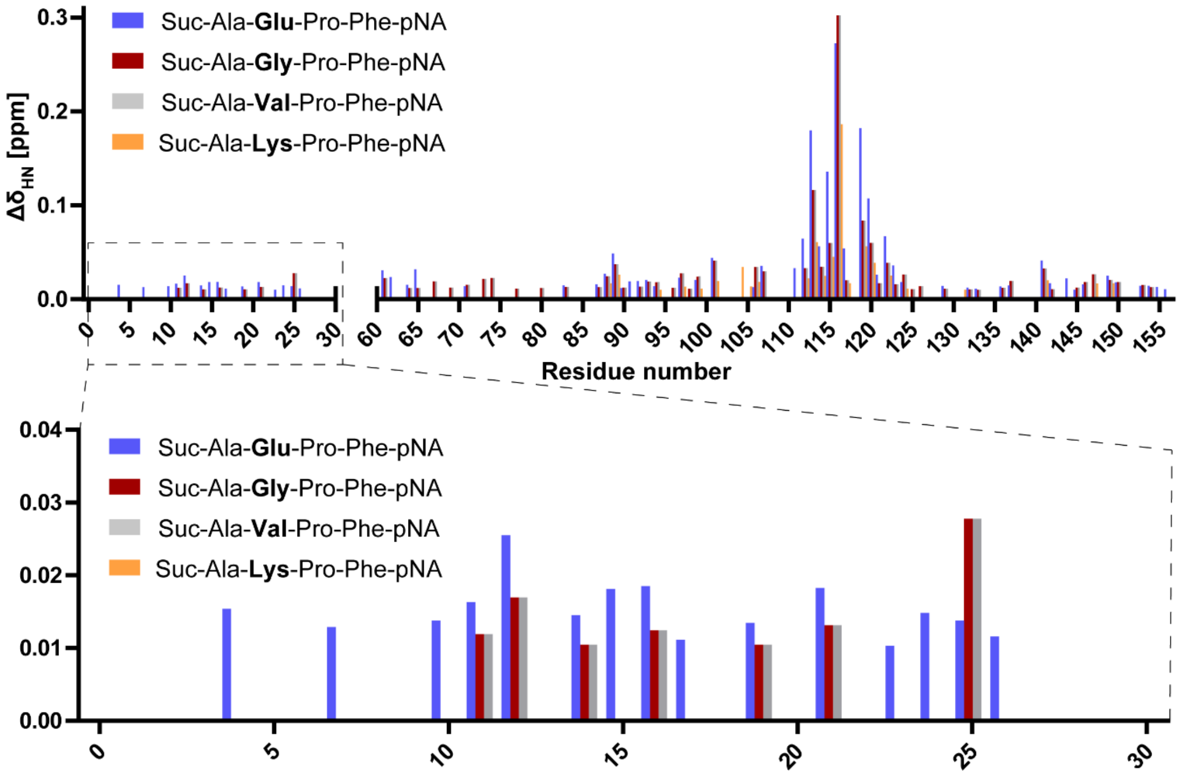

Appendix figure 8: Chemical shift changes in Par17 after the addition of the different model substrates. Chemical shift changes measured for amide resonances of ^{15}N-labeled Par17 (300 µM, except for the Lys-peptide 200 µM) before and after the addition of the model substrate (3 mM each) at 20 °C in 50 mM KPi buffer and at pH 6.7 (chemical shift change values in table A10). For the chemical shift changes of the amide resonance of the first 25 additional amino acids of the N-terminus, a cutout magnification was created.

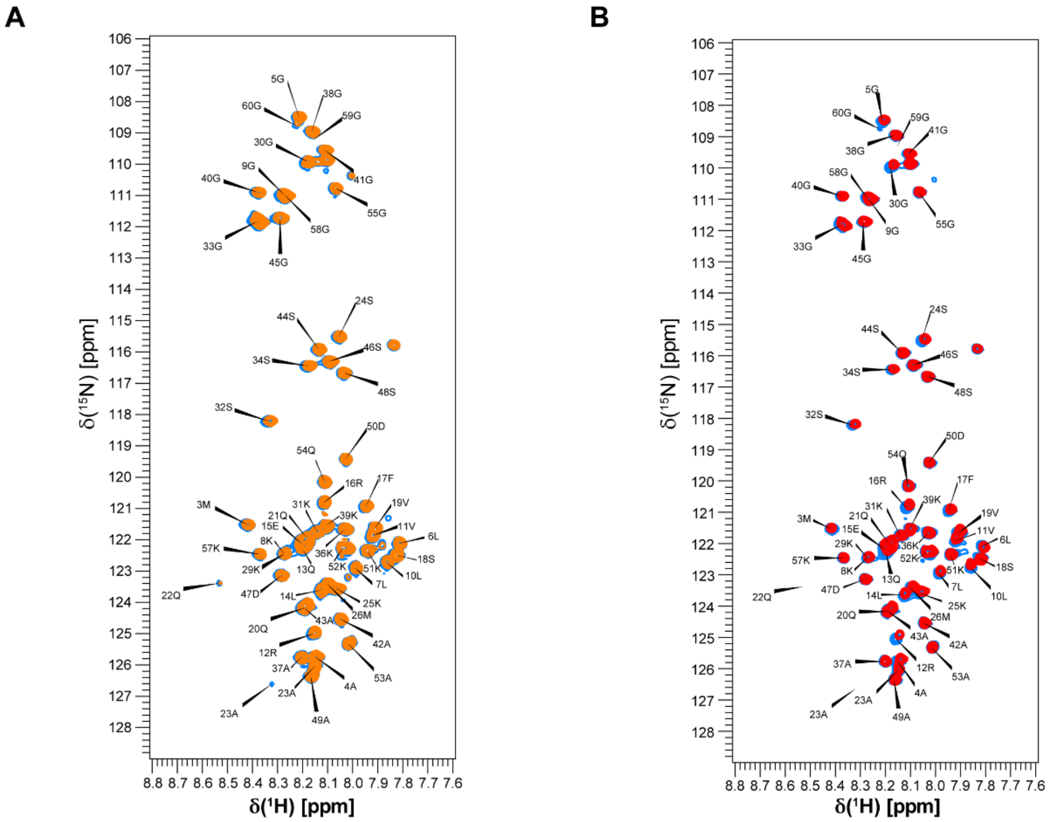

Appendix figure 9: Superposition of $^1H^{15}N$-HSQC spectra of Par17's N-terminus before and after addition of model substrate. Overlay of $^1H^{15}N$-HSQC spectra of Par17's N-terminus (Par17$_{\Delta61\text{-}156}$) in absence (cyan) and presence of A: 5 mM Suc-Ala-Lys-Pro-Phe-pNa (orange) or B: 4.5 mM Suc-Ala-Glu-Pro-Phe-pNa (red). Measurements were carried out at 20 °C in 50 mM KPi buffer and at pH 6.7. Amide resonances of Par17's N-terminus residues were labeled according to the known assignment of Lin et al. [74].

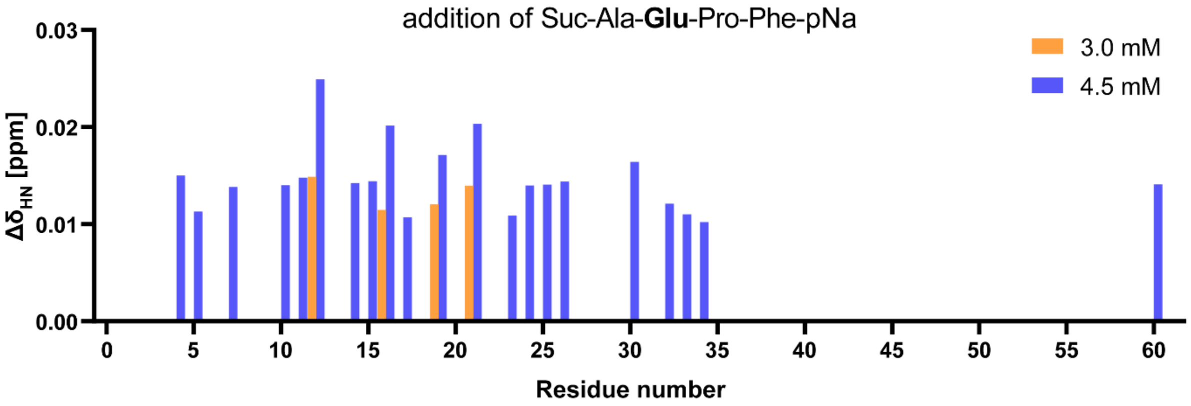

Appendix figure 10: Chemical shift changes in N-terminus of Par17 after the addition of the model substrate Suc-Ala-Glu-Pro-Phe-pNa. Chemical shift changes measured for amide resonances of 15N-labeled Par17$_{\Delta61\text{-}156}$ (350 µM) before and after the addition of different concentrations of the model substrate at 20°C in 50 mM KPi buffer and at pH 6.7 (chemical shift change values in table A10).

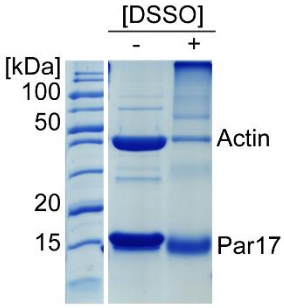

Appendix figure 11: SDS-gel of DSSO Cross-linking of Par17 with actin. Par17 and actin were incubated for 30 min and a sample was taken (DSSO-) then the DSSO was added. The solution was incubated for 10 min and a probe was collected (DSSO+). Samples were applied to an SDS gel in addition to a marker. The bands of native proteins and the protein size of the marker were labeled.

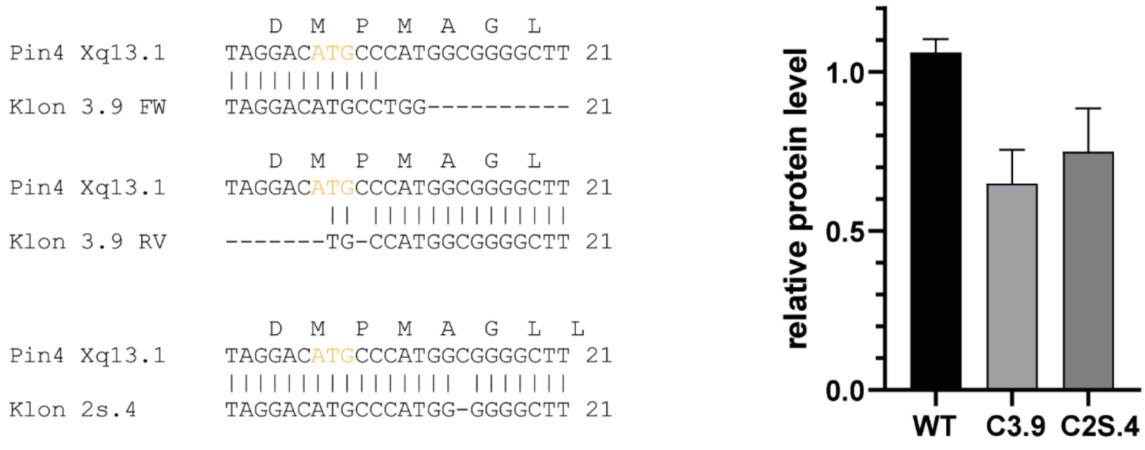

```
                        D  M  P  M  A  G  L
Pin4 Xq13.1       TAGGACATGCCCATGGCGGGGCTT 21
                  |||||||||||
Klon 3.9 FW       TAGGACATGCCTGG---------- 21

                        D  M  P  M  A  G  L
Pin4 Xq13.1       TAGGACATGCCCATGGCGGGGCTT 21
                         || ||||||||||||||
Klon 3.9 RV       -------TG-CCATGGCGGGGCTT 21


                        D  M  P  M  A  G  L  L
Pin4 Xq13.1       TAGGACATGCCCATGGCGGGGCTT 21
                  |||||||||||||||| |||||||
Klon 2s.4         TAGGACATGCCCATGG-GGGGCTT 21
```

Appendix figure 12: Sequences and relative protein levels of Par17 of the knockdown cell lines HEK293 C3.9 and HEK293 C2s.4. After single-cell dissociation the gDNA of the clones was isolated and analyzed for changes in the sequence. Clone 3.9 sequenced forward and reverse showed a deletion of a cysteine in the start sequence likely resulting in shifting of the reading frame, as well as the clone 2s.4. Since HEK293 is from a female donor, there are two X chromosomes. Therefore, the change does not have to lead to a complete deletion. The relative protein levels of Par17 in comparison to the wild type revealed a knockdown of 30%.

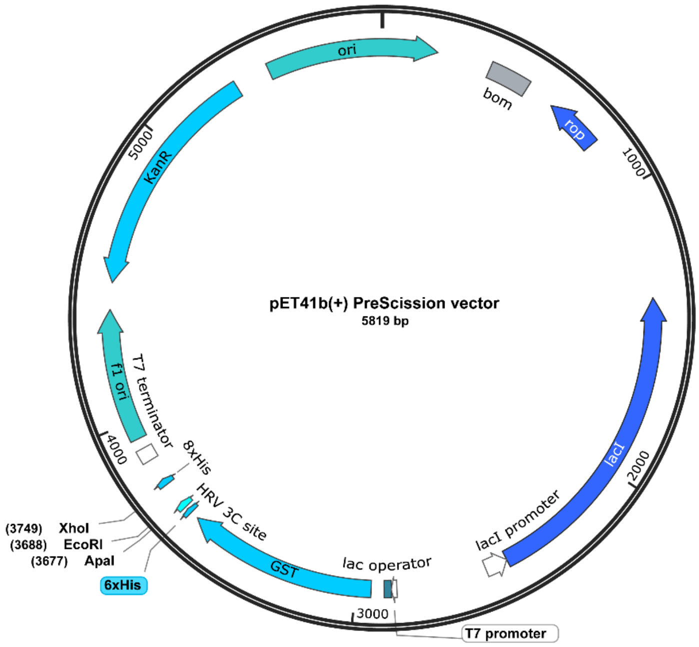

Term	Restriction enzymes	Insert sequence 5'-to-3'
BC697	ApaI/XhoI	CCCCAAAGGAAAAAGTGGTTCTGGAAAAGCGGGGAAAGGGGGAGCAGCCTCTGGGAGTGACAGTGCTGACAAGAAGGCTCAAGGTCCCAAAGGTGGTGGATCCTGGAGCCACCCGCAGTTCGAAAAATAAT
BC808	ApaI/XhoI	ATGGCGGGGCTTCTAAAGGGGCTTGTACGGCAACTGGAGCAGTTCAGAGTTCAACAACAAGCTTCCAAGATGCCGCCCAAAGGAAAAAGTGGTTCTGGAAAAGCGGGGAAAGGGGGAGCAGCCTCTGGGAGTGACAGTGCTGACAAGAAGGCTCAAGGTCCCAAAGGTGGTGGCAATGCAGTAAAGGTCAGACACATTCTATGTGAAAAACATGGCAAAATCATGGAAGCCATGGAAAAGTTAAAGTCTGGGATGAGATTCAATGAAGTGGCCGCACAGTATAGTGAAGATAAAGCCAGGCAAGGGGGTGACTTGGGTTGGATGACCAGAGGGTCCATGGTGGGACCATTTCAAGAAGCAGCATTTGCCTTGCCTGTAAGTGGGATGGATAAGCCTGTGTTTACAGACCCACCGGTTAAGACAAAATTTGGATATCATATTATTATGGTCGAAGGAAGAAAATAA
BC844	ApaI/EcoRI	ATGGGATCCAATGCAGTAAAGGTCAGACACATTCTATGTGAAAAACATGGCAAAATCATGGAAGCCATGGAAAAGTTAAAGTCTGGGATGAGATTCAATGAAGTGGCCGCACAGTATAGTGAAGATAAAGCCAGGCAAGGGGGTGACTTGGGTTGGATGACCAGAGGGTCCATGGTGGGACCATTTCAAGAAGCAGCATTTGCCTTGCCTGTAAGTGGGATGGATAAGCCTGTGTTTACAGACCCACCGGTTAAGACAAAATTTGGATATCATATTATTATGGTCGAAGGAAGAAAATAAT
BC880	ApaI/EcoRI	CCCCAAAGGAAAAAGTGGTTCTGGAAAAGCGGGGAAAGGGGGAGCAGCCTCTGGGAGTGACAGTGCTGACAAGAAGGCTCAAGGTCCCAAAGGTGGTGGCAATGCAGTAAAGGTCAGACACATTCTATGTGAAAAACATGGCAAAATCATGGAAGCCATGGAAAAGTTAAAGTCTGGGATGAGATTCAATGAAGTGGCCGCACAGTATAGTGAAGATAAAGCCAGGCAAGGGGGTGACTTGGGTTGGATGACCAGAGGGTCCATGGTGGGACCATTTCAAGAAGCAGCATTTGCCTTGCCTGTAAGTGGGATGGATAAGCCTGTGTTTACAGACCCACCGGTTAAGACAAAATTTGGATATCATATTATTATGGTCGAAGGAAGAAAATAAT
BC1119	ApaI/XhoI	ATGGCGGGGCTTCTAAAGGGGCTTGTACGGCAACTGGAGCAGTTCAGAGTTCAACAACAAGCTTCCAAGATGCCGCCCAAAGGAAAAAGTGGTTCTGGAAAAGCGGGGAAAGGGGGAGCAGCCTCTGGGAGTGACAGTGCTGACAAGAAGGCTCAAGGTCCCAAAGGTGGTGGCAATGCAGTAAAGGTCAGACACATTCTATGTGAAAAACATGGCAAAATCATGGAAGCCATGGAAAAGTTAAAGTCTGGGATGAGATTCAATGAAGTGGCCGCACAGTATAGTGAAGCTAAAGCCAGGCAAGGGGGTGACTTGGGTTGGATGACCAGAGGGTCCATGGTGGGACCATTTCAAGAAGCAGCATTTGCCTTGCCTGTAAGTGGGATGGATAAGCCTGTGTTTACAGACCCACCGGTTAAGACAAAATTTGGATATCATATTATTATGGTCGAAGGAAGAAAATAA
BC1356	/	CCCAAAGGAAAAAGTGGTTCTGGAAAAGCGGGGAAAGGGGGAGCAGCCTCTGGGAGTGACAGTGCTGACAAGAAGGCTCAAGGTCCCAAAGGTGGTGGATCCTGGAGCCACCCGCAGTTCGAAAAATAATAG
BC1366	ApaI/XhoI	ATGGCGGGGCTTCTAAAGGGGCTTGTACGGCAACTGGAGCAGTTCAGAGTTCAACAACAAGCTTCCAAGATGCCGCCCAAAGGAAAAAGTGGTTCTGGAAAAGCGGGGAAAGGGGGAGCAGCCTCTGGGAGTGACAGTGCTGACAAGAAGGCTCAAGGTCCCAAAGGTGGTGGCTGGAGCCACCCGCAGTTCGAAAAGTAATAG
BC1467	ApaI/XhoI	ATGGCGGGGCTTCTAAAGGGGCTTGTACGGCAACTGGAGCAGTTCAGAGTTCAACAACAAGCTTCCAAGATGCCGCCCAAAGGAAAAAGTGGTTCTGGAAAAGCGGGGAAAGGGGGAGCAGCCTCTGGGAGTGACAGTGCTGACAAGAAGGCTCAAGGTCCCAAAGGTGGTGGCTAATAG
BC1468	ApaI/EcoRI	GCTGACAAGAAGGCTCAAGGTCCCAAAGGTGGTGGCAATGCAGTAAAGGTCAGACACATTCTATGTGAAAAACATGGCAAAATCATGGAAGCCATGGAAAAGTTAAAGTCTGGGATGAGATTCAATGAAGTGGCCGCACAGTATAGTGAAGATAAAGCCAGGCAAGGGGGTGACTTGGGTTGGATGACCAGAGGGTCCATGGTGGGACCATTTCAAGAAGCAGCATTTGCCTTGCCTGTAAGTGGGATGGATAAGCCTGTGTTTACAGACCCACCGGTTAAGACAAAATTTGGATATCATATTATTATGGTCGAAGGAAGAAAATAA

Appendix figure 13: Vector map of the pET41(+) PreSission vector. The vector is demonstrated with its features and the used restriction enzyme sides. The sequence of the different inserts is listed with the used restriction enzymes.

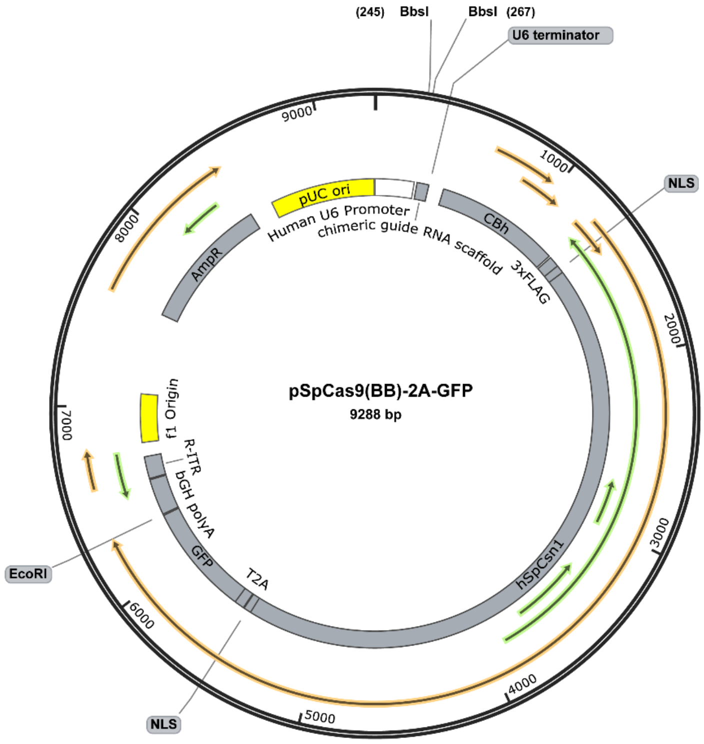

Term	Restriction enzymes	Insert sequence 5'-to-3'
BC1405	BbsI	CACCGCCCCTTTAGAAGCCCCGCCAT
BC1406	BbsI	CACCGTGTTTAGGACATGCCCATGG

Appendix figure 14: Vector map of the pSpCas9(BB)-2A-GFP vector. The vector is demonstrated with its features and the used restriction enzyme sides. The sequence of the different inserts is listed with the used restriction enzymes.

5.2 Appendix tables

Appendix table 1: Detailed liquid chromatography settings before mass spectrometry measurements.

Experiment (intern project number)	**DSSO-CL intramolecular (ACE 403)**		**Photo-CL intramolecular (ACE 366)**		**Photo-CL Fl-Par14/17 with cell lysate (ACE 0379,0321)**		**Photo-CL Par14/17 N-terminus with cell lysate (ACE 440)**		**DSSO-CL of Par17 and actin (ACE 0439)**	
MS device	Thermo Orbitrap Elite		Thermo Orbitrap Elite		Thermo Orbitrap Elite		Thermo Orbitrap Fusion Lumos		Thermo Orbitrap Elite	
LC device	Thermo Easy-nLC 1000		Thermo Easy-nLC 1000		Thermo Easy-nLC 1000		Thermo Easy-nLC 1000		Thermo Easy-nLC 1000	
Ion source	Thermo Nanospray Flex		Thermo Nanospray Flex		Thermo Nanospray Flex		Thermo Nanospray Flex		Thermo Nanospray Flex	
Colum oven (temperature)	Sonation column oven PRSO-V1 (45 °C)		Sonation column oven PRSO-V1 (45 °C)		Sonation column oven PRSO-V1 (45 °C)		Sonation column oven PRSO-V1 (45 °C)		Sonation column oven PRSO-V1 (45 °C)	
Analytic column	Self-packed fused silica capillary with integrated pico frit emitter		Self-packed fused silica capillary with integrated pico frit emitter		Self-packed fused silica capillary with integrated pico frit emitter		Self-packed fused silica capillary with integrated pico frit emitter		Self-packed fused silica capillary with integrated pico frit emitter	
Column diameter	75 µm × 37 cm		75 µm × 35 cm		75 µm × 35 cm		75 µm × 50 cm		75µM × 50 cm	
Stationary phase	Reprosil-Pur 120 Å C18-AQ		Reprosil-Pur 120 Å C18-AQ		Reprosil-Pur 120 Å C18-AQ		Reprosil-Pur 120 C18-AQ		Reprosil-Pur 120 C18-AQ	
Particle diameter	1.9 µM		1.9 µM				1.9 µM		1.9 µM	
Gradient (Solvent B (0.1 % in 80 % ACN, 20 % H_2O) Solvent A (0.1 % in H_2O)	time [min]	solvent B [%]	time [min]	solvent B [%]	time [min]	solvent B [%]	time [min]	solvent B [%]	time [min]	solvent B [%]
	0	7	0	7	0	7	0	9	0	9
	50	20	50	45	120	35	90	40	90	40
	130	45	60	80	130	80	100	100	100	100
	150	80	70	80	140	80	105	100	105	100
	160	80								
Flow rate [nl/min]	300		300		300		300		300	

Appendix table 2: Detailed mass spectrometry measurement settings.

Experiment (Intern project number) (MS/general)	**MS1**	**MS2**	**MS2**	**MS3**	**Comments; special settings**
DSSO-CL intramolecular (ACE 403) (Elite/ Tune v2.7.0.1112 SP2 Gradient: 160 min)	Analyzer: FT Res.: 120000 SR: 300 - 2000 AGC: 1×10^6 AcT: 70 ms RF: -- SF: -- DDM: NS	Analyzer: FT Res./ScR: 15000/- SR: Auto AGC: 1×10^5 AcT: 250 ms CS: > +2 IsM: IT IsW: 2.0 Frag.: HCD NCE: 31 NS: 10			classic orbitrap experiment: MS1 in orbitrap at high resolution and data dependent MS2 in orbitrap at 15000 resolution. Dynamic exclusion enabled (Exclude after n times = 1; Exclusion duration (s) = 80; Mass tolerance= ± 10ppm)
Photo-CL intramolecular (ACE 366) (Elite/ Tune v2.7.0.1112 SP2 Gradient: 160 min)	Analyzer: FT Res.: 120000 SR: 300 - 2000 AGC: 1×10^6 AcT: 50 ms RF: -- SF: -- DDM: NS	Analyzer: FT Res./ScR: 15000/- SR: Auto AGC: 1×10^5 AcT: 120 ms CS: > +2 IsM: IT IsW: 2.0 Frag.: CID NCE: 35 NS: 5	Analyzer: FT Res./ScR: 15000/- SR: Auto AGC: 1×10^5 AcT: 120 ms CS: > +2 IsM: IT IsW: 2.0 Frag.: ETD AT: 100 ms NS: 5		5th order double play orbitrap experiment: MS1 in orbitrap at high resolution and 2x data dependent MS2 in orbitrap at 15000 resolution (CID and ETD fragmentation). Dynamic exclusion enabled (Exclude after n times=1; Exclusion duration (s)= 120; Mass tolerance= ± 10ppm)
Photo-CL Fl-Par14/17 with cell lysate (ACE 0379,0321) (Elite/ Tune v2.7.0.1112 SP2 Gradient: 140 min)	Analyzer: FT Res.: 60000 SR: 300 - 1800 AGC: 3×10^6 AcT: 50 ms RF: -- SF: -- DDM: NS	Analyzer: FT Res./ScR: -/rapid SR: Auto AGC: 1×10^4 AcT: 50 ms CS: > +1 IsM: IT IsW: 2.0 Frag.: CID NCE: 35 NS: 15			classic orbitrap experiment: MS1 in orbitrap at high resolution and data dependent MS2 in orbitrap at 15000 resolution. Dynamic exclusion enabled (Exclude after n times = 1; Exclusion duration (s) = 80; Mass tolerance= ± 10ppm)
Photo-CL Par14/17 N-terminus with cell lysate (ACE 440) (Lumos/ Tune v v3.3.2782.28 Gradient: 105 min)	Analyzer: FT Res.: 240000 SR: 375 - 1500 AGC: Standard AcT: 50 ms RF: 30 SF: -- DDM: NS	Analyzer: IT Res./ScR: -/Turbo SR: 200-1400 AGC: 300 % AcT: 10 ms CS: > +2 - +7 IsM: Q IsW: 0.7 Frag.: HCD NCE: 35			classic orbitrap experiment: MS1 in orbitrap at high resolution and data dependent MS2 in ion trap at turbo scan rate. Dynamic exclusion enabled (Exclude after n times=1; Exclusion duration (s)= 60; mass tolerance= ± 10ppm)

DSSO-CL of Par17 and actin (ACE 0439) (Lumos/ Tune v3.1.2412.25 Gradient: 105 min)	Analyzer: FT Res.: 120000 SR: 375 - 1600 AGC: Standard AcT: 50 ms RF: 30 SF: 10V DDM: Ct/5sec	Analyzer: FT Res./ScR: 30000/- SR: Auto AGC: Auto AcT: 100 ms CS: > +2 IsM: Q IsW: 1.6 Frag.: CID NCE: 25	Analyzer: FT Res./ScR: 50000/- SR: Auto AGC: 400% AcT: 150 ms CS: > +2 IsM: Q IsW: 1.6 Frag.: EthcD NCE: 20 NS: 1	Analyzer: IT Res./ScR: 15000/- SR: Auto AGC: 200% AcT: 120 ms CS: > +2 IsM: IT IsW: 2.5 (MS) 2 (MS2) Frag.: HCD NCE: 35 NS: 4	First MS2 is triggered by targeted mass difference 31.9721 (DSSO). Second MS2 is performed in OT with EThcD. Fragments from first MS2 with triggered mass difference were collected for MS3 experiments (HCD in IT). The whole sequence MS1-MS2-MS2/MS3 was repeated for 5 sec (cycle time between master scans). Dynamic exclusion enabled (exclude after n times=1; Exclusion duration (s)= 60; mass tolerance= ± 10ppm)

FT = Fourier Transform (Orbitrap); **IT** = Ion trap; **Q**= Quadrupole; **Res.**= max. Resolution at 200 m/z (Lumos) or 400 m/z (Elite) [FWHM (full width at half maximum)]; **ScR** = scan rate for measurements in the IT; **SR**= scan range [m/z]; AGC= automatic gain control, max number of acquired ions per measurement; **AcT** = max. Ion acquisition time [ms]; **CS** = charge states used for fragmentation; **IsM** = Isolation mode (Q or IT), MS2 isolation and further is only done in IT; **IsW** = Isolation window [m/z], value followed by scan mode the isolation is based on (MS1, MS2 …) **Frag.**= Fragmentation method; **HCD** = Higher-energy collisional dissociation; **CID** = Collision-induced dissociation; **ETD** = Electron-transfer dissociation; **EThcD** = Electron-Transfer/Higher-Energy Collision Dissociation; **NCE** = normalized collision energy; cycles: number of MSn recorded or max cycle time; RF = RF Lens [%]; **SF**= Source Fragmentation [V]; **DDM** = Data dependent Mode (cycle time in seconds, CT/[s] or number of scans, NS); **NS** = Number of data dependent scans

Appendix table 3: Detailed search settings for the mass spectrometry data.

Experiment (intern project number)	**DSSO-CL intramolecular (ACE 403)**	**Photo-CL intramolecular (ACE 366)**	**Photo-CL Fl-Par14/17 with cell lysate (ACE 0379,0321)**	**Photo-CL Par14/17 N-terminus with cell lysate (ACE 440)**	**DSSO-CL of Par17 and actin (ACE 0439)**
Peptide and Protein identification and Data analysis	Proteome Discoverer 2.2 SEQUEST[1] and XlinkX[2]	Proteome Discoverer 2.2 and StavroX 3.6.6	MaxQuant 1.5.3.30 search engine Andromeda	MaxQuant v1.6.3.4 search engine Andromeda	Proteome Discoverer 2.2. XlinkX 2.0
precursor ion mass tolerance:	10 ppm[1,2]	10 ppm	20 ppm (first search) 4.5 ppm (main search)	20 ppm 4.5 ppm (main search)	5 ppm
product ion mass tolerance:	0.1 Da[1], 20 ppm[2]	10 ppm			0.02 ppm
Fixed modifications	Carbamidomethylation[1,2]	Carbamidomethylation	Carbamidomethylation	Carbamidomethylation	Carbamidomethylation
Digestion mode	Trypsin/P (specific) [1,2]	Trypsin/P (specific)	Trypsin/P (specific)	Trypsin/P (specific)	Trypsin/P (specific)
Variable modification	Acetyl (N-term) [1] Oxidation (M) [1,2] DSSO[1] DSSO amidated[1] DSSO hydrolyzed[1]	Oxidation (M) Met oxidation photo-Met was added as amino acid (“x”, 139.0755) all 20 amino acids were potential cross-linking sites	Acetyl (N-term); Oxidation (M) Alkylation (C)	Acetyl (N-term) Oxidation (M) Alkylation (C)	Oxidation (M), DSSO DSSO amidated, DSSO hydrolyzed, DSSO Tris
Allowed missed-cleavage	2[1,2]	3	2	2	2
FDR	0.01[1,2]	0.05	0.01	0.01	0.01

Appendix table 4: Proportions of initial *cis/trans* populations of model peptides Suc-Ala-Xaa-Pro-Phe-pNa obtained from PPIase Assay.

Xaa	*cis*-isomer [%]	*trans*-isomer [%]	Xaa	*cis*-isomer [%]	*trans*-isomer [%]
Asp	75	25	Leu	42	68
Trp	62	28	Arg	39	61
Glu	52	48	Ile	37	63
Phe	50	50	Val	32	68
Ala	49	51	Gly	22	78
Tyr	46	44	Asn	19	81
Gln	48	52	His	18	82
Glu	52	48	Ser	14	86
Lys	47	53	Thr	10	90

5.2.1 Table description of the attached tables

Appendix table 5: Chemical shifts changes of residues between the parvulin isoforms from Fig. 6. The chemical shifts for the peaks were extracted from ccpNMR analysis program and listed in the table. Sheet 1: Chemical shift changes between the Par14 and the isolated PPIase domain ≥ 0.01 ppm. Sheet 2: Chemical shift changes between Par17 and the isolated PPIase domain ≥ 0.01 ppm. Sheet 3: Chemical shift changes between Par17 and Par14 ≥ 0.01 ppm. Sheet 4: Chemical shift changes between the Par14Δ1-22 and the isolated PPIase domain ≥ 0.01 ppm.

Appendix table 6: Row and extracted data of the Photo and DSSO cross-linking. The cross-linking data was extracted from the analysis programs Proteome discoverer and StavroX and further evaluated. The cross-links depicted in figure 7 and figure 8 were marked. Sheet1: exported photo cross-linking data of Par14 from StavroX. Sheet 2: Photo cross-links of Par14 with a score ≥ 100 and measured distances. Sheet 3: exported photo cross-linking data of Par17 from StavroX. Sheet 4: Photo cross-links of Par17 with a score ≥ 100 and measured distances. Sheet 5: exported DSSO cross-links of Par14 from the Proteome discoverer. Sheet 6: DSSO cross-links of Par14 with a score ≥ 90 and measured distances. Sheet 7: exported DSSO cross-links of Par17 from the Proteome discoverer. Sheet8: DSSO cross-links of Par17 with a score ≥ 90 and measured distances.

Appendix table 7: Data of the PPIase assay measurements with the model substrate Suc-Ala-Ser-Pro-Phe-pNa and various Par17 concentrations. Sheet 1: Absorption measured at 390 nm at different time points for the PPIase Assay with different Par17 concentrations and the model substrate Suc-Ala-Ser-Pro-Phe-pNa. Sheet 2: Normalization of the data to the highest measured absorption of the respective measurement. Sheet 3: Rate constants calculated for each measurement by GraphPad Prism.

Appendix table 8: Data of the Michaelis-Menten kinetic measurements with Par14. Absorption measured at 390 nm at different time points in the PPIase Assay with different concentrations of the peptide Suc-Ala-Gln-Pro-Phe-pNa Sheet 1: of the thermic reaction and Sheet 2: of the catalytic reaction with Par14. Sheet 3: Slope of the first 10 data points from the measurements extracted from GraphPad Prism and the calculation of the initial velocity.

Appendix table 9: Row data, normalized data and calculations of the peptides measured with the PPIase Assay. For each peptide measured, there is a sheet containing the raw data (named Xaa_row), a sheet containing the normalized values (named Xaa_normalized) and a sheet containing the fitted rate constants from GraphPad Prism and the corresponding evaluations (named Xaa_normalized). The 18 measured peptides were ordered alphabetically by the amino acid preceding proline.

Appendix table 10: Chemical shift changes between the bound and free signals of the parvulin forms with all measured substrate peptides. Combined chemical shift perturbation of Sheet 1: the catalytic PPIase domain with 3 mM Lys-Xaa substrate peptide, Sheet 2: Par17 with 3 mM Lys-Pro substrate peptide, Sheet 3: the catalytic PPIase domain with 3 mM Glu-Pro substrate peptide, Sheet 4: Par17 with 3 mM Glu-Pro substrate peptide and Sheet 5: Par17 with 3 mM Glu-Pro substrate peptide. The Shift 1A, Shift 1B, Δ1 (ppm), Shift 2A, Shift 2B, Δ2 (ppm), Shift Distance, and Sequence number were listed respectively. Sheet 6: Combined chemical shift perturbations of selected amino acids of Par17 and the PPIase domain at various concentrations after addition of both model substrates (Glu-Pro or Lys-Pro). Sheet 7: Combined chemical shift perturbation of Par17 with 3 mM Gly-Pro substrate peptide. Sheet 8: Combined chemical shift perturbation of Par17 with 3 mM Val-Pro substrate peptide. Sheet 9: Combined chemical shift perturbation of Par17's N-terminus with 3 mM or 4.5 mM Glu-Pro substrate peptide.

Appendix Table 11: Venn diagram with proteins enriched by Par14 or Par17 compared with interactors available from other sources. Sheet 1: Interactors of PIN4 listed in the BioGRID$^{4.2}$ interaction repository. Shee2: Input, interactors of PIN4 listed in the BioGrid$^{4.2}$ DB, Par14 and Par17. Output, Interactors unique for BioGrid$^{4.2}$ DB, Par14 and Par17, interactors shared by BioGrid$^{4.2}$ DB PIN4 binding partners/Par14 and by Par14/Par17. Sheet 2: Input, interactors identified by Frattini et al. (2018), Par14 and Par17. Output, binding partners unique for Frattini, Par14 and Par17, and interactors shared between Par14/Frattini, Par17/Frattini, Par14.

Appendix Table 12: Venn diagram with proteins enriched by Par14's N-terminus, Par17's N-terminus compared to the enriched proteins of the full-length parvulins. Sheet 1: Input, interactors of Par14's N-terminus and Par17's N-terminus. Output, Interactors unique for Par14's N-terminus and Par17's N-terminus, Interactors shared between both N-termini. Sheet 2: Input, interactors identified by Par14's N-terminus and full length Par14. Output, binding partners unique for Par14's N-terminus and Par14 and interactors shared between Par14/Par14 N-terminus. Sheet 3: Input, interactors identified by Par17's N-terminus, Par14 and Par17. Output, binding partners unique for Par17's N-terminus, Par14 and Par17 and interactors shared between Par17 N-terminus/Par14, Par17 N-terminus/Par17, Par17/Par14 and Par17 N-terminus/Par17/Par14.

Appendix table 13: Enriched proteins of Par14's N-terminus classified in categories. Proteins were organized into functional categories (column A, bold and underlined). Groups and attributed proteins were listed along with their Protein ID, Protein names, Gene name and further specifications/features extracted from KEGG, GOMP name or additional information.

Appendix table 14: Protein interactions identified by STRING for the bait Proteins of Par14's N-terminus. Sheet 1: Protein interactions retrieved in the STRING database for the enriched Proteins of the Par14 N-terminus (scores > 0.4, Fig 16). Gene names of interacting proteins were listed in column A (node 1) and B (node 2), respectively. Second 2: Formed clusters were listed for the enriched proteins of the Par14 N-terminus.

Appendix table 15: Enriched proteins of Par17's N-terminus classified in categories. Proteins were organized into functional categories (column A, underlined, bold). Proteins were listed along with their protein ID, Protein name, Gene name, Protein short name and further specifications/features extracted from KEGG, GOMP name or additional information.

Appendix table 16: Protein interactions identified by STRING for the bait Proteins of Par17's N-terminus. Sheet 1: Protein interactions retrieved in the STRING database for the enriched Proteins of the Par17 N-terminus (scores > 0.4, Fig 16). Gene names of interacting proteins were listed in column A (node 1) and B (node 2), respectively. Second 2: Formed clusters were listed for the enriched proteins of the Par17 N-terminus.

Appendix table 17: DSSO cross-linking data of Par17 and Actin exported from Proteome discoverer. Sheet 1: The score and the details of the cross-linked peptides of the proteins were listed. All cross-links with a score >130 between Actin (P63261) und Par17 were depicted in Figure 18. Sheet 2: HADDOCK restrains for the Par17 actin complex modulation.

Appendix table 18: Mito Stress Test measured oxygen consumption rate and normalization. All sheets contain the OCR values extracted from the Wave measurement program (where the OCR was normalized to the cell count per well). In addition, the measured values for the different respirations were combined and then normalized with the respective mean value of the LV cell line. Sheet 1: first measurement, depicted in the flow chart in Fig 20A. Sheet 2: second Measurement, Sheet 3: third Measurement without the WT cell line.

6 References

1. Achuthankutty D, Thakur RS, Haahr P et al. (2019) Regulation of ETAA1-mediated ATR activation couples DNA replication fidelity and genome stability. J Cell Biol 218(12): 3943–3953. doi: 10.1083/jcb.201905064
2. Albers MW, Walsh CT, Schreiber SL (1990) Substrate specificity for the human rotamase FKBP: a view of FK506 and rapamycin as leucine-(twisted amide)-proline mimics. J. Org. Chem. 55(17): 4984–4986. doi: 10.1021/jo00304a003
3. Arlt C, Götze M, Ihling CH et al. (2016) Integrated Workflow for Structural Proteomics Studies Based on Cross-Linking/Mass Spectrometry with an MS/MS Cleavable Cross-Linker. Anal. Chem. 88(16): 7930–7937. doi: 10.1021/acs.analchem.5b04853
4. Bartolome F, Esteras N, Martin-Requero A et al. (2017) Pathogenic p62/SQSTM1 mutations impair energy metabolism through limitation of mitochondrial substrates. Sci Rep 7(1): 1666. doi: 10.1038/s41598-017-01678-4
5. Bayer E, Goettsch S, Mueller JW et al. (2003) Structural analysis of the mitotic regulator hPin1 in solution: insights into domain architecture and substrate binding. J. Biol. Chem. 278(28): 26183–26193. doi: 10.1074/jbc.M300721200
6. Berg JM, Tymoczko JL, Stryer L et al. (2014) Biochemie, 7. Auflage, korrigierter Nachdruck. Lehrbuch. Springer Spektrum, Berlin, Heidelberg
7. Black DJ, Tran Q-K, Keightley A et al. (2019) Evaluating Calmodulin-Protein Interactions by Rapid Photoactivated Cross-Linking in Live Cells Metabolically Labeled with Photo-Methionine. J Proteome Res 18(10): 3780–3791. doi: 10.1021/acs.jproteome.9b00510
8. Borger JL (2019) Verification of the activity of human Parvulin 14 and human Parvulin 17 with a protease coupled cis/trans isomerase assay, Universität Duisburg-Essen
9. Born A, Henen MA, Vögeli B (2019) Activity and Affinity of Pin1 Variants. Molecules 25(1). doi: 10.3390/molecules25010036
10. Brand MD, Nicholls DG (2011) Assessing mitochondrial dysfunction in cells. Biochem J 435(Pt 2): 297–312. doi: 10.1042/BJ20110162
11. Brandts JF, Brennan M, Lung-Nan L (1977) Unfolding and refolding occur much faster for a proline-free proteins than for most proline-containing proteins. Proc Natl Acad Sci U S A 74(10): 4178–4181. doi: 10.1073/pnas.74.10.4178
12. Brohée S, van Helden J (2006) Evaluation of clustering algorithms for protein-protein interaction networks. BMC Bioinformatics 7: 488. doi: 10.1186/1471-2105-7-488
13. Burgardt NI, Linnert M, Weiwad M et al. (2012) NMR assignments of the FKBP-type PPIase domain of FKBP42 from Arabidopsis thaliana. Biomol NMR Assign 6(2): 185–188. doi: 10.1007/s12104-011-9352-z
14. Burgardt NI, Schmidt A, Manns A et al. (2015) Parvulin 17-catalyzed Tubulin Polymerization Is Regulated by Calmodulin in a Calcium-dependent Manner. J Biol Chem 290(27): 16708–16722. doi: 10.1074/jbc.M114.593228
15. Cheng C-W, Tse E (2018) PIN1 in Cell Cycle Control and Cancer. Frontiers in pharmacology 9: 1367. doi: 10.3389/fphar.2018.01367
16. Cheng HN, Bovey FA (1977) Cis-trans equilibrium and kinetic studies of acetyl-L-proline and glycyl-L-proline. Biopolymers 16(7): 1465–1472. doi: 10.1002/bip.1977.360160707
17. Clore GM, Iwahara J (2009) Theory, practice, and applications of paramagnetic relaxation enhancement for the characterization of transient low-population states of biological macromolecules and their complexes. Chem Rev 109(9): 4108–4139. doi: 10.1021/cr900033p
18. Combe CW, Fischer L, Rappsilber J (2015) xiNET: cross-link network maps with residue resolution. Mol Cell Proteomics 14(4): 1137–1147. doi: 10.1074/mcp.O114.042259
19. Cox J, Hein MY, Luber CA et al. (2014) Accurate proteome-wide label-free quantification by delayed normalization and maximal peptide ratio extraction, termed MaxLFQ. Mol Cell Proteomics 13(9): 2513–2526. doi: 10.1074/mcp.M113.031591
20. Cox J, Mann M (2008) MaxQuant enables high peptide identification rates, individualized p.p.b.-range mass accuracies and proteome-wide protein quantification. Nat Biotechnol 26(12): 1367–1372. doi: 10.1038/nbt.1511
21. Cox J, Neuhauser N, Michalski A et al. (2011) Andromeda: a peptide search engine integrated into the MaxQuant environment. J Proteome Res 10(4): 1794–1805. doi: 10.1021/pr101065j

22. DeCenzo MT, Park ST, Jarrett BP et al. (1996) FK506-binding protein mutational analysis: defining the active-site residue contributions to catalysis and the stability of ligand complexes. Protein Eng 9(2): 173–180. doi: 10.1093/protein/9.2.173

23. Dominguez R, Holmes KC (2011) Actin structure and function. Annu Rev Biophys 40: 169–186. doi: 10.1146/annurev-biophys-042910-155359

24. Doolittle LK, Rosen MK, Padrick SB (2013) Measurement and analysis of in vitro actin polymerization. Methods Mol Biol 1046: 273–293. doi: 10.1007/978-1-62703-538-5_16

25. Dugave C (2006) Cis-trans isomerization in biochemistry. Wiley-VCH, Weinheim

26. Erben ED, Valguarnera E, Nardelli S et al. (2010) Identification of an atypical peptidyl-prolyl cis/trans isomerase from trypanosomatids. Biochim Biophys Acta 1803(9): 1028–1037. doi: 10.1016/j.bbamcr.2010.05.006

27. Etzler JC, Bollo M, Holstein D et al. (2017) Cyclophilin D over-expression increases mitochondrial complex III activity and accelerates supercomplex formation. Arch Biochem Biophys 613: 61–68. doi: 10.1016/j.abb.2016.11.008

28. Fischer G (2000) Chemical aspects of peptide bond isomerisation. Chem. Soc. Rev. 29(2): 119–127. doi: 10.1039/a803742f

29. Fischer G, Bang H, Berger E et al. (1984) Conformational specificity of chymotrypsin toward proline-containing substrates. Biochim Biophys Acta 791(1): 87–97

30. Fischer G, Bang H, Mech C (1984) Nachweis einer Enzymkatalyse für die cis-trans-Isomerisierung der Peptidbindung in prolinhaltigen Peptiden (Determination of enzymatic catalysis for the cis-trans-isomerization of peptide binding in proline-containing peptides). Biomed Biochim Acta 43(10): 1101–1111

31. Fischer G, Wittmann-Liebold B, Lang K et al. (1989) Cyclophilin and peptidyl-prolyl cis-trans isomerase are probably identical proteins. Nature 337(6206): 476–478. doi: 10.1038/337476a0

32. Frattini V, Pagnotta SM, Tala et al. (2018) A metabolic function of *FGFR3-TACC3* gene fusions in cancer. Nature 553(7687): 222. doi: 10.1038/nature25171

33. Fujiyama S, Yanagida M, Hayano T et al. (2002) Isolation and proteomic characterization of human Parvulin-associating preribosomal ribonucleoprotein complexes. J Biol Chem 277(26): 23773–23780. doi: 10.1074/jbc.M201181200

34. Fujiyama-Nakamura S, Yoshikawa H, Homma K et al. (2009) Parvulin (Par14), a peptidyl-prolyl cis-trans isomerase, is a novel rRNA processing factor that evolved in the metazoan lineage. Molecular & cellular proteomics 8(7): 1552–1565. doi: 10.1074/mcp.M900147-MCP200

35. Gao Y, Thomas JO, Chow RL et al. (1992) A cytoplasmic chaperonin that catalyzes β-actin folding. Cell 69(6): 1043–1050. doi: 10.1016/0092-8674(92)90622-J

36. Garcin C, Straube A (2019) Microtubules in cell migration. Essays Biochem 63(5): 509–520. doi: 10.1042/EBC20190016

37. Goehring A, Michin I, Gerdes T et al. (2020) Targeting of parvulin interactors by diazirine mediated cross-linking discloses a cellular role of human Par14/17 in actin polymerization. Biol Chem(401(8)): 955–968. doi: 10.1515/hsz-2019-0423

38. Göthel SF, Marahiel MA (1999) Peptidyl-prolyl cis-trans isomerases, a superfamily of ubiquitous folding catalysts. Cellular and molecular life sciences 55: 423–436. doi: 10.1007/s000180050299

39. Götze M, Pettelkau J, Schaks S et al. (2012) StavroX--a software for analyzing crosslinked products in protein interaction studies. J Am Soc Mass Spectrom 23(1): 76–87. doi: 10.1007/s13361-011-0261-2

40. Greenwood AI, Rogals MJ, De S et al. (2011) Complete determination of the Pin1 catalytic domain thermodynamic cycle by NMR lineshape analysis. J Biomol NMR 51(1-2): 21–34. doi: 10.1007/s10858-011-9538-9

41. Hanes SD, Shank PR, Bostian KA (1989) Sequence and mutational analysis of ESS1, a gene essential for growth in Saccharomyces cerevisiae. Yeast 5(1): 55–72. doi: 10.1002/yea.320050108

42. Hani J, Stumpf G, Domdey H (1995) PTF1 encodes an essential protein in Saccharomyces cerevisiae , which shows strong homology with a new putative family of PPIases. FEBS Letters 365(2-3): 198–202. doi: 10.1016/0014-5793(95)00471-k

43. Harrison RK, Stein RL (1990) Substrate specificities of the peptidyl prolyl cis-trans isomerase activities of cyclophilin and FK-506 binding protein: evidence for the existence of a family of distinct enzymes. Biochemistry 29(16): 3813–3816. doi: 10.1021/bi00468a001

44. Häupl B, Ihling CH, Sinz A (2017) Combining affinity enrichment, cross-linking with photo-amino acids, and mass spectrometry for probing protein kinase D2 interactions. Proteomics. doi: 10.1002/pmic.201600459

45. Havugimana PC, Hart GT, Nepusz T et al. (2012) A census of human soluble protein complexes. Cell 150(5): 1068–1081. doi: 10.1016/j.cell.2012.08.011

46. Heikkinen O, Seppala R, Tossavainen H et al. (2009) Solution structure of the parvulin-type PPIase domain of Staphylococcus aureus PrsA--implications for the catalytic mechanism of parvulins. BMC Struct Biol 9: 17. doi: 10.1186/1472-6807-9-17

47. Hocking HG, Zangger K, Madl T (2013) Studying the structure and dynamics of biomolecules by using soluble paramagnetic probes. Chemphyschem 14(13): 3082–3094. doi: 10.1002/cphc.201300219

48. Hoppstock L, Trusch F, Lederer C et al. (2016) NmPin from the marine thaumarchaeote Nitrosopumilus maritimus is an active membrane associated prolyl isomerase. BMC Biol 14: 53. doi: 10.1186/s12915-016-0274-1

49. Hsu VL, Handschumacher RE, Armitage IM (1990) Peptidyl-prolyl cis-trans isomerase activity of cyclophilin studied by one-dimensional proton nuclear magnetic resonance spectroscopy. J Am Chem Soc 112(18): 6745–6747. doi: 10.1021/ja00174a064

50. Iacobucci C, Götze M, Piotrowski C et al. (2018) Carboxyl-Photo-Reactive MS-Cleavable Cross-Linkers: Unveiling a Hidden Aspect of Diazirine-Based Reagents. Anal. Chem. 90(4): 2805–2809. doi: 10.1021/acs.analchem.7b04915

51. Irobi E, Aguda AH, Larsson M et al. (2004) Structural basis of actin sequestration by thymosin-B4: Implications for arp2/3 activation

52. J Fanghanel GF (2004) Insights into the catalytic mechanism of peptidyl prolyl cis/trans isomerases

53. Justice RM, Kline AD, Sluka JP et al. (1990) The detection of proline isomerase activity in FK506-binding protein by two-dimensional 1H NMR exchange spectroscopy. Biochem Biophys Res Commun 171(1): 445–450. doi: 10.1016/0006-291X(90)91413-M

54. Kamba B (2018) Überprüfung der Substratselektivität des humanen Parvulins 14 (hPar14) mittels eines Protease-gekoppelten cis/trans-Isomeraseassays. Master thesis, Universität-Duisburg Essen

55. Kanehisa M, Goto S (2000) KEGG: kyoto encyclopedia of genes and genomes. Nucleic Acids Res 28(1): 27–30. doi: 10.1093/nar/28.1.27

56. Kang C, Ye H, Chia J et al. (2013) Functional role of the flexible N-terminal extension of FKBP38 in catalysis. Sci Rep 3: 2985. doi: 10.1038/srep02985

57. Kao A, Chiu C, Vellucci D et al. (2011) Development of a novel cross-linking strategy for fast and accurate identification of cross-linked peptides of protein complexes. Mol Cell Proteomics 10(1): M110.002212. doi: 10.1074/mcp.M110.002212

58. Keller RLJ (2005) Optimizing the process of nuclear magnetic resonance spectrum analysis and computer aided resonance assignment, ETH Zurich

59. Kennedy SA, Jarboui M-A, Srihari S et al. (2020) Extensive rewiring of the EGFR network in colorectal cancer cells expressing transforming levels of KRASG13D. Nat Commun 11(1): 499. doi: 10.1038/s41467-019-14224-9

60. Kern D, Kern G, Scherer G et al. (1995) Kinetic analysis of cyclophilin-catalyzed prolyl cis/trans isomerization by dynamic NMR spectroscopy. Biochemistry 34(41): 13594–13602. doi: 10.1021/bi00041a039

61. Kessler D, Papatheodorou P, Stratmann T et al. (2007) The DNA binding parvulin Par17 is targeted to the mitochondrial matrix by a recently evolved prepeptide uniquely present in Hominidae. BMC Biol 5: 37. doi: 10.1186/1741-7007-5-37

62. Kieffer LJ, Thalhammer T, Handschumacher RE (1992) Isolation and characterization of a 40-kDa cyclophilin-related protein. J. Biol. Chem. 267(8): 5503–5507. doi: 10.1016/S0021-9258(18)42795-0

63. Kofron JL, Kuzmic P, Kishore V et al. (1991) Determination of kinetic constants for peptidyl prolyl cis-trans isomerases by an improved spectrophotometric assay. Biochemistry 30(25): 6127–6134. doi: 10.1021/bi00239a007

64. Kouri ED, Labrou NE, Garbis SD et al. (2009) Molecular and biochemical characterization of the parvulin-type PPIases in Lotus japonicus. Plant Physiol 150(3): 1160–1173. doi: 10.1104/pp.108.132415

65. Krieger E, Joo K, Lee J et al. (2009) Improving physical realism, stereochemistry, and side-chain accuracy in homology modeling: Four approaches that performed well in CASP8. Proteins 77 Suppl 9: 114–122. doi: 10.1002/prot.22570

66. Krieger E, Vriend G (2014) YASARA View - molecular graphics for all devices - from smartphones to workstations. Bioinformatics 30(20): 2981–2982. doi: 10.1093/bioinformatics/btu426

67. Kühlewein A, Voll G, Hernandez Alvarez B et al. (2004) Solution structure of Escherichia coli Par10. The prototypic member of the Parvulin family of peptidyl-prolyl cis/trans isomerases. Protein Sci 13(9): 2378–2387. doi: 10.1110/ps.04756704

68. Lang K, Schmid FX, Fischer G (1987) Catalysis of protein folding by prolyl isomerase. Nature 329(6136): 268–270. doi: 10.1038/329268a0

69. Laurent EM, Sofianatos Y, Komarova A et al. (2020) Global BioID-based SARS-CoV-2 proteins proximal interactome unveils novel ties between viral polypeptides and host factors involved in multiple COVID19-associated mechanisms

70. Lederer C, Heider D, van den Boom J et al. (2011) Single-domain parvulins constitute a specific marker for recently proposed deep-branching archaeal subgroups. Evol Bioinform Online 7: 135–148. doi: 10.4137/EBO.S7683

71. Lehnart SE, Huang F, Marx SO et al. (2003) Immunophilins and coupled gating of ryanodine receptors. Curr Top Med Chem 3(12): 1383–1391. doi: 10.2174/1568026033451907

72. Leitner A, Walzthoeni T, Kahraman A et al. (2010) Probing native protein structures by chemical cross-linking, mass spectrometry, and bioinformatics. Molecular & cellular proteomics 9(8): 1634–1649. doi: 10.1074/mcp.R000001-MCP201

73. Lin J-S, Lai E-M (2017) Protein-Protein Interactions: Co-Immunoprecipitation. Methods Mol Biol 1615: 211–219. doi: 10.1007/978-1-4939-7033-9_17

74. Lin Y-J, Schmidt A, Burgardt NI et al. (2013) ^{1}H, ^{13}C and ^{15}N resonance assignments of human parvulin 17. Biomol NMR Assign 7(2): 325–329. doi: 10.1007/s12104-012-9438-2

75. Liu F, Lössl P, Scheltema R et al. (2017) Optimized fragmentation schemes and data analysis strategies for proteome-wide cross-link identification. Nat Commun 8: 15473. doi: 10.1038/ncomms15473

76. Liu J, Albers MW, Chen CM et al. (1990) Cloning, expression, and purification of human cyclophilin in Escherichia coli and assessment of the catalytic role of cysteines by site-directed mutagenesis. Proc Natl Acad Sci U S A 87(6): 2304–2308. doi: 10.1073/pnas.87.6.2304

77. Lössl P, Kölbel K, Tänzler D et al. (2014) Analysis of nidogen-1/laminin γ1 interaction by cross-linking, mass spectrometry, and computational modeling reveals multiple binding modes. PLoS ONE 9(11): e112886. doi: 10.1371/journal.pone.0112886

78. Lu KP, Hanes SD, Hunter T (1996) A human peptidyl-prolyl isomerase essential for regulation of mitosis. Nature 380(6574): 544–547. doi: 10.1038/380544a0

79. Lu PJ, Wulf G, Zhou XZ et al. (1999) The prolyl isomerase Pin1 restores the function of Alzheimer-associated phosphorylated tau protein. Nature 399(6738): 784–788. doi: 10.1038/21650

80. Lu PJ, Zhou XZ, Shen M et al. (1999) Function of WW domains as phosphoserine- or phosphothreonine-binding modules. Science 283(5406): 1325–1328. doi: 10.1126/science.283.5406.1325

81. Luo C, Long J, Liu J (2008) An improved spectrophotometric method for a more specific and accurate assay of mitochondrial complex III activity. Clin Chim Acta 395(1-2): 38–41. doi: 10.1016/j.cca.2008.04.025

82. Maigret B, Perahia D, Pullman B (1970) Molecular orbital calculations on the conformation of polypeptides and proteins IV. The conformation of the prolyl and hydroxyprolyl residues. Journal of Theoretical Biology 29(2): 275–291. doi: 10.1016/0022-5193(70)90022-6

83. Mallis RJ, Brazin KN, Fulton DB et al. (2002) Structural characterization of a proline-driven conformational switch within the Itk SH2 domain. Nat Struct Biol 9(12): 900–905. doi: 10.1038/nsb864

84. Matena A, Rehic E, Hönig D et al. (2018) Structure and function of the human parvulins Pin1 and Par14/17. Biol Chem 399(2): 101–125. doi: 10.1515/hsz-2017-0137

85. Matena A, Sinnen C, van den Boom J et al. (2013) Transient domain interactions enhance the affinity of the mitotic regulator Pin1 toward phosphorylated peptide ligands. Structure 21(10): 1769–1777. doi: 10.1016/j.str.2013.07.016

86. McQuin C, Goodman A, Chernyshev V et al. (2018) CellProfiler 3.0: Next-generation image processing for biology. PLoS Biol 16(7): e2005970. doi: 10.1371/journal.pbio.2005970

87. Moerke NJ (2009) Fluorescence Polarization (FP) Assays for Monitoring Peptide-Protein or Nucleic Acid-Protein Binding. Curr Protoc Chem Biol 1(1): 1–15. doi: 10.1002/9780470559277.ch090102

88. Mueller JW, Bayer P (2008) Small Family with Key Contacts. Par14 and Par17 Parvulin Proteins, Relatives of Pin1, Now Emerge in Biomedical Research. Perspect Medicin Chem 2: 11–20

89. Mueller JW, Kessler D, Neumann D et al. (2006) Characterization of novel elongated Parvulin isoforms that are ubiquitously expressed in human tissues and originate from alternative transcription initiation. BMC Mol Biol 7: 9. doi: 10.1186/1471-2199-7-9

90. Mueller JW, Link NM, Matena A et al. (2011) Crystallographic proof for an extended hydrogen-bonding network in small prolyl isomerases. J Am Chem Soc 133(50): 20096–20099. doi: 10.1021/ja2086195

91. Mueller JW, Link NM, Matena A et al. (2012) 0.89 A resolution crystal structure of human Parvulin 14 in complex with oxidized DTT

92. Murray J, Zhang B, Taylor SW et al. (2003) The subunit composition of the human NADH dehydrogenase obtained by rapid one-step immunopurification. J. Biol. Chem. 278(16): 13619–13622. doi: 10.1074/jbc.C300064200

93. Olsen JV, Godoy LMF de, Li G et al. (2005) Parts per million mass accuracy on an Orbitrap mass spectrometer via lock mass injection into a C-trap. Mol Cell Proteomics 4(12): 2010–2021. doi: 10.1074/mcp.T500030-MCP200

94. Pastorino L, Sun A, Lu P-J et al. (2006) The prolyl isomerase Pin1 regulates amyloid precursor protein processing and amyloid-beta production. Nature 440(7083): 528–534. doi: 10.1038/nature04543

95. Pemberton JR (1975) Retention of mercurial preservatives in desiccated biological products. J Clin Microbiol 2(6): 549–551

96. Pemberton TJ, Kay JE (2005) Identification and comparative analysis of the peptidyl-prolyl cis/trans isomerase repertoires of H. sapiens, D. melanogaster, C. elegans, S. cerevisiae and Sz. pombe. Comp Funct Genomics 6(5-6): 277–300. doi: 10.1002/cfg.482

97. Piotrowski C, Ihling CH, Sinz A (2015) Extending the cross-linking/mass spectrometry strategy. Facile incorporation of photo-activatable amino acids into the model protein calmodulin in Escherichia coli cells. Methods 89: 121–127. doi: 10.1016/j.ymeth.2015.02.012

98. Pollard AK, Craig EL, Chakrabarti L (2016) Mitochondrial Complex 1 Activity Measured by Spectrophotometry Is Reduced across All Brain Regions in Ageing and More Specifically in Neurodegeneration. PLoS ONE 11(6): e0157405. doi: 10.1371/journal.pone.0157405

99. Pollard TD (2016) Actin and Actin-Binding Proteins. Cold Spring Harb Perspect Biol 8(8). doi: 10.1101/cshperspect.a018226

100. Porter GA, Beutner G (2018) Cyclophilin D, Somehow a Master Regulator of Mitochondrial Function. Biomolecules 8(4). doi: 10.3390/biom8040176

101. Ptáčková R, Ječmen T, Novák P et al. (2014) The application of an emerging technique for protein-protein interaction interface mapping: the combination of photo-initiated cross-linking protein nanoprobes with mass spectrometry. Int J Mol Sci 15(6): 9224–9241. doi: 10.3390/ijms15069224

102. Pu W, Zheng Y, Peng Y (2020) Prolyl Isomerase Pin1 in Human Cancer: Function, Mechanism, and Significance. Front Cell Dev Biol 8: 168. doi: 10.3389/fcell.2020.00168

103. Rahfeld JU, Rücknagel KP, Schelbert B et al. (1994) Confirmation of the existence of a third family among peptidyl-prolyl cis/trans isomerases. Amino acid sequence and recombinant production of parvulin. FEBS Letters 352(2): 180–184

104. Rahfeld J-U, Schierhorn A, Mann K et al. (1994) A novel peptidyl-prolyl cisltrans isomerase from Escherichia coli. FEBS Letters 343(1): 65–69. doi: 10.1016/0014-5793(94)80608-X

105. Ran FA, Hsu PD, Wright J et al. (2013) Genome engineering using the CRISPR-Cas9 system. nprot 8(11): 2281–2308. doi: 10.1038/nprot.2013.143

106. Ranganathan R, Lu KP, Hunter T et al. (1997) Structural and Functional Analysis of the Mitotic Rotamase Pin1 Suggests Substrate Recognition Is Phosphorylation Dependent. Cell 89(6): 875–886. doi: 10.1016/S0092-8674(00)80273-1

107. Rao JN, Dominguez R (2014) Complex of ADP-actin With the N-terminal Actin-Binding Domain of Tropomodulin

108. Rappsilber J, Mann M, Ishihama Y (2007) Protocol for micro-purification, enrichment, pre-fractionation and storage of peptides for proteomics using StageTips. Nat Protoc 2(8): 1896–1906. doi: 10.1038/nprot.2007.261

109. Redwine WB, DeSantis ME, Hollyer I et al. (2017) The human cytoplasmic dynein interactome reveals novel activators of motility. Elife 6. doi: 10.7554/eLife.28257

110. Rehic E, Hoenig D, Kamba BE et al. (2019) Structural Analysis of the 42 kDa Parvulin of Trypanosoma brucei. Biomolecules 9(3): 93. doi: 10.3390/biom9030093

111. Reimer T (2003) Cellular localization and function of peptidyl-prolyl cis-trans isomerase hPar14, Universität Duisburg-Essen

112. Reimer T, Weiwad M, Schierhorn A et al. (2003) Phosphorylation of the N-terminal Domain Regulates Subcellular Localization and DNA Binding Properties of the Peptidyl-prolyl cis/trans Isomerase hPar14. Journal of Molecular Biology 330(5): 955–966. doi: 10.1016/S0022-2836(03)00713-7

113. Ridley AJ, Schwartz MA, Burridge K et al. (2003) Cell migration: integrating signals from front to back. Science 302(5651): 1704–1709. doi: 10.1126/science.1092053

114. Rippmann JF, Hobbie S, Daiber C et al. (2000) Phosphorylation-dependent proline isomerization catalyzed by Pin1 is essential for tumor cell survival and entry into mitosis. Cell Growth Differ 11(7): 409–416

115. Rohde N (2009) NMR-spektroskopische Studien der PPiase-Domäne von hPar 14/17 mit Liganden, Universität Duisburg-Essen

116. Rolland T, Taşan M, Charloteaux B et al. (2014) A proteome-scale map of the human interactome network. Cell 159(5): 1212–1226. doi: 10.1016/j.cell.2014.10.050

117. Rulten S, Thorpe J, Kay J (1999) Identification of eukaryotic parvulin homologues. A new subfamily of peptidylprolyl cis-trans isomerases. Biochem Biophys Res Commun 259(3): 557–562. doi: 10.1006/bbrc.1999.0828

118. Saeed U, Kim J, Piracha ZZ et al. (2018) Parvulin 14 and parvulin 17 bind to HBx and cccDNA and upregulate HBV replication from cccDNA to virion in a HBx-dependent manner. J Virol. doi: 10.1128/JVI.01840-18

119. Salabei JK, Gibb AA, Hill BG (2014) Comprehensive measurement of respiratory activity in permeabilized cells using extracellular flux analysis. nprot 9(2): 421–438. doi: 10.1038/nprot.2014.018

120. Saningong AD, Bayer P (2015) Human DNA-binding peptidyl-prolyl cis/trans isomerase Par14 is cell cycle dependently expressed and associates with chromatin in vivo. BMC Biochem 16: 4. doi: 10.1186/S12858_015_0033_x

121. Sarkar P, Reichman C, Saleh T et al. (2007) Proline cis-trans isomerization controls autoinhibition of a signaling protein. Mol Cell 25(3): 413–426. doi: 10.1016/j.molcel.2007.01.004

122. Scherer G, Kramer ML, Schutkowski M et al. (1998) Barriers to Rotation of Secondary Amide Peptide Bonds. J Am Chem Soc 120(22): 5568–5574. doi: 10.1021/ja980181t

123. Schiene-Fischer C (2015) Multidomain Peptidyl Prolyl cis/trans Isomerases. Biochim Biophys Acta 1850(10): 2005–2016. doi: 10.1016/j.bbagen.2014.11.012

124. Schiene-Fischer C, Aumüller T, Fischer G (2013) Peptide bond cis/trans isomerases: a biocatalysis perspective of conformational dynamics in proteins. Top Curr Chem 328: 35–67. doi: 10.1007/128_2011_151

125. Schmid FX, Baldwin RL (1978) Acid catalysis of the formation of the slow-folding species of RNase A: evidence that the reaction is proline isomerization. Proc Natl Acad Sci U S A 75(10): 4764–4768. doi: 10.1073/pnas.75.10.4764

126. Scholz C, Rahfeld J, Fischer G et al. (1997) Catalysis of protein folding by parvulin. Journal of Molecular Biology 273(3): 752–762. doi: 10.1006/jmbi.1997.1301

127. Schönbrunner ER, Mayer S, Tropschug M et al. (1991) Catalysis of protein folding by cyclophilins from different species. J. Biol. Chem. 266(6): 3630–3635. doi: 10.1016/S0021-9258(19)67841-5

128. Sekerina E, Rahfeld JU, Müller J et al. (2000) NMR solution structure of hPar14 reveals similarity to the peptidyl prolyl cis/trans isomerase domain of the mitotic regulator hPin1 but indicates a different functionality of the protein. Journal of Molecular Biology 301(4): 1003–1017. doi: 10.1006/jmbi.2000.4013

129. Seo S, Baye LM, Schulz NP et al. (2010) BBS6, BBS10, and BBS12 form a complex with CCT/TRiC family chaperonins and mediate BBSome assembly. Proc Natl Acad Sci U S A 107(4): 1488–1493. doi: 10.1073/pnas.0910268107

130. Shen Z-J, Esnault S, Malter JS (2005) The peptidyl-prolyl isomerase Pin1 regulates the stability of granulocyte-macrophage colony-stimulating factor mRNA in activated eosinophils. Nat Immunol 6(12): 1280–1287. doi: 10.1038/ni1266

131. Siegel V, Walter P (1985) Elongation arrest is not a prerequisite for secretory protein translocation across the microsomal membrane. J Cell Biol 100(6): 1913–1921. doi: 10.1083/jcb.100.6.1913

132. Smith FD, Samelson BK, Scott JD (2011) Discovery of cellular substrates for protein kinase A using a peptide array screening protocol. Biochem J 438(1): 103–110. doi: 10.1042/BJ20110720

133. Stark C, Breitkreutz B-J, Reguly T et al. (2006) BioGRID: a general repository for interaction datasets. Nucleic Acids Res 34(Database issue): D535-9. doi: 10.1093/nar/gkj109

134. Stelzl U, Worm U, Lalowski M et al. (2005) A human protein-protein interaction network: a resource for annotating the proteome. Cell 122(6): 957–968. doi: 10.1016/j.cell.2005.08.029

135. Stewart DE, Sarkar A, Wampler JE (1990) Occurrence and role ofcis peptide bonds in protein structures. Journal of Molecular Biology 214(1): 253–260. doi: 10.1016/0022-2836(90)90159-J

136. Suchanek M, Radzikowska A, Thiele C (2005) Photo-leucine and photo-methionine allow identification of protein-protein interactions in living cells. Nat Methods 2(4): 261–267. doi: 10.1038/nmeth752

137. Surmacz TA, Bayer E, Rahfeld JU et al. (2002) The N-terminal basic domain of human parvulin hPar14 is responsible for the entry to the nucleus and high-affinity DNA-binding. Journal of Molecular Biology 321(2): 235–247

138. Szklarczyk D, Gable AL, Lyon D et al. (2019) STRING v11: protein-protein association networks with increased coverage, supporting functional discovery in genome-wide experimental datasets. Nucleic Acids Res 47(D1): D607-D613. doi: 10.1093/nar/gky1131

139. Terada T, Shirouzu M, Fukumori Y et al. (2001) Solution structure of the human parvulin-like peptidyl prolyl cis/trans isomerase, hPar14. Journal of Molecular Biology 305(4): 917–926. doi: 10.1006/jmbi.2000.4293

140. (2021) The Gene Ontology resource: enriching a GOld mine. Nucleic Acids Res 49(D1): D325-D334. doi: 10.1093/nar/gkaa1113

141. The UniProt Consortium (2021) UniProt: the universal protein knowledgebase in 2021. Nucleic Acids Res 49(D1): D480-D489. doi: 10.1093/nar/gkaa1100

142. Thiele A, Krentzlin K, Erdmann F et al. (2011) Parvulin 17 promotes microtubule assembly by its peptidyl-prolyl cis/trans isomerase activity. Journal of Molecular Biology 411(4): 896–909. doi: 10.1016/j.jmb.2011.06.040

143. Tuorto F, Liebers R, Musch T et al. (2012) RNA cytosine methylation by Dnmt2 and NSun2 promotes tRNA stability and protein synthesis. Nat Struct Mol Biol 19(9): 900–905. doi: 10.1038/nsmb.2357

144. Tyanova S, Temu T, Sinitcyn P et al. (2016) The Perseus computational platform for comprehensive analysis of (prote)omics data. Nat Methods 13(9): 731–740. doi: 10.1038/nmeth.3901

145. Uchida T, Fujimori F, Tradler T et al. (1999) Identification and characterization of a 14 kDa human protein as a novel parvulin-like peptidyl prolyl cis/trans isomerase. FEBS Letters 446(2-3): 278–282. doi: 10.1016/S0014-5793(99)00239-2

146. Uchida T, Takamiya M, Takahashi M et al. (2003) Pin1 and Par14 Peptidyl Prolyl Isomerase Inhibitors Block Cell Proliferation. Chemistry & Biology 10(1): 15–24. doi: 10.1016/S1074-5521(02)00310-1

147. Uhlen M, Zhang C, Lee S et al. (2017) A pathology atlas of the human cancer transcriptome. Science 357(6352). doi: 10.1126/science.aan2507

148. Uhlén M, Fagerberg L, Hallström BM et al. (2015) Proteomics. Tissue-based map of the human proteome. Science 347(6220): 1260419. doi: 10.1126/science.1260419

149. Ünal CM, Berges M, Smit N et al. (2018) PrsA2 (CD630_35000) of Clostridioides difficile Is an Active Parvulin-Type PPIase and a Virulence Modulator. Front Microbiol 9: 2913. doi: 10.3389/fmicb.2018.02913

150. Uren PJ, Bahrami-Samani E, Araujo PR de et al. (2016) High-throughput analyses of hnRNP H1 dissects its multi-functional aspect. RNA Biol 13(4): 400–411. doi: 10.1080/15476286.2015.1138030

151. van Zundert GCP, Rodrigues JPGLM, Trellet M et al. (2016) The HADDOCK2.2 Web Server: User-Friendly Integrative Modeling of Biomolecular Complexes. Journal of Molecular Biology 428(4): 720–725. doi: 10.1016/j.jmb.2015.09.014

152. Vranken WF, Boucher W, Stevens TJ et al. (2005) The CCPN data model for NMR spectroscopy: development of a software pipeline. Proteins 59(4): 687–696. doi: 10.1002/prot.20449

153. Wan C, Borgeson B, Phanse S et al. (2015) Panorama of ancient metazoan macromolecular complexes. Nature 525(7569): 339–344. doi: 10.1038/nature14877

154. Wang F, Orlova A, Avery AW et al. (2017) Cryo-EM structure of F-actin complexed with the beta-III-spectrin actin-binding domain

155. Wang K, Li Y, Wang J et al. (2021) A novel 12-gene signature as independent prognostic model in stage IA and IB lung squamous cell carcinoma patients. Clin Transl Oncol. doi: 10.1007/s12094-021-02638-1

156. Wang L, Zhou Y, Chen D et al. (2020) Peptidyl-Prolyl Cis/Trans Isomerase Pin1 and Alzheimer's Disease. Front Cell Dev Biol 8: 355. doi: 10.3389/fcell.2020.00355

157. Wang X, Mahoney BJ, Zhang M et al. (2015) Negative Regulation of Peptidyl-Prolyl Isomerase Activity by Interdomain Contact in Human Pin1. Structure 23(12): 2224–2233. doi: 10.1016/j.str.2015.08.019

158. Wu C, Ma MH, Brown KR et al. (2007) Systematic identification of SH3 domain-mediated human protein-protein interactions by peptide array target screening. Proteomics 7(11): 1775–1785. doi: 10.1002/pmic.200601006

159. Wulf G, Finn G, Suizu F et al. (2005) Phosphorylation-specific prolyl isomerization: is there an underlying theme? Nat Cell Biol 7(5): 435–441. doi: 10.1038/ncb0505-435

160. Wulf GM, Ryo A, Wulf GG et al. (2001) Pin1 is overexpressed in breast cancer and cooperates with Ras signaling in increasing the transcriptional activity of c-Jun towards cyclin D1. EMBO J 20(13): 3459–3472. doi: 10.1093/emboj/20.13.3459

161. Yang J, Zhang Y (2015) I-TASSER server: new development for protein structure and function predictions. Nucleic Acids Res 43(W1): W174-81. doi: 10.1093/nar/gkv342

162. Yao X, Wigginton JG, Maass DL et al. (2014) Estrogen-provided cardiac protection following burn trauma is mediated through a reduction in mitochondria-derived DAMPs. Am J Physiol Heart Circ Physiol 306(6): H882-94. doi: 10.1152/ajpheart.00475.2013

163. Zhang J, Nakatsu Y, Shinjo T et al. (2013) Par14 protein associates with insulin receptor substrate 1 (IRS-1), thereby enhancing insulin-induced IRS-1 phosphorylation and metabolic actions. J Biol Chem 288(28): 20692–20701. doi: 10.1074/jbc.M113.485730

164. Zhang M, Frederick TE, VanPelt J et al. (2020) Coupled intra- and interdomain dynamics support domain cross-talk in Pin1. J Biol Chem. doi: 10.1074/jbc.RA120.015849

165. Zhang M, Wang XJ, Chen X et al. (2012) Structural and kinetic analysis of prolyl-isomerization/phosphorylation cross-talk in the CTD code. ACS Chem Biol 7(8): 1462–1470. doi: 10.1021/cb3000887

166. Zhou XZ, Lu PJ, Wulf G et al. (1999) Phosphorylation-dependent prolyl isomerization: a novel signaling regulatory mechanism. Cell Mol Life Sci 56(9-10): 788–806. doi: 10.1007/s000180050026

167. Zoldák G, Aumüller T, Lücke C et al. (2009) A library of fluorescent peptides for exploring the substrate specificities of prolyl isomerases. Biochemistry 48(43): 10423–10436. doi: 10.1021/bi9014242

Figure 17 and Figure 19 are republished with permission of Walter de Gruyter and Company, from “Targeting of parvulin interactors by diazirine mediated cross-linking discloses a cellular role of human Par14/17 in actin polymerization.”, Goehring, Anna; Michin, Irina; Gerdes, Tina; Schulze, Nina; Blueggel, Mike; Rehic, Edisa; Kaschani, Farnusch; Kaiser, Markus; Bayer, Peter, Volume 401, Issue 8, 2020, permission conveyed through Copyright Clearance Center, Inc.

7 Danksagung

Ich danke Herrn Prof. Dr. Peter Bayer für die Möglichkeit eine Dissertation in seiner Arbeitsgruppe anzufertigen, die freundliche Aufnahme in diese Arbeitsgruppe, die hervorragende Betreuung sowie die ständige Bereitschaft zur Diskussion. Ebenso danke ich auch dafür, dass Prof. Dr. Peter Bayer mir immer mit Rat, Tat und seinem Wissen zur Seite gestanden und mich in meinen Ideen sowie meiner Kreativität gefördert hat.

Herrn Prof. Dr. Raphael Stoll danke ich für die unkomplizierte, kompetente und freundliche Übernahme des Zweitgutachtens.

Ich möchte mich auch bei allen meinen Kooperationspartnern während der Doktorarbeit bedanken. Im Speziellen Frau PD Dr. Ulrike Hendgen-Cotta für die tolle Zusammenarbeit und die Möglichkeit in ihrem Labor Messungen durchzuführen und ihrer Arbeitsgruppe für die herzliche Aufnahme. Prof. Dr. Markus Kaiser für die Möglichkeit der Analyse meiner Proben in der Analytics Core Facility Essen (ACE) mit der Hilfe von Dr. Farnusch Kaschani und Svenja Heimann. Sowie Prof. Dr. Michael Ehrmann für die Möglichkeit der Nutzung des Peptide Synthesizer und Helmut Tourné für die Herstellung des Peptid Spotter Array.

Ein ganz besonderer Dank gilt auch meiner Arbeitsgruppe. Danke für die unvergessliche Zeit und, dass ihr mir immer mit Rat und Tat zur Seite standet! Meine lieben Promotionsbuddys Daniel und Mike (oder lieber Professor Blüggel) danke für viele gemeinsame Stunden im Labor und Promotionsoffice sowie die schönen und lustigen Momente an die ich mich immer erinnern werden (Schrödingers Katze in der Knaueranlage, 2020 für nichts und wieder nichts etc.). Liebe Tina ich danke dir, dass du mir in der Zellkultur Beistand geleistet hast, für mich eingesprungen bist, wenn ich nicht da war und für die vielen gemeinsamen Pläuschen. Liebe Anja und liebe Christine, danke, dass ihr euch immer Zeit für mich genommen und mich unterstützt habt (vor allem am NMR) ohne euch wäre ich nicht so glücklich mit meinen Daten. Liebe Edisa, Bianca und Dana es ist schön, dass wir so viele tolle Momente gemeinsam konnten und uns immer sehr gut über die Forschung austauschen konnten. Liebe Elke, danke für deine außerordentliche Hilfsbereitschaft. Du hast es immer geschafft, dass wir alles bekommen haben, was wir brauchten und zusätzlich

hast du mich noch so gut versorgt mit glutenfreien Süßigkeiten. Liebe Alma, danke, dass du immer fleißig Proteine gereinigt und mich unterstützt hast wo immer es ging. Lieber Peter danke, dass du immer alles im Schuss gehalten und durch deine tollen Fotos all die schönen Momente festgehalten hast. Ausdrücklich bedanken möchte ich mich auch noch bei Mina, Helmut, Jenni, Maike und Joel für ihre Hilfe und die schönen gemeinsam erlebten Momente.

Insbesondere danke ich auch all meinen Freunden, dafür, dass ihr euch mit viel Spaß und guter Laune um meine Work-Live-Balance gekümmert habt. Darüber hinaus noch einen Dank an die Crazy G's die zusätzlich auch manchmal noch einen fachlichen Rat parat hatten. Meiner Familie danke ich für die Motivation und den Zuspruch während meines Studiums und der Promotion. Besonders möchte ich mich bei meiner Mutter und meiner Oma bedanken, da sie mir so das Studium erst ermöglicht haben. Bei meinem Vater und meinem Bruder möchte ich mich für ihr andauerndes Interesse bedanken und bei meiner Tante für ihre liebevollen Motivationspakete. Und am Schluss möchte ich mich bei Philipp bedanken, dafür, dass er immer ein offenes Ohr für mich hatte, mir den Rücken freigehalten und mich auf dem Boden der Tatsachen gehalten hat.

8 Lebenslauf

"Der Lebenslauf ist in der Online-Version aus Gründen des Datenschutzes nicht enthalten."

9 Eidesstattliche Erklärungen

Erklärung:

Hiermit erkläre ich, gem. § 7Abs. (2) d) + f) der Promotionsordnung der Fakultät für Biologie zur Erlangung des Dr. rer. nat., dass ich die vorliegende Dissertation selbständig verfasst und mich keiner anderen als der angegebenen Hilfsmittel bedient,bei der Abfassung der Dissertation nur die angegeben Hilfsmittel benutzt und alle wörtlich oder inhaltlich übernommenen Stellen als solche gekennzeichnet habe.

Essen, den ________________ __________________________________

Unterschrift des/r Doktoranden/in

Erklärung:

Hiermit erkläre ich, gem. § 7Abs. (2) e) + g) der Promotionsordnung der Fakultät für Biologie zur Erlangung des Dr. rer. nat., dass ich keine anderen Promotionen bzw. Promotionsversuche in der Vergangenheit durchgeführt habe und dass diese Arbeit von keiner anderen Fakultät/Fachbereich abgelehnt worden ist.

Essen, den ________________ __________________________________

Unterschrift des/r Doktoranden/in

Erklärung:

Hiermit erkläre ich, gem. § 6 Abs. (2) g) der Promotionsordnung der Fakultät für Biologie zur Erlangung der Dr. rer. nat., dass ich das Arbeitsgebiet, dem das Thema „The role of Par17’s N-terminus in interaction and function of the enzyme“ zuzuordnen ist, in Forschung und Lehre vertrete und den Antrag von Anna Göhring befürworte und die Betreuung auch im Falle eines Weggangs, wenn nicht wichtige Gründe dem entgegenstehen, weiterführen werde.

____

Name des Mitglieds der Universität Duisburg-Essen in Druckbuchstaben

Essen, den ________________ ______________________________________

Unterschrift eines Mitglieds der Universität Duisburg-Essen